

# Magnetic Properties of the One-Band Hubbard Model

## **Dissertation**

zur Erlangung des Doktorgrades  
der Naturwissenschaften (Dr. rer. nat.)  
der Mathematisch-Naturwissenschaftlichen Fakultät  
der Universität Augsburg

vorgelegt von  
**Robert Zitzler**  
aus Teublitz

2004

Promotionsgesuch eingereicht am 24.05.2004.

Prüfungskommission:	Vorsitzender:	PD Dr. Alexander Krimmel
	Erstgutachter:	Prof. Dr. Thomas Pruschke
	Zweitgutachter:	Prof. Dr. Thilo Kopp
	Weitere Prüfer:	Prof. Dr. Ulrich Eckern
		Prof. Dr. Bernd Stritzker

Termin der mündlichen Prüfung: 19.07.2004

# CONTENTS

<b>1. Introduction</b>	1
<b>2. Models for the description of strongly correlated electron systems</b>	5
2.1 The one-band Hubbard model	5
2.2 The single impurity Anderson model	11
<b>3. The Dynamical Mean-Field Theory</b>	15
3.1 The local approximation	15
3.2 Mapping onto an effective impurity problem	17
3.3 DMFT on a bipartite lattice	20
<b>4. Solution of the effective impurity problem</b>	25
4.1 The Numerical Renormalization Group	25
4.2 Generalization for problems with broken symmetry	26
4.3 Calculation of dynamical quantities	38
<b>5. Results</b>	47
5.1 The Hubbard model at half filling	47
5.1.1 The paramagnetic metal-insulator transition	47
5.1.2 The antiferromagnetic state	50
5.1.3 The Hubbard model with frustration	59
5.2 Results for finite doping	70
5.2.1 Phase Separation	70
5.2.2 Ferromagnetism	79

<b>6. Summary and Outlook . . . . .</b>	<b>85</b>
<b>Appendix</b>	<b>89</b>
<b>A. Details of the NRG formalism . . . . .</b>	<b>91</b>
<b>B. Evaluation of the integrals in Sec. 3.3 . . . . .</b>	<b>95</b>
<b>Bibliography . . . . .</b>	<b>99</b>
<b>Acknowledgements . . . . .</b>	<b>105</b>

## 1. INTRODUCTION

The microscopic description of magnetism to this day constitutes one of the major areas of research in modern solid state theory. Motivated by a wide variety of interesting phenomena, the development of new methods for an accurate description of these materials is one of the most exciting fields of physics. This is true in particular for materials where the interactions between the electrons play an important role in determining the physical properties of the system. For the investigation of these strongly correlated materials, single-particle methods such as the Density Functional Theory (DFT) are not sufficient. In general, the electrons in these systems occupy narrow atomic orbitals and, as a result, experience a strong Coulombic repulsion. This interaction requires the use of many-body methods in order to arrive at a correct description of these materials. However, in most cases the complexity of the resulting many-particle problem prohibits the consideration of the full electronic structure, and simplified effective models have to be introduced in order to capture the underlying physics. These models only take into account the most important degrees of freedom, such as one or several orbitals near the Fermi level, and the behavior of the system is studied by varying the parameters of the corresponding model.

The reduction of the full many-body Hamiltonian to a simple effective model is in itself a complicated problem, and in general the resulting models can not be solved exactly. A variety of approximative and numerically exact methods have been developed, but there are a number of shortcomings to each of these approaches. Most of the approximative methods are based on a perturbatory expansion and therefore only valid in a certain parameter regime, while numerically exact methods such as Quantum Monte Carlo (QMC) calculations or Exact Diagonalization (ED) are restricted to finite and rather small system sizes, making it difficult to evaluate the quantities of interest in the thermodynamic limit. In recent years, considerable progress has been made in understanding models of correlated electrons by introducing a new limit to this problem, namely the limit of infinite lattice coordination. Within this Dynamical Mean-Field Theory (DMFT), each lattice site is assumed to have infinitely many neighbors, and the correlation effects are purely local. This results in a considerable reduction of the complexity of the problem. In particular, it allows for the mapping of the lattice onto an effective quantum impurity model. The solution of this model lies at the heart of a self-consistent scheme to calculate various quantities for the lattice

problem within the DMFT.

Clearly, in order to obtain reliable results for lattice models from the DMFT, an accurate method is needed to solve the impurity problem. In particular, this method should be non-perturbative, so that all the different parameter regimes are accessible, and furthermore, it should work in the thermodynamic limit. In addition, it should allow for the investigation of the ground state properties of the system, and therefore work at  $T = 0$ . In combining the above three aspects, Wilson's Numerical Renormalization Group (NRG) theory has become the method of choice for the solution of the impurity model at very low temperatures. One goal of this work is the extension of the NRG to allow for the investigation of symmetry-broken phases. In doing so, it will be possible to study the magnetic phases of the one-band Hubbard model within the DMFT, in particular the different types of magnetic order found in the ground state of this model.

In **Chapter 2**, the two generic models for the description of strongly correlated electron systems used in this work are introduced, the one-band Hubbard model and the single impurity Anderson model (SIAM). The relevance of the Hubbard model with respect to the description of real materials is discussed, and the different types of magnetic order it may show are reviewed briefly. Furthermore, an overview of the different parameter regimes of the SIAM is presented.

The method used to study the Hubbard model in this work, the dynamical mean-field theory, is reviewed in **Chapter 3**. In addition, the formalism of the DMFT on a bipartite lattice is presented. This is necessary in order to investigate the antiferromagnetic phase of the Hubbard model within the DMFT. A detailed account of the calculation of the optical conductivity in the antiferromagnetic phase concludes this chapter.

The concept of the numerical renormalization group theory is briefly introduced at the start of **Chapter 4**. A comprehensive description of the different steps that are necessary in the modification of the NRG to include the spin degree of freedom follows. In particular, the approach that has to be used to obtain accurate results for the dynamical quantities from the NRG is presented in detail.

The results from the DMFT calculations for the one-band Hubbard model with the NRG as the impurity solver are presented in **Chapter 5**. After a brief review of the established results for the paramagnetic metal-insulator transition (MIT) at half filling, the antiferromagnetic ground state of the model is discussed. In this context, a detailed analysis of the optical conductivity is carried out. In order to study the interplay of the metal-insulator transition and the magnetic ordering, results for the Hubbard model with frustration are presented. The remaining part of the chapter is used to discuss the types of magnetic order found for the Hubbard model away from half filling for different parameter regimes.

The thesis is concluded by a summary and an outlook in **Chapter 6**.

To enhance the readability, unless otherwise noted, the value of the constants  $\hbar$ ,  $g$ ,  $\mu_B$ ,  $k_B$  and the lattice constant  $a$  on a square lattice is set to 1.

Parts of this work are published in [Zit02, Pru03].



## 2. MODELS FOR THE DESCRIPTION OF STRONGLY CORRELATED ELECTRON SYSTEMS

In solid state physics there are many systems where a simple one-particle picture fails to describe the underlying physics. It turns out that the local Coulomb repulsion between the electrons is essential for a proper understanding of these materials. While methods like the density functional theory are highly successful in describing materials where the electrons are mostly delocalized, as is the case for metals with a conduction band made up of  $s$  or  $p$  electrons, they fail completely in describing systems where the electrons are much more localized. Prime examples for such materials are transition metals such as vanadium, iron, and their respective oxides, where the interaction between the electrons in the partially filled  $d$  or  $f$  shells is very strong and the conduction band is very narrow.

The simplest model for describing the interplay between localization and band formation in a solid is the one-band Hubbard model, which will be introduced in the first part of this chapter. However, despite its simplicity, the electronic interactions contained in this model still make it very hard to solve, and exact solutions can only be obtained in certain limiting cases. One of these limits, namely the one of infinite lattice coordination  $Z$ , has turned out to an excellent starting point for the investigation of the electronic properties of strongly correlated materials. In the framework of this so-called dynamical mean-field theory, a mapping onto an effective impurity problem is constructed, which then has to be solved in a self-consistent fashion. The resulting single impurity Anderson model is, however, far from trivial, and an introduction to this model and its various parameters makes up the second part of this chapter.

### 2.1 The one-band Hubbard model

As pointed out above, there are two important aspects which need to be incorporated into an effective model for the description of strongly correlated systems, namely the propagation of electrons in a conduction band of width  $W$  and the local Coulomb interaction  $U$  between the electrons. The simplest model that

takes this into account is the one-band Hubbard model [Hub63]

$$H = \sum_{\sigma} \sum_{ij} t_{ij} c_{i\sigma}^{\dagger} c_{j\sigma} + U \sum_i n_{i\uparrow} n_{i\downarrow}. \quad (2.1)$$

The first term describes the hopping of an electron from site  $i$  of a lattice to site  $j$ . The operators  $c_{i\sigma}^{\dagger}$  and  $c_{j\sigma}$  are standard fermionic creation and annihilation operators for an electron with spin  $\sigma$  at site  $i$  and  $j$  respectively. The nature of this hopping is determined by the matrix element  $t_{ij}$ . In most cases only hopping between nearest neighbors  $\langle i, j \rangle$  with a hopping amplitude  $-t$  is considered. The hopping amplitude is negative to reflect the gain in the kinetic energy of the system due to the hopping. The bandwidth  $W$  is connected to the size of the matrix element  $t$ , obviously a larger value of  $t$  results in a more itinerant behaviour of the electrons and an increase in the bandwidth. In this simple model there is no orbital degeneracy, i.e. only two electrons with opposite spin may occupy the same lattice site. If this is the case, one has to pay the correlation energy  $U$  because of the Coulomb repulsion between the two electrons. This is described by the second term in (2.1), where  $n_{i\sigma}$  is the number operator for an electron with spin  $\sigma$  at site  $i$ .

Even with such a simple model, it is possible to describe real materials at least qualitatively. Both transition metal oxides like NiO, CrO<sub>2</sub> or V<sub>2</sub>O<sub>3</sub> and the CuO<sub>2</sub>

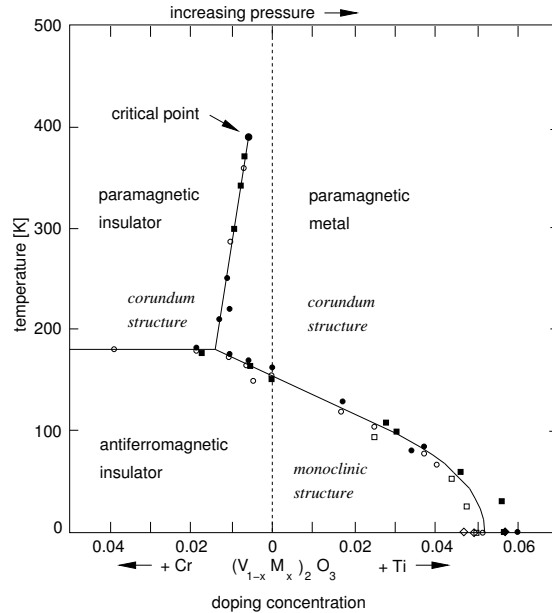


**Fig. 2.1:** Phase diagram of  $V_2O_3$  showing the MIT as a function of pressure and of doping with Cr and Ti [Kel04].

planes in the cuprates have been studied using the above model. A common property of these substances is the fact that their ground state is an antiferromagnetic

insulator. In addition, they may show a metal-insulator transition depending on composition, pressure or other control parameters [Ima98]. This kind of behavior is unexpected, as in most of these materials the conduction bands are partially filled, and they should therefore be metallic. In fact, this is what is found in band structure calculations based on the local density approximation.

Figure 2.1 shows the phase diagram of  $V_2O_3$  as a function of pressure and of doping with Cr and Ti atoms. Both the antiferromagnetic state at low temperatures and the paramagnetic metal-insulator transition can clearly be identified. The data points in the plot have been taken from the work of McWhan et al. [McW70]. All the transitions shown are of first order. The paramagnetic insulating phase is believed to be a so-called Mott-Hubbard insulator, and is a result of the strong electronic correlations. Therefore, for an accurate description of these materials, the local Coulomb interaction has to be taken into account. This requires the

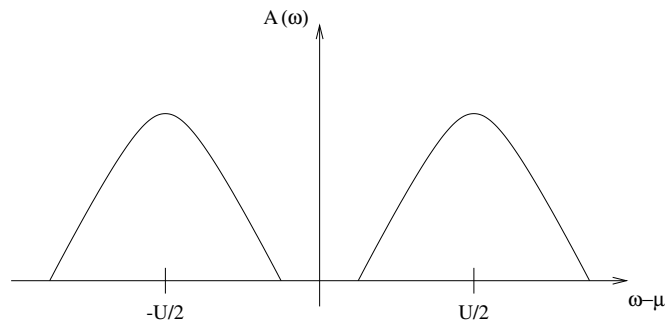


**Fig. 2.2:** *Qualitative shape of the spectral function for the half-filled Hubbard model for large values of the Coulomb interaction  $U$ .*

application of many-body methods, and in general the solution of the resulting model is a very complicated problem. In this work, the dynamical mean-field theory (see Chapter 3) is used to investigate the Hubbard model both at  $T = 0$  and at finite temperatures. It should be noted that there is one important difference between theory and experiment in the investigation of the metal-insulator transition. In the experiments, by doping with different-sized atoms or by applying pressure, it is the bandwidth  $W$  that is changed in order to drive the transition. In the calculations for the Hubbard model (2.1), in general, it is the value of the Coulomb interaction  $U$  that is varied in order to obtain either a metallic or an insulating solution, while the bandwidth is usually fixed. It is the ratio  $U/W$  that is important for the comparison between theory and experiment.

The fact that the Hubbard model does indeed have an insulating solution for large values of the Coulomb interaction  $U$  can easily be understood. At half filling, with one electron per site, it is clear that for very large  $U$  the double occupancy of a particular site is effectively prohibited. The excitation spectrum of the system

is split into two parts, and if  $U$  is large enough, a gap opens between the so-called lower and upper Hubbard bands. At half filling, the Fermi energy lies between these two bands, and the system becomes insulating. This is drawn schematically in Figure 2.2.

The tendency of the system to order antiferromagnetically can be understood from the following argument: If  $t/U \ll 1$ , the high energy excitations can be projected out of the Hilbert space by a canonical transformation (see e.g. [Ful95]). The effect of this transformation is to restrict the Hilbert space to states that are only singly occupied. As a result, the tJ-model is obtained,

$$H = -t \sum_{\sigma} \sum_{\langle ij \rangle} \tilde{c}_{i\sigma}^{\dagger} \tilde{c}_{j\sigma} + J \sum_{\langle ij \rangle} (\mathbf{S}_i \mathbf{S}_j - \frac{1}{4} \tilde{n}_i \tilde{n}_j), \quad (2.2)$$

where the operators  $\tilde{c}_{i\sigma} = (1 - n_{i\bar{\sigma}}) c_{i\sigma}$  and the corresponding creation operators act in the reduced Hilbert space. The second term contains corrections to the strict exclusion of the double occupancy of a site. It results in processes like the one shown in Figure 2.3. As the hopping to a neighboring site is possible only if

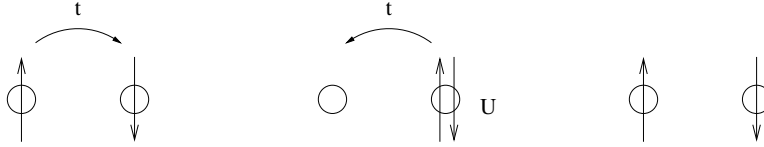


**Fig. 2.3:** Antiferromagnetic exchange process in the tJ-model.

the two spins are antiparallel, the antiferromagnetic nature of the correlation is obvious. The transformation results in an additional term that describes hopping processes involving three sites, but it is neglected here. A detailed discussion of the relevance of this term can be found in [Obe97a]. Perturbation theory up to second order results in an exchange coupling  $J = 4t^2/U$ .

At half filling, the first term in (2.2) cancels, and the second term becomes trivial. This results in the well-known Heisenberg model

$$H = J \sum_{\langle ij \rangle} \mathbf{S}_i \mathbf{S}_j \quad (2.3)$$

that is frequently used to describe antiferromagnetically ordered states. Therefore, at least at half filling and for large  $U$ , the Hubbard model is expected to show antiferromagnetic order. The antiferromagnetic state will be discussed in detail in Section 5.1. The situation is less clear away from half filling, and some other types of ordering may be relevant. This is discussed in the following.

## Ferromagnetism and phase separation

In the previous section it has been shown that the one-band Hubbard model can be viewed as a generic model for the description of an antiferromagnetic insulator. This is interesting, as it had originally been proposed in order to explain the ferromagnetism found in transition metals such as Fe or Ni [Hub63]. There, it is the delocalized  $d$  electrons that carry the moments that result in the magnetic behavior of the system. However, the simple model (2.1) does not contain the complicated structure of the atomic orbitals of these elements, nor can it describe the local exchange and Coulomb interactions both within one orbital and between electrons occupying different orbitals. Still, under certain conditions, this simple model can also have a ferromagnetic solution.

The most important statement in this regard is the Nagaoka theorem [Nag66]. It states that in the limit  $U \rightarrow \infty$  and in the presence of exactly one hole in the half-filled system, the ground state is a fully polarized ferromagnet. This statement is true for different lattice types, among others also for a hypercubic lattice. This has led to the question whether the ferromagnetic solution extends to higher doping, finite  $U$  and finite temperature. For a review of the work along these lines see e.g. [Obe97a]. Both in the Hubbard model and the tJ-model an extended ferromagnetic phase has been found above a critical value  $U_c$  within the DMFT [Jar93, Obe97b] at finite temperatures. It can be seen from these results that the tJ-model does indeed describe the low-energy physics of the Hubbard model very well, however, for smaller values of  $U$  there are some discrepancies. In the above calculations nothing could be said about the ground state of the system, as the method used for the solution of the impurity model, the non-crossing approximation (NCA), a resolvent perturbation theory in the hybridization (see e.g. [Hew93]), fails at  $T = 0$ . This has been part of the motivation to extend the NRG method described in Chapter 4 to allow for the investigation of symmetry-broken phases. In doing so, a very powerful method is available to study the magnetic properties of the Hubbard model both at  $T = 0$  and at finite temperature within the DMFT. In addition, due to the non-perturbative nature of the NRG, there are no restrictions in the choice of the parameters of the model, such as the strength of the Coulomb interaction  $U$  or the filling  $n$ .

The introduction of the limit  $d \rightarrow \infty$  in the DMFT in principle allows for the exact solution of this model. This has resulted in a large amount of investigations of the infinite dimensional Hubbard model. In addition,  $d \rightarrow \infty$  has turned out to be a reasonable starting point for weak-coupling expansions [Don91, Don94, Don96]. Within this approach, in addition to the expected antiferromagnetic order on a bipartite lattice, phase separation was found for the whole region of the magnetically ordered phase [Don96]. This phenomenon describes the spatially inhomogeneous distribution of the electrons on the lattice. In this scenario it is energetically

favorable for the electrons to form regions with higher and lower density for a fixed filling  $n$ . Since this result is based on a weak-coupling expansion, it is far from clear whether it holds true for finite values of the interaction  $U$  as well. Results from a numerically exact solution of the Hubbard model in  $d = \infty$  based on Quantum Monte Carlo simulations for example showed no evidence of phase separation [Fre95], but these calculations were done in the paramagnetic phase and at finite, comparatively high temperatures.

The question whether phase separation in the Hubbard model occurs in a certain parameter regime is of importance for two reasons. First, from a model theoretical point of view, it is of course interesting to explore the stability of the different possible ordered phases with respect to phase separation. Second, a vicinity to phase separation has been discussed as one of the possible ingredients to the superconductivity in the high- $T_c$  cuprates [Eme93, Cas95]. Moreover, a tendency towards phase separation together with the long-range part of the Coulomb interaction may in principle lead to charge ordered states such as stripe-phases.

Phase separation has long been predicted [Eme90, Eme93] and indeed been observed for the tJ-model in  $d = 1, 2$  (for a review see e.g. [Dag94]). Since the tJ-model for vanishing  $J$  is connected to the Hubbard model in the limit  $U/t \rightarrow \infty$  (see the discussion in the previous section), additional information about phase separation in the strong coupling limit could thus be obtained. However, the early work on phase separation in the tJ-model established phase separation only for  $J \sim t$  [Dag94]. Despite ongoing efforts [Hel97, Pry98] the situation in the limit  $J \rightarrow 0$  is far from clear, and more detailed studies are necessary. The question about whether there is phase separation in the Hubbard model in  $d = 2$  has not been clarified yet even for  $U/t \rightarrow \infty$ , since a direct inspection of the Hubbard model in this limit has led to contradictory results [Su96, Tan99].

The results for the  $2d$  Hubbard model for finite  $U$  available so far have not revealed signs for phase separation [Dag94, Bec00]. However, these results are typically based on Quantum Monte Carlo or related techniques, which have severe problems in the interesting parameter regime close to half filling and at very low temperatures. Consequently, one either has to restrict oneself to rather small system sizes [Dag94] or use other approximations [Bec00]. Thus, a detailed study of the ground state phase diagram of the Hubbard model in the thermodynamic limit and in the vicinity of half filling, comprising weak, intermediate and strong coupling within a non-perturbative approach, has not been available so far. In this work, DMFT calculations for the ground state of the model away from half filling are presented in Section 5.2. It is clear that in this approach non-local dynamics can not be taken into account. While this is obviously a considerable simplification, especially for dimensions  $d \leq 2$ , the results can still provide insight into whether phase separation is possible at all.

As the central aspect of the DMFT is the mapping of the lattice model onto an

effective impurity problem, in the following section the single impurity Anderson model will be introduced and its different parameter regimes will be discussed briefly.

## 2.2 The single impurity Anderson model

In the framework of the dynamical mean-field theory, the lattice problem is mapped onto an effective single impurity Anderson model [And61]. The Hamiltonian of the SIAM has the following form:

$$\begin{aligned}
 H = & \sum_{\sigma} \epsilon_{f\sigma} f_{\sigma}^{\dagger} f_{\sigma} + U f_{\uparrow}^{\dagger} f_{\uparrow} f_{\downarrow}^{\dagger} f_{\downarrow} \\
 & + \sum_{\mathbf{k}\sigma} \epsilon_{\mathbf{k}\sigma} c_{\mathbf{k}\sigma}^{\dagger} c_{\mathbf{k}\sigma} + \sum_{\mathbf{k}\sigma} V_{\mathbf{k}\sigma} (f_{\sigma}^{\dagger} c_{\mathbf{k}\sigma} + c_{\mathbf{k}\sigma}^{\dagger} f_{\sigma}).
 \end{aligned} \tag{2.4}$$

The first two terms describe the magnetic impurity itself. The operators  $f_{\sigma}^{\dagger}$  and  $f_{\sigma}$  create or annihilate an electron with spin  $\sigma$  at the impurity site. Its energy is given by  $\epsilon_{f\sigma}$ . Only one orbital is considered, i.e. the impurity level can accommodate a maximum of two electrons at the same time. While this degeneracy is in general higher in real systems, it is enough to consider this simple case in order to capture the essence of the underlying physics. Extensions of the model (2.4) are discussed e.g. in the book by Hewson [Hew93]. The second term of the Hamiltonian contains the Coulomb energy  $U$  that has to be paid for putting a second electron onto the already occupied impurity level. Once there is an electron with energy  $\epsilon_{f\sigma}$  at the impurity, it is necessary to spend the energy  $\epsilon_{f\bar{\sigma}} + U$  in order to add one more. In a certain parameter regime, this results in the presence of a localized magnetic moment that lies at the heart of the Kondo effect. This will be discussed in more detail later.

The third term in (2.4) describes a band of uncorrelated conduction electrons with dispersion  $\epsilon_{\mathbf{k}\sigma}$ . The operators  $c_{\mathbf{k}\sigma}^{\dagger}$  and  $c_{\mathbf{k}\sigma}$  create or annihilate an electron in the conduction band with wave vector  $\mathbf{k}$  and spin  $\sigma$ . The form of the dispersion is of no importance, as in the following discussion only the density of states

$$\rho_{\sigma}(\epsilon) = \frac{1}{N} \sum_{\mathbf{k}} \delta(\epsilon - \epsilon_{\mathbf{k}\sigma}) \tag{2.5}$$

will be considered. The energies  $\epsilon$  are assumed to lie in the interval  $[-D, D]$ , i.e. the bandwidth is  $2D$ .

The last term in (2.4) describes the hybridization of the impurity with the conduction band via the matrix elements  $V_{\mathbf{k}\sigma}$ . In the case of  $V_{\mathbf{k}\sigma} = 0$  the impurity and the conduction electrons are decoupled, and the two separate problems are

easily solved. If that is not the case, then the local correlations at the impurity site result in a complicated many-body problem that has been the object of intense theoretical efforts for many decades [Hew93].

The correlations due to the Coulomb interaction  $U$  at the site of the impurity lead to a self-energy term  $\Sigma_\sigma(z)$  in the impurity Green's function

$$G_\sigma^f(z) = \frac{1}{z - \epsilon_{f\sigma} - \Sigma_\sigma(z) - \Delta_\sigma(z)}. \quad (2.6)$$

The hybridization function

$$\Delta_\sigma(z) = \sum_{\mathbf{k}\sigma} V_{\mathbf{k}\sigma}^2 \frac{1}{z - \epsilon_{\mathbf{k}\sigma}} \quad (2.7)$$

describes the transition of an electron from the impurity level into the conduction band, the propagation with  $1/(z - \epsilon_{\mathbf{k}\sigma})$  in the band and a subsequent return to the impurity site.

### Parameter regimes of the SIAM

The physics of the model introduced in the previous section are determined by the interplay of the parameters  $V_{\mathbf{k}\sigma}$ ,  $U$  and  $\epsilon_{f\sigma}$ . As already mentioned, the case  $V_{\mathbf{k}\sigma} = 0$  is trivial. In the spectral function for the impurity there are just two  $\delta$ -peaks at energies  $\epsilon_{f\sigma}$  and  $\epsilon_{f\bar{\sigma}} + U$ . If  $V_{\mathbf{k}\sigma}$  is finite these peaks are broadened due to the hybridization with the conduction electrons and, in addition, they are shifted to slightly higher energies. The spectral function for  $U = 0$  is shown qualitatively in the left part of Figure 2.4. The width of the broadening is  $\Delta_\sigma = -\text{Im}\Delta_\sigma(0)$ , and

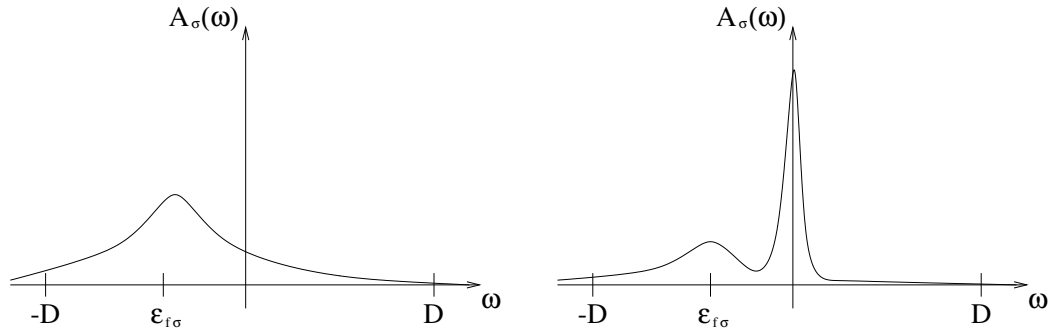


**Fig. 2.4:** Qualitative result for the impurity spectral function for  $V_{\mathbf{k}\sigma} > 0$  and  $U = 0$  (left) and in the Kondo regime for  $\epsilon_{f\sigma} + U \gg D$  (right).

in the case of a  $\mathbf{k}$ -independent hybridization it may be written as  $\Delta_\sigma = \pi\rho_\sigma(0)V_\sigma^2$ .

If, on the other hand,  $U$  is large, there are two scenarios: If  $\Delta_\sigma \geq |\epsilon_{f\sigma}|$ , the occupation number for the impurity is significantly less than 1, as there are constant transitions between the impurity level and empty conduction electron states close to the Fermi level. In this parameter regime the physics are dominated by charge fluctuations with a characteristic energy scale  $\Delta_\sigma$ .

Much more interesting is the Kondo regime, where  $|\epsilon_{f\sigma}|, \epsilon_{f\bar{\sigma}} + U \gg \Delta_\sigma$ . Charge fluctuations can be neglected in this case, the impurity is essentially singly occupied and a magnetic moment is formed. In this regime there is an effective antiferromagnetic exchange coupling of the impurity spin to the spins of the conduction electrons, and the Anderson model can be mapped onto the Kondo (or s-d) model by means of a Schrieffer-Wolff transformation. This model describes a local magnetic moment that is coupled to the conduction electron band by an exchange interaction  $J$ . In terms of the parameters of the Anderson model it is given by

$$J = -2V_\sigma^2 \frac{U}{|\epsilon_{f\sigma}|(\epsilon_{f\bar{\sigma}} + U)}. \quad (2.8)$$

Again, the hybridization is taken to be  $\mathbf{k}$ -independent. This interaction results in a sharp resonance at the Fermi energy in the spectral function of the impurity. This so-called Abrikosov-Suhl resonance (see Fig. 2.4) is a true many-body effect. It has to be created by processes with very small excitation energies. It is the antiferromagnetic coupling  $J$  that results in an effective spin-flip scattering of the conduction electrons at arbitrarily small energies. One of these processes is shown in Figure 2.5. An electron with spin  $\sigma$  leaves the impurity level and a

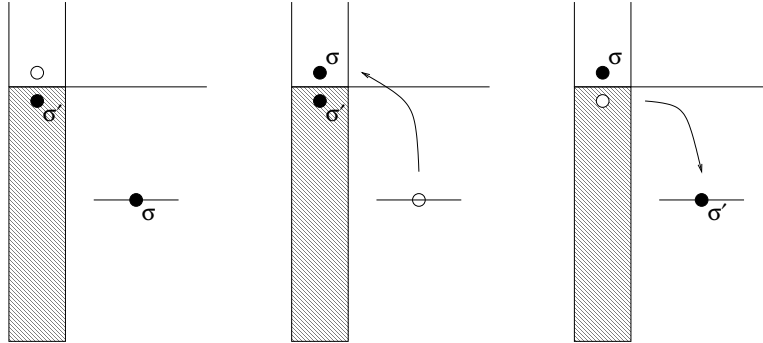


**Fig. 2.5:** *Scattering of a conduction electron spin due to the presence of the impurity level.*

conduction electron with opposite spin takes its place. This mechanism results in a dynamical screening of the impurity spin at low temperatures, and the ground state is a singlet. This effect will be discussed in detail in Chapter 4.

From perturbation theory up to third order in  $J$  a contribution to the resistivity proportional to  $\ln T$  is found. This, together with the phononic contribution that

decreases as the temperature is lowered, is sufficient to explain the resistivity minimum that has been observed in metals that contain magnetic impurities. However, this theory diverges as  $T \rightarrow 0$ , and a summation of all the logarithmically divergent terms in the perturbation expansion even results in a divergence at a finite temperature. It is clear that perturbation theory is not suited to describe this phenomenon at very low temperatures. While there is indeed a logarithmic increase in the resistivity observed at low temperatures, the resistivity saturates below a certain temperature  $T_K$ , the Kondo temperature, which has been found to be proportional to  $\exp(1/J\rho_\sigma(0))$ . This temperature is at the center of the theoretical description of models of magnetic impurities at low temperatures. All thermodynamic quantities scale with the Kondo temperature, the behavior of the system becomes universal. Both the appearance of the resonance at the Fermi level and the width of this resonance are determined by  $T_K$ .

From the above discussion it is clear that methods based on perturbation theory are in general ill suited to describe the impurity problem at very low temperatures. Therefore, a variety of other approaches have been developed [Hew93], the most prominent one being Wilson's numerical renormalization group theory. This is also the method used in this work for the solution of the effective impurity problem from the dynamical mean-field theory. The details of the NRG are discussed in Chapter 4.

### 3. THE DYNAMICAL MEAN-FIELD THEORY

The simple lattice models introduced in Chapter 2 still represent a complicated many-body problem, and an exact solution of these models is only possible in a few select cases. In recent years a powerful method has been developed to study strongly correlated electron systems, the dynamical mean-field theory [Met89, Pru95, Geo96]. This theory treats the dynamics due to the local correlations in an exact way, while non-local correlation effects are neglected. It becomes exact in the limit of infinite spatial dimensions  $d$  or lattice coordination number  $Z$ . Using this method, the lattice model can be mapped onto an effective impurity model, and the single-particle Green's function can be calculated in a self-consistent fashion. In addition, thermodynamic properties and two-particle correlation functions can also be calculated in the framework of this theory.

#### 3.1 The local approximation

What lies at the heart of a mean-field theory is the averaging over the spatial variations of an observable in the description of the interaction between a single site and the rest of the system. The most well-known example for this is the mean-field approximation for the Heisenberg model (2.3). There it is the fluctuations  $\mathbf{S}_j - \langle \mathbf{S}_j \rangle$  of the spins on different lattice sites that are neglected. This leads to the coupling of the spin at site  $i$  to an effective field generated by all the neighboring spins, and the resulting mean-field equations have to be solved self-consistently. It is clear that this description is the more accurate the higher the coordination number of the lattice is. Obviously fluctuations on a single site  $j$  are less important the more neighbors the spin at site  $i$  has. In the limit of infinite coordination number this theory becomes exact [Itz89]. This theory can also be applied to a system containing itinerant degrees of freedom like the Hubbard model (2.1). There are, however, two important differences. On the one hand, the correlations in this model are now purely local, and on the other hand the quantities of interest are no longer expectation values of some observable but rather single-particle Green's functions. It was the important realization that in the limit of infinite coordination number the self-energy is purely local [Met89],

$$\Sigma_{ij,\sigma}(z) = \Sigma_{ii,\sigma}(z) \delta_{ij} \quad \text{or} \quad \Sigma_{\sigma}(\mathbf{k}, z) = \Sigma_{\sigma}(z), \quad (3.1)$$

that allowed for the application of the mean-field formalism to these models.

However, in order to obtain a non-trivial model in the limit of infinite coordination number, the hopping matrix element  $t$  has to be rescaled, or else the kinetic energy of the system becomes infinite. Consider a hypercubic lattice in  $d$  dimensions with a lattice constant  $a$  that is taken to be 1. From the dispersion

$$\epsilon_{\mathbf{k}} = -2t \sum_{\nu=1}^d \cos k_{\nu} \quad (3.2)$$

and the general expression for the density of states

$$\rho(\epsilon) = \frac{1}{N} \sum_{\mathbf{k}} \delta(\epsilon - \epsilon_{\mathbf{k}}) \quad (3.3)$$

it follows from the central limit theorem that in the limit  $d \rightarrow \infty$  [Met89]

$$\rho(\epsilon) = \frac{1}{2t\sqrt{\pi d}} \exp \left[ - \left( \frac{\epsilon}{2t\sqrt{d}} \right)^2 \right]. \quad (3.4)$$

Only by rescaling  $t$  proportional to  $1/\sqrt{d}$  the kinetic energy term remains finite as  $d \rightarrow \infty$ . With the convention that

$$t = \frac{t^*}{2\sqrt{d}} \quad (3.5)$$

the result

$$\rho(\epsilon) = \frac{1}{\sqrt{\pi}} e^{-\epsilon^2} \quad (3.6)$$

for the free density of states is obtained. Unless otherwise noted, in all calculations for the hypercubic lattice the unit of energy is given by  $t^*$ .

It is important to note that, while the density of states (3.6) does not have any van Hove singularities, it is found to be quite similar to the density of states in two or three dimensions. From that it seems reasonable to assume that the results obtained from DMFT calculations are indeed relevant for the description of real materials. The main drawback in using the density of states (3.6) is that there are no band edges, which of course have to be present in a realistic density of states. This point will be addressed in a later part of this work.

The condition that the kinetic energy has to remain finite also results in a Green's function for the non-interacting system

$$G_{ij,\sigma}^0(z) = g_{\sigma}^0(z) \delta_{ij} - g_{\sigma}^0(z) t \sum_k G_{kj,\sigma}^0(z) \quad (3.7)$$

for nearest neighbors  $i$  and  $j$  or  $k$  and  $j$  respectively that has to be of the order of  $1/\sqrt{d}$ . Here  $g_{\sigma}^0(z) = (z + \mu)^{-1}$  is the free atomic Green's function. If the

self-energy diagrams in a diagrammatic expansion are now classified by orders of  $1/\sqrt{d}$ , it can be shown that in the limit  $d \rightarrow \infty$  only the local graphs contribute [Met89, Mue89]. This results in the expression (3.1) for the self-energy. The local Coulomb interaction, however, does not need to be rescaled and it leads to non-trivial dynamics even in the limit  $d \rightarrow \infty$ . The remaining many-body problem is still a very complicated one, and the details of the DMFT solution are presented in the following section.

## 3.2 Mapping onto an effective impurity problem

Due to the locality of the self-energy, the local Green's function of the lattice may be written as

$$G_{ii,\sigma}(z) = \frac{1}{N} \sum_{\mathbf{k}} \frac{1}{z + \mu - \Sigma_{\sigma}^L(z) - \epsilon_{\mathbf{k}}}. \quad (3.8)$$

Here  $N$  is the number of lattice sites and  $\mu$  is the chemical potential. The index  $L$  now denotes that the corresponding quantity is defined for the lattice model. As  $\Sigma_{\sigma}^L(z)$  is now independent of  $\mathbf{k}$ , the sum can be evaluated and one finds

$$G_{ii,\sigma}(z) = \frac{1}{z + \mu - \Sigma_{\sigma}^L(z) - \Delta_{\sigma}^L(z)}, \quad (3.9)$$

where

$$\Delta_{\sigma}^L(z) = \frac{\frac{1}{N} \sum_{\mathbf{k}} \epsilon_{\mathbf{k}}^2 G_{\sigma}(\mathbf{k}, z)}{1 - \frac{1}{N} \sum_{\mathbf{k}} \epsilon_{\mathbf{k}} G_{\sigma}(\mathbf{k}, z)} \quad (3.10)$$

and

$$G_{\sigma}(\mathbf{k}, z) = \frac{1}{z + \mu - \Sigma_{\sigma}^L(z) - \epsilon_{\mathbf{k}}}. \quad (3.11)$$

The hybridization function  $\Delta_{\sigma}^L(z)$  describes processes where an electron leaves the lattice site  $i$ , propagates on the lattice excluding the site  $i$  and eventually returns to the starting point. The self-energy  $\Sigma_{\sigma}^L(z)$  takes into account the Coulomb interaction between two electrons at the same site. As a result, the problem is now effectively a local one, where the effect of the remaining lattice sites is described by the dynamical, i.e. frequency-dependent, mean-field  $\Delta_{\sigma}^L(z)$ . This is illustrated in Figure 3.1.

From (3.9) the formal similarity between the local Green's function of the lattice and the impurity Green's function for the SIAM (see Sec. 2.2) is evident. Defining the local propagator  $\mathcal{G}_{ii,\sigma}$  that no longer contains the self-energy due to the correlations at site  $i$ ,

$$\mathcal{G}_{ii,\sigma}(z)^{-1} = G_{ii,\sigma}(z)^{-1} + \Sigma_{\sigma}^L(z), \quad (3.12)$$

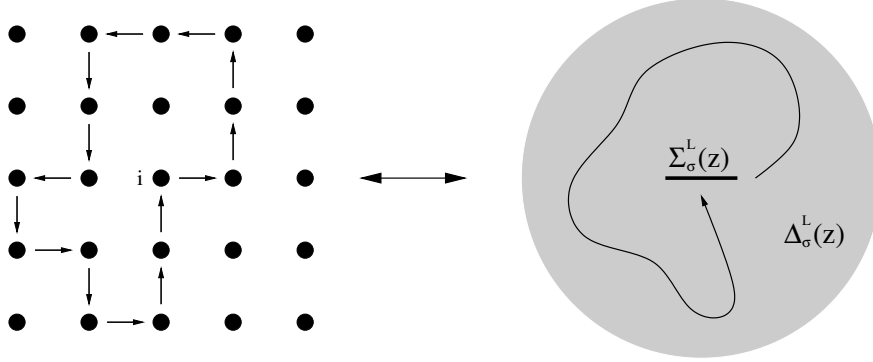


**Fig. 3.1:** Mapping of the Hubbard model onto an effectively local problem with a dynamical mean field  $\Delta_\sigma^L(z)$ .

the self-energy may be written as a functional of this propagator,

$$\Sigma_\sigma^L(z) = \mathcal{F} [\mathcal{G}_{ii,\sigma}(z)] . \quad (3.13)$$

For a detailed discussion of this, see [Pru95, Geo96]. At the same time, the self-energy of the single impurity problem is given by

$$\Sigma_\sigma(z) = \mathcal{F} [(z - \epsilon_{f\sigma} - \Delta_\sigma(z))^{-1}] \quad (3.14)$$

with the same functional  $\mathcal{F}$  as in (3.13). This leads to the following important realization: The self-energy of the lattice model can be calculated by solving an effective single impurity Anderson model. All that one has to do is to replace the hybridization of the impurity level with the conduction electron band  $\Delta_\sigma(z)$  by the quantity  $\Delta_\sigma^L(z)$  and the energy  $\epsilon_{f\sigma}$  by  $-\mu$ . Doing this allows for a self-consistent calculation of the self-energy of the lattice model.

The details of this self-consistent solution of the DMFT equations are shown in Fig. 3.2. One starts with an initial guess for the self-energy  $\Sigma_\sigma(z)$ . From that, the local Green's function (3.8) of the lattice is calculated. In practice this is done by converting the  $\mathbf{k}$ -sum into an integral over the energy. The only point at which the actual lattice structure enters in the DMFT calculation is therefore the form of the free density of states used to evaluate this integral. For the hypercubic lattice, the result is

$$\begin{aligned} G_{ii,\sigma}(z) &= \frac{1}{\sqrt{\pi}} \int_{-\infty}^{\infty} d\epsilon \frac{e^{-\epsilon^2}}{z - \epsilon + \mu - \Sigma_\sigma(z)} \\ &= -i\sqrt{\pi} w(z + \mu - \Sigma_\sigma(z)) \end{aligned}$$

with the Faddeeva function

$$w(z) = \frac{i}{\pi} \int_{-\infty}^{\infty} dt \frac{e^{-t^2}}{z - t} = e^{-z^2} \operatorname{erfc}(-iz)$$

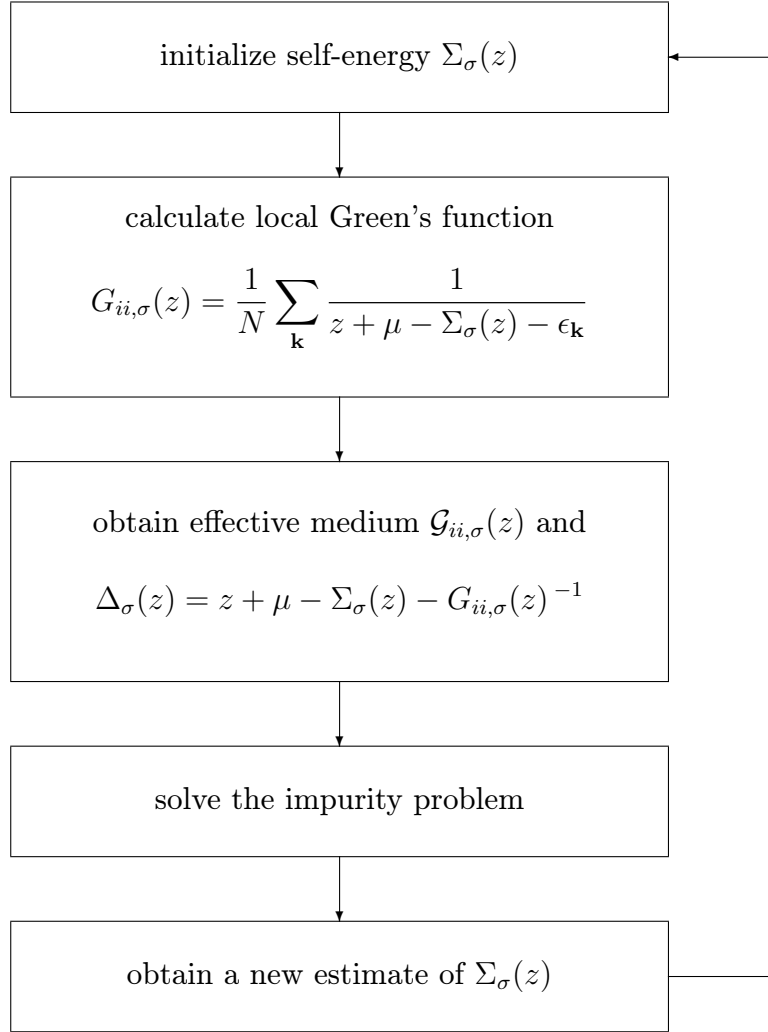


**Fig. 3.2:** *Self-consistent solution of the DMFT equations.*

for complex arguments  $z$  with  $\text{Im}z > 0$ . It has turned out that using this function is much more accurate than a direct numerical integration. Therefore, whenever possible, all the integrals appearing in the calculations for the hypercubic lattice presented in this work have been reduced to such a form.

From the local Green's function it is now possible to calculate the hybridization  $\Delta_\sigma(z)$  that enters into the solution of the impurity model. Once the impurity Green's function has been calculated, a new estimate for the self-energy can be extracted. How this is achieved is described in detail in Chapter 4. This procedure is repeated until convergence has been reached, i.e. the result for the self-energy does not change significantly from one step of the iteration to the next.

All the relevant quantities in the formalism presented so far can depend on the spin of the electrons. It is therefore possible to investigate symmetry-broken phases within the DMFT. There are various ways this can be implemented. One possibility is to calculate the  $\mathbf{q}$ -dependent magnetic susceptibility and see for which wave vectors  $\mathbf{q}$  it diverges. This is at present not possible when using the NRG to solve the impurity model. Instead, the presence of a phase with broken symmetry is detected by directly looking at the spectral function for both spin up and down. This is done in the following way: In the DMFT self-consistency cycle a small symmetry-breaking field is applied during the first few steps of the calculation. It is then removed, and the rest of the calculation is performed without an external field. As a result, the difference in the spectra for spin up and spin down either increases further and the converged solution has a finite magnetization, or the system relaxes back to a paramagnetic solution. It is also possible to search for an antiferromagnetic solution with this method. To that end one has to consider a bipartite lattice and apply a small staggered field during the first few steps of the calculation. The details of the DMFT formalism in this case are presented in the following section.

### 3.3 DMFT on a bipartite lattice

It is clear that in order to investigate the antiferromagnetic phase, the DMFT scheme presented above has to be somewhat modified. This is due to the fact that not all the lattice sites are equivalent anymore. In the simplest case, that of an antiferromagnetic Néel state, the DMFT equations have to be modified to account for two inequivalent sublattices  $A$  and  $B$  (see Fig. 3.3, left panel) with two different self-energies  $\Sigma_\sigma^A \neq \Sigma_\sigma^B$  [Bra91, Geo96].

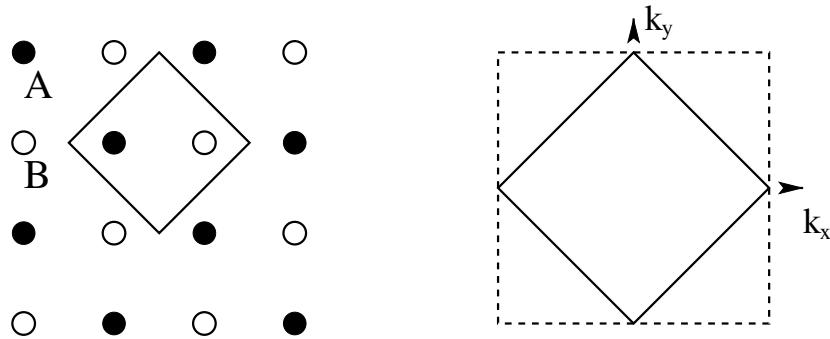


**Fig. 3.3:** *Left: Schematic view of the AB sublattice decomposition suitable for the treatment of the Néel state. Right: Magnetic Brillouin zone (MBZ), the first Brillouin zone of the Néel state.*

To this end, the operators  $a_{i\sigma}^{(\dagger)}$  and  $b_{i\sigma}^{(\dagger)}$  are introduced, which act on sublattice  $A$  and  $B$  respectively. In the case of nearest-neighbor hopping only, the kinetic part of the Hamiltonian (2.1) can be written as

$$H_t = -t \sum_{\langle i,j \rangle} \sum_{\sigma} \left( a_{i\sigma}^{\dagger} b_{j\sigma} + b_{j\sigma}^{\dagger} a_{i\sigma} \right) .$$

A Fourier transformation of this expression yields

$$H_t = \sum_{\sigma} \sum_{\mathbf{k}}' \Psi_{\mathbf{k}\sigma}^{\dagger} \begin{pmatrix} 0 & \epsilon_{\mathbf{k}} \\ \epsilon_{\mathbf{k}} & 0 \end{pmatrix} \Psi_{\mathbf{k}\sigma} ,$$

where the spinors

$$\Psi_{\mathbf{k}\sigma}^{\dagger} = \left( a_{\mathbf{k}\sigma}^{\dagger} , b_{\mathbf{k}\sigma}^{\dagger} \right) , \quad \Psi_{\mathbf{k}\sigma} = \begin{pmatrix} a_{\mathbf{k}\sigma} \\ b_{\mathbf{k}\sigma} \end{pmatrix}$$

have been introduced, and  $\epsilon_{\mathbf{k}}$  is the dispersion on the bipartite lattice. The prime on the sum indicates that the summation is over all values of  $\mathbf{k}$  in the *magnetic* Brillouin zone (MBZ) (see Fig. 3.3, right panel). Within this notation, the Green's function becomes a matrix in the two sublattices,

$$G_{\mathbf{k}\sigma}(z) = \begin{pmatrix} \zeta_{\sigma}^A & -\epsilon_{\mathbf{k}} \\ -\epsilon_{\mathbf{k}} & \zeta_{\sigma}^B \end{pmatrix}^{-1} , \quad (3.15)$$

where  $\zeta_{\sigma}^{A/B} = z + \mu - \Sigma_{\sigma}^{A/B}$ . Obviously, in the DMFT calculation these two different sublattices now have to be taken into account. This implies that there are now in principle two effective impurity problems that have to be solved in each step of the self-consistent calculation. However, in the Néel state, an additional simplification arises. In this case, all the properties at a site  $A$  of one sublattice for spin  $\sigma$  are exactly the same as the corresponding quantity at a site  $B$  from the other sublattice for opposite spin  $\bar{\sigma}$ . This is true in particular for the self-energy, and from now on the symmetry  $\zeta_{\sigma}^A = \zeta_{\bar{\sigma}}^B \equiv \zeta_{\sigma}$  of the Néel state will be used and the indices  $A$  and  $B$  can be dropped.

It is therefore enough to consider only one sublattice in the DMFT calculation, resulting again in only a single impurity model that has to be solved in each step. As a consequence, the self-consistent scheme shown in Fig. 3.2 can still be applied. The only difference is now the calculation of the local Green's function of the lattice model, as the nearest neighbors of a given site  $i$  are now all part of a different sublattice. This can easily be done by inverting the matrix in equation (3.15) and summing over  $\mathbf{k}$ . Converting this sum into an energy integral yields

$$G_{ii,\sigma}(z) = \zeta_{\sigma} \int_{-\infty}^{\infty} d\epsilon \frac{\rho(\epsilon)}{\zeta_{\uparrow}\zeta_{\downarrow} - \epsilon^2} . \quad (3.16)$$

For the hypercubic lattice, this can be written as

$$\begin{aligned} G_{ii,\sigma}(z) &= \frac{1}{\sqrt{\pi}} \frac{\zeta_{\bar{\sigma}}}{\sqrt{\zeta_{\uparrow}\zeta_{\downarrow}}} \int_{-\infty}^{\infty} d\epsilon \frac{e^{-\epsilon^2}}{\sqrt{\zeta_{\uparrow}\zeta_{\downarrow}} - \epsilon} \\ &= -i\sqrt{\pi} \frac{\zeta_{\bar{\sigma}}}{\sqrt{\zeta_{\uparrow}\zeta_{\downarrow}}} w\left(\sqrt{\zeta_{\uparrow}\zeta_{\downarrow}}\right) \end{aligned}$$

with the function  $w(z)$  as defined in Sec. 3.2. Again, this is done in order to improve the accuracy of the numerical calculations.

### Calculation of the optical conductivity

An appealing property of the DMFT is the possibility to calculate transport quantities in a very simple fashion. Due to the local nature of the theory, vertex corrections to the leading particle-hole bubble of the current-current correlation function vanish identically [Khu90, Pru95], i.e. one needs to calculate the bare bubble only. This has been extensively used to study the optical conductivity and various other transport properties in the paramagnetic phase of the Hubbard model [Pru95, Geo96, Fre01, Fre03]. On the other hand, up to now a comparable investigation of the optical properties of symmetry-broken phases, in particular the Néel state at half filling, has not been performed. The details of the necessary steps to carry out this calculation are presented below.

Using the formalism introduced in the previous section, the current operator is now written as

$$\mathbf{j} = e \sum_{\sigma} \sum_{\mathbf{k}} \Psi_{\mathbf{k}\sigma}^{\dagger} \begin{pmatrix} 0 & \mathbf{v}_{\mathbf{k}} \\ \mathbf{v}_{\mathbf{k}} & 0 \end{pmatrix} \Psi_{\mathbf{k}\sigma}$$

with  $\mathbf{v}_{\mathbf{k}} = \nabla_{\mathbf{k}}\epsilon_{\mathbf{k}}$  as usual. In the case of a lattice for which the conductivity tensor is diagonal, the elements  $\sigma_{ii} \equiv \sigma$  can be calculated from ( $d$  is the spatial dimension of the lattice)

$$d \cdot \sigma(\omega) = \Re e \frac{1}{i\omega} \sum_{l=1}^d \langle\langle j_l; j_l \rangle\rangle_{\omega+i\delta}$$

with the current-current correlation function

$$\begin{aligned} \langle\langle j_l; j_l \rangle\rangle_{i\nu} &= e^2 \sum_{\sigma\sigma'} \sum_{\mathbf{k}\mathbf{k}'} v_{\mathbf{k}}^l v_{\mathbf{k}'}^l \\ &\times \langle\langle a_{\mathbf{k}\sigma}^{\dagger} b_{\mathbf{k}\sigma} + b_{\mathbf{k}\sigma}^{\dagger} a_{\mathbf{k}\sigma}; a_{\mathbf{k}'\sigma'}^{\dagger} b_{\mathbf{k}'\sigma'} + b_{\mathbf{k}'\sigma'}^{\dagger} a_{\mathbf{k}'\sigma'} \rangle\rangle_{i\nu} . \end{aligned}$$

Again, due to the symmetry of the lattice, the index  $l$  can be dropped.

The most important simplification arises from the locality of the two-particle self-energies within the DMFT [Khu90, Bra91, Pru93]. Note that in the present

formulation the proper locality of the two-particle self-energies is still ensured, because in the DMFT as defined by eq. (3.15) no dynamical correlations between the  $A$  and  $B$  sublattices have been introduced. In analogy to the paramagnetic case this allows for the  $\mathbf{k}$  sums in diagrams containing two-particle self-energy insertions to be carried out independently at each vertex. Since the single particle propagators only depend on  $\mathbf{k}$  through the even function  $\epsilon_{\mathbf{k}}$  and the  $v_{\mathbf{k}}$  are of odd parity, the sum over their product vanishes.

As a result, the exact expression for the current-current correlation function in the DMFT is given by

$$\begin{aligned} \langle\langle j; j \rangle\rangle_{i\nu} &= -\frac{e^2}{\beta} \sum_{\omega_n} \sum_{\sigma} \sum'_{\mathbf{k}} v_{\mathbf{k}}^2 \\ &\times \left[ \langle\langle a_{\mathbf{k}\sigma}; a_{\mathbf{k}\sigma}^\dagger \rangle\rangle_{i\omega_n+i\nu} \langle\langle b_{\mathbf{k}\sigma}; b_{\mathbf{k}\sigma}^\dagger \rangle\rangle_{i\omega_n} \right. \\ &+ \langle\langle b_{\mathbf{k}\sigma}; b_{\mathbf{k}\sigma}^\dagger \rangle\rangle_{i\omega_n+i\nu} \langle\langle a_{\mathbf{k}\sigma}; a_{\mathbf{k}\sigma}^\dagger \rangle\rangle_{i\omega_n} \\ &+ \langle\langle b_{\mathbf{k}\sigma}; a_{\mathbf{k}\sigma}^\dagger \rangle\rangle_{i\omega_n+i\nu} \langle\langle b_{\mathbf{k}\sigma}; a_{\mathbf{k}\sigma}^\dagger \rangle\rangle_{i\omega_n} \\ &\left. + \langle\langle a_{\mathbf{k}\sigma}; b_{\mathbf{k}\sigma}^\dagger \rangle\rangle_{i\omega_n+i\nu} \langle\langle a_{\mathbf{k}\sigma}; b_{\mathbf{k}\sigma}^\dagger \rangle\rangle_{i\omega_n} \right] , \end{aligned}$$

with the inverse temperature  $\beta$  and fermionic Matsubara frequencies  $\omega_n$ .

In terms of the matrix elements of the Green's function (3.15) this can be written as

$$\begin{aligned} \langle\langle j; j \rangle\rangle_{i\nu} &= -\frac{e^2}{\beta} \sum_{\omega_n} \sum_{\sigma} \sum'_{\mathbf{k}} v_{\mathbf{k}}^2 \\ &\times \left[ G_{\mathbf{k}\sigma}^{AA}(i\omega_n+i\nu) G_{\mathbf{k}\sigma}^{BB}(i\omega_n) \right. \\ &+ G_{\mathbf{k}\sigma}^{BB}(i\omega_n+i\nu) G_{\mathbf{k}\sigma}^{AA}(i\omega_n) \\ &+ G_{\mathbf{k}\sigma}^{BA}(i\omega_n+i\nu) G_{\mathbf{k}\sigma}^{BA}(i\omega_n) \\ &\left. + G_{\mathbf{k}\sigma}^{AB}(i\omega_n+i\nu) G_{\mathbf{k}\sigma}^{AB}(i\omega_n) \right] \end{aligned}$$

where

$$G_{\mathbf{k}\sigma}^{AA}(z) = \frac{\zeta_{\bar{\sigma}}}{\zeta_{\sigma}\zeta_{\bar{\sigma}} - \epsilon_{\mathbf{k}}^2} , \quad G_{\mathbf{k}\sigma}^{BB}(z) = \frac{\zeta_{\sigma}}{\zeta_{\sigma}\zeta_{\bar{\sigma}} - \epsilon_{\mathbf{k}}^2}$$

and

$$G_{\mathbf{k}\sigma}^{BA}(z) = G_{\mathbf{k}\sigma}^{AB}(z) = \frac{\epsilon_{\mathbf{k}}}{\zeta_{\sigma}\zeta_{\bar{\sigma}} - \epsilon_{\mathbf{k}}^2} .$$

Next, the  $\mathbf{k}$  sum is converted into an energy integral by introducing the average squared velocity

$$\langle v^2 \rangle_{\epsilon} := \frac{1}{d \cdot N} \sum'_{\mathbf{k}} v_{\mathbf{k}}^2 \delta(\epsilon - \epsilon_{\mathbf{k}}) . \quad (3.17)$$

Making furthermore use of the spectral representation of the Green's functions, the frequency sum can be evaluated in a straightforward way, and finally the result for the optical conductivity in the Néel state is

$$\begin{aligned} \sigma(\omega) = & c \sum_{\sigma} \int_{-\infty}^0 d\epsilon \langle v^2 \rangle_{\epsilon} \int_{-\infty}^{\infty} d\omega' \frac{f(\omega') - f(\omega' + \omega)}{\omega} \\ & \times [A_{\sigma}(\epsilon, \omega') A_{\bar{\sigma}}(\epsilon, \omega' + \omega) + B_{\sigma}(\epsilon, \omega') B_{\sigma}(\epsilon, \omega' + \omega)] \end{aligned} \quad (3.18)$$

with

$$A_{\sigma}(\epsilon, \omega) = -\frac{1}{\pi} \Im m G_{\sigma}^{AA}(\epsilon, \omega + i\delta)$$

and

$$B_{\sigma}(\epsilon, \omega) = -\frac{1}{\pi} \Im m G_{\sigma}^{AB}(\epsilon, \omega + i\delta) .$$

Here  $f(\omega)$  is the Fermi function and  $c$  collects the various constants. Note that the form (3.18) is reminiscent of the result found in the case of superconductivity, which is discussed at length e.g. in the book by Mahan [Mah90]. Consequently, one can expect to obtain similar features from the evaluation of (3.18).

In order to proceed with the calculation of the conductivity, it is necessary to specify the actual lattice structure and the corresponding non-interacting dispersion in (3.17). For the hypercubic lattice [Pru93],  $\langle v^2 \rangle_{\epsilon} \propto \rho(\epsilon)$  is a simple Gaussian, and the integration over  $\epsilon$  can be performed analytically. For the details of this calculation, see Appendix B.

## 4. SOLUTION OF THE EFFECTIVE IMPURITY PROBLEM

### 4.1 The Numerical Renormalization Group

Wilson's numerical renormalization group theory (NRG) has originally been developed to solve the well-known Kondo problem [Wil75]. This problem [Hew93] is associated with the observation that in many metals at very low temperatures the resistance does not decrease monotonously, but instead it starts to increase below a certain temperature before it eventually saturates. It is now known that this behavior is a result of the presence of magnetic impurities such as iron in the metal. However, the theoretical description of this phenomenon has turned out to be remarkably complex. While Kondo had been able to explain the resistance minimum by doing perturbation theory for the s-d model (also known as the Kondo model), he obtained a logarithmically divergent result for the resistivity at very low temperature [Kon64]. Such a divergence is encountered frequently when a perturbatory approach is used to describe systems that do not possess a characteristic energy scale. In the case of the Kondo problem, it is the fact that all the different energy scales are of equal importance in accurately describing the low temperature properties of the system that results in the divergence.

A widely used approach to treat this kind of problem is to set up a so-called renormalization group transformation. The idea behind this formalism is that the different energy scales are coupled to each other. This allows for an iterative solution, where after a given step in this scheme there remains an effective Hamiltonian describing those energy scales which have not been taken into account yet. Thus, a renormalization group transformation corresponds to the mapping  $R$  of a Hamiltonian  $H(\mathbf{K})$  containing a set of couplings  $\mathbf{K} = (K_1, K_2, \dots)$  onto a Hamiltonian of the same form but with a new set of parameters  $\mathbf{K}'$ . This new, effective Hamiltonian then describes the physics of the problem at hand on a lower energy scale. In general, a parameter  $\Lambda$  is introduced which relates the old energy scale to the new one. Formally this transformation can be written as

$$H(\mathbf{K}') = R_\Lambda\{H(\mathbf{K})\} \quad \text{or} \quad \mathbf{K}' = R_\Lambda(\mathbf{K}). \quad (4.1)$$

An important concept in the implementation of this formalism is the existence

of fixed points, that is, a set of parameters  $\mathbf{K}^*$  that fulfills the condition

$$R_\Lambda(\mathbf{K}^*) = \mathbf{K}^* . \quad (4.2)$$

The trajectories that are generated by a repeated transformation in general flow towards or away from such fixed points, depending on whether the fixed point is a *stable* or an *unstable* one. Knowledge of the fixed points of the renormalization group transformation allows for the determination of many important physical properties of the system under investigation. Details of the formal theory of these fixed points can be found e.g. in the review article by Wilson and Kogut [Wil74].

The renormalization group theory as it has been formulated by Gell-Mann and Low [Gel54] allows for an efficient summation of diagrams in a perturbation expansion. However, it has the disadvantage that it does not reveal any information regarding the influence of the different relevant energy scales on the physics. It was the groundbreaking work by Wilson [Wil75], who developed a non-perturbative theory by setting up a renormalization group transformation and solving it numerically, that overcame this shortcoming. This numerical renormalization group theory allowed for the investigation of a variety of problems which could not be accessed by perturbation theoretical methods. In his investigations of the Kondo model, Wilson could show that it is the screening of the magnetic impurity below a certain temperature  $T_K$  that accounts for the resistivity to saturate as the temperature goes to zero. In subsequent works by Krishna-murthy, Wilkins and Wilson [Kri80], the single impurity Anderson model (2.4) has also been extensively studied. The methods described there form the basis of the approach to solving the effective impurity problem which is described in this chapter. To that end, two main extensions of the original work have to be implemented. For one thing, as the main point of interest in this work is the investigation of symmetry-broken phases, the NRG formalism must be modified to take into account the spin degree of freedom (see Sec. 4.2). The second aspect is the calculation of dynamical quantities such as the single particle self-energy from the NRG. This is in itself a complicated problem, but considerable progress has been made in recent years (for a review see [Bul00]). However, it has turned out that the inclusion of a magnetic field or the treatment of spin-dependent problems in the framework of the DMFT introduces an additional complication when it comes to the calculation of dynamical properties. This will be discussed in detail in Section 4.3.

## 4.2 Generalization for problems with broken symmetry

All the important steps in applying the NRG to the single impurity Anderson model are described in the work of Wilson [Wil75] and Krishna-murthy et al. [Kri80]. However, there the density of states of the conduction band electrons

was assumed to be constant. It is clear that if this approach is to be used for the solution of an effective impurity problem in the DMFT, this restriction has to be lifted. It has been shown that this is indeed possible [Bul94, Bul97], and a detailed description can be found in these references. The second extension that has to be implemented is the inclusion of the spin degree of freedom into the NRG formalism. This is inevitable if the DMFT is used to investigate phases with broken symmetry, where the effective medium is different for spin up and spin down. Although this is straightforward for the most part, there are some important differences in the actual implementation of the NRG. Therefore, the most important steps of the formalism will be presented in the following.

The starting point is the Hamiltonian of the single impurity Anderson model

$$\begin{aligned}
 H = & \sum_{\sigma} \epsilon_{f\sigma} f_{-1\sigma}^{\dagger} f_{-1\sigma} + U f_{-1\uparrow}^{\dagger} f_{-1\uparrow} f_{-1\downarrow}^{\dagger} f_{-1\downarrow} \\
 & + \sum_{k\sigma} \epsilon_{k\sigma} c_{k\sigma}^{\dagger} c_{k\sigma} + \sum_{k\sigma} V_{k\sigma} (f_{-1\sigma}^{\dagger} c_{k\sigma} + c_{k\sigma}^{\dagger} f_{-1\sigma}). \quad (4.3)
 \end{aligned}$$

This Hamiltonian has already been discussed in Section 2.2. It is convenient to introduce the index  $-1$  to label the operators acting on the impurity site. In addition, both the conduction electron energies  $\epsilon_{k\sigma}$  and the hybridization  $V_{k\sigma}$  are assumed to depend only on the absolute value of the wave vector  $k$ . The Hamiltonian (4.3) now has to be cast into a form that allows for the definition of a renormalization group transformation and, subsequently, its iterative solution. To that end, it is useful to change to the energy representation, with the energies of the conduction band electrons ranging from  $-D$  to  $D$ . From now on, all energies will be given in terms of the half-bandwidth  $D$ .

### Logarithmic Discretization

As stated before, it is the presence of arbitrarily small energy scales in the impurity problem that presents the main difficulty in solving this problem. To be able to account for these small energy scales, one introduces a logarithmic discretization of the conduction band, i.e. it is divided into a series of intervals  $[-\Lambda^{-n}, -\Lambda^{-(n+1)}[$  and  $]\Lambda^{-(n+1)}, \Lambda^{-n}]$  ( $n = 0, 1, 2, \dots$ ) with a parameter  $\Lambda > 1$ . This is shown in Figure 4.1. The quantity  $\Delta_{\sigma}(\epsilon)$  that is shown there is defined as  $\Delta_{\sigma}(\epsilon) = \pi V_{\sigma}^2(\epsilon) \rho_{\sigma}(\epsilon)$ , where  $\rho_{\sigma}(\epsilon)$  is the free conduction electron density of states and the hybridization  $V_{\sigma}$  is assumed to be independent of  $k$ .

This allows for the Hamiltonian of the single impurity model to be written in a discretized way, where the electrons with continuous energies from  $-1$  to  $1$  are now represented by a set of electrons with discrete energies  $\pm\Lambda^{-n}$  [Bul97]. Clearly, it is the electrons with energies close to the Fermi edge which are sampled

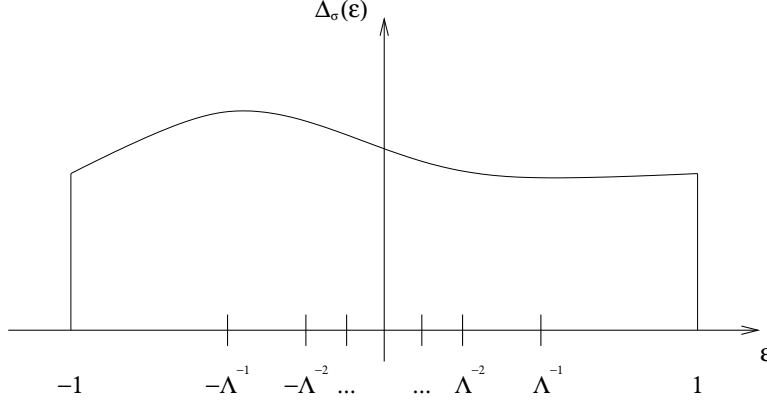


**Fig. 4.1:** *Logarithmic discretization of the conduction band.*

well using this method. Since they are the ones determining the physics at very low temperatures, this turns out to be a good approximation.

The motivation for this approach is that it is now possible to clearly differentiate between the different energy scales present in the problem. This point has already been addressed in the previous section. The next step is to find the couplings between the different energy scales to be able to apply the concepts of the renormalization group to the single impurity model.

### Mapping onto a linear chain

As a result of the discretization described above, in the Hamiltonian there is now a term coupling the impurity to a new fermionic operator  $f_{0\sigma}^{(\dagger)}$ , which essentially denotes the conduction electron field operator at the impurity site (for details, see [Kri80]). The conduction electron term at this point is still diagonal. Now, a unitary transformation of this term is carried out onto a new set of conduction electron operators  $f_{n\sigma}^{(\dagger)}$ , under the constraint that  $f_{0\sigma}^{(\dagger)}$  remains invariant under the transformation. This inevitably results in couplings between these new operators, and, in the simplest case, only those operators with indices differing by  $\pm 1$  are coupled to each other. The Hamiltonian is now written as

$$\begin{aligned}
 H &= \sum_{\sigma} \epsilon_{f\sigma} f_{-1\sigma}^{\dagger} f_{-1\sigma} + U f_{-1\uparrow}^{\dagger} f_{-1\uparrow} f_{-1\downarrow}^{\dagger} f_{-1\downarrow} \\
 &+ \sum_{n\sigma} \left( \epsilon_{n\sigma} f_{n\sigma}^{\dagger} f_{n\sigma} + t_{n\sigma} (f_{n\sigma}^{\dagger} f_{n+1\sigma} + f_{n+1\sigma}^{\dagger} f_{n\sigma}) \right) \\
 &+ \sum_{\sigma} t_{-1\sigma} (f_{-1\sigma}^{\dagger} f_{0\sigma} + f_{0\sigma}^{\dagger} f_{-1\sigma}). \tag{4.4}
 \end{aligned}$$

The local part of the Hamiltonian in the first line is unchanged. The second part

is the conduction electron contribution, written in terms of the new operators  $f_{n\sigma}^{(\dagger)}$ , and the last term describes the coupling between the impurity and the conduction electrons. The parameters  $\epsilon_{n\sigma}$ ,  $t_{n\sigma}$  and  $t_{-1\sigma}$  can be calculated numerically from a given conduction electron density of states. Essentially, this is done by using a tridiagonalization procedure, details of which can again be found in the articles by Krishna-murthy et al. and Wilson, as well as in the book by Hewson. While this can be done analytically for a constant density of states, in case of an arbitrary  $\Delta_\sigma(\epsilon)$  these calculations have to be done numerically. The important feature in both the analytic and numeric calculation of these parameters is that the size of the couplings is exponentially decreasing, i.e. the  $t_{n\sigma}$  are found to be proportional to  $\Lambda^{-n/2}$ . The on-site energies  $\epsilon_{n\sigma}$  vanish even more rapidly as  $n$  increases.

Equation (4.4) corresponds to the Hamiltonian of a semi-infinite linear chain with on-site energies  $\epsilon_{n\sigma}$  and matrix elements  $t_{n\sigma}$  that describe the hopping between

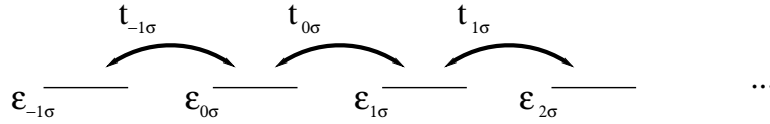


**Fig. 4.2:** Mapping onto a semi-infinite linear chain.

site  $n$  und site  $n + 1$  (see Fig. 4.2). The impurity site is at the beginning of the chain, while the rest of the sites correspond to the new conduction electron states. Both the on-site energies and the hopping matrix elements can depend on spin. Having rewritten the original Hamiltonian (4.3) in this particular form, it is now possible to set up a renormalization group transformation and solve it.

### Iterative Diagonalization

In order to solve the Hamiltonian (4.4) of the linear chain, one defines a series of Hamiltonians

$$\begin{aligned}
 H_N = & \Lambda^{(N-1)/2} \left[ \sum_{\sigma} \epsilon_{f\sigma} f_{-1\sigma}^{\dagger} f_{-1\sigma} + U f_{-1\uparrow}^{\dagger} f_{-1\uparrow} f_{-1\downarrow}^{\dagger} f_{-1\downarrow} \right. \\
 & \left. + \sum_{\sigma} \sum_{n=-1}^{N-1} \left( \epsilon_{n+1\sigma} f_{n+1\sigma}^{\dagger} f_{n+1\sigma} + t_{n\sigma} (f_{n\sigma}^{\dagger} f_{n+1\sigma} + h.c.) \right) \right] \quad (4.5)
 \end{aligned}$$

that converges to (4.4) in the limit  $N \rightarrow \infty$ ,

$$H = \lim_{N \rightarrow \infty} \Lambda^{-(N-1)/2} H_N. \quad (4.6)$$

$H_N$  then describes a chain of length  $N + 2$ , and

$$H_{-1} = \Lambda^{-1} \sum_{\sigma} \epsilon_{f\sigma} f_{-1\sigma}^{\dagger} f_{-1\sigma} + U f_{-1\uparrow}^{\dagger} f_{-1\uparrow} f_{-1\downarrow}^{\dagger} f_{-1\downarrow} \quad (4.7)$$

is the Hamiltonian of the impurity alone and the starting point for the iterative diagonalization procedure. The scaling of  $H_N$  with  $\Lambda^{(N-1)/2}$  is introduced so that the lowest eigenvalues of  $H_N$  are of the order of one.

The iterative solution is carried out in the following way: One starts with a diagonalized chain of length  $N$ , for which all the eigenvalues are known, and adds the coupling of this chain to the site  $N + 1$ . This new chain is then again diagonalized, one more site is added, and the procedure is repeated until the energy scales represented by additional sites in the chain are small enough to be deemed irrelevant. The central aspect of this calculation is the relation between two successive Hamiltonians,

$$H_{N+1} = \Lambda^{1/2} H_N + \Lambda^{N/2} \sum_{\sigma} \left( \epsilon_{N+1\sigma} f_{N+1\sigma}^{\dagger} f_{N+1\sigma} + t_{N\sigma} (f_{N\sigma}^{\dagger} f_{N+1\sigma} + h. c.) \right). \quad (4.8)$$

Equation (4.8) represents a renormalization group transformation as it has been introduced in Sec. 4.1.

All that is necessary to solve  $H_{N+1}$  are the eigenvalues  $E_N(r)$  of  $H_N$  and the matrix elements  ${}_N \langle r | f_{N\sigma}^{\dagger} | r' \rangle_N$  of the conduction electron operator  $f_{N\sigma}^{\dagger}$ , evaluated in the basis of the eigenstates to  $H_N$ . The index  $r$  is introduced to label the different eigenstates of  $H_N$ . From these one can obviously construct a basis

$$\begin{aligned} |r, 1\rangle &= |r\rangle_N \\ |r, 2\rangle &= f_{N+1\uparrow}^{\dagger} |r\rangle_N \\ |r, 3\rangle &= f_{N+1\downarrow}^{\dagger} |r\rangle_N \\ |r, 4\rangle &= f_{N+1\uparrow}^{\dagger} f_{N+1\downarrow}^{\dagger} |r\rangle_N \end{aligned} \quad (4.9)$$

for the Hilbert space of  $H_{N+1}$ . By diagonalizing the matrix  $\langle r, i | H_{N+1} | r', j \rangle$  in this representation one obtains the eigenstates  $|w\rangle_{N+1}$  and the corresponding eigenvalues  $E_{N+1}(w)$ . At the same time the matrix elements  ${}_{N+1} \langle w | f_{N+1\sigma}^{\dagger} | w' \rangle_{N+1}$ , which are necessary for the next step of the diagonalization procedure, can be calculated.

As the main numerical effort goes into the diagonalization of the matrix of  $H_{N+1}$ , it is essential for the practical implementation of the above iteration scheme to make use of the symmetries of the Hamiltonian. In doing so, one can carry out the diagonalization in each of the subspaces belonging to a particular set of good quantum numbers separately, thus drastically reducing the size of the matrices that have to be diagonalized. It can be easily shown that the operator

$$Q_N = \sum_{\sigma} \sum_{n=-1}^N (f_{n\sigma}^{\dagger} f_{n\sigma} - 1), \quad (4.10)$$

which denotes the particle number, or to be more precise, the difference from half filling of the chain of length  $N$ , commutes with  $H_N$ . The same is true for the

operator of the total spin

$$\mathbf{S}_N = \frac{1}{2} \sum_{\sigma\sigma'} \sum_{n=-1}^N f_{n\sigma}^\dagger \boldsymbol{\tau}_{\sigma\sigma'} f_{n\sigma'}, \quad (4.11)$$

where the  $\boldsymbol{\tau} = (\tau_x, \tau_y, \tau_z)$  are the Pauli matrices. To see that this is true even in the presence of a magnetic field or spin-dependent couplings between the sites of the chain, it is best to rewrite the terms in (4.5) in the following way: The first term can be written as

$$\sum_{\sigma} \epsilon_{f\sigma} f_{-1\sigma}^\dagger f_{-1\sigma} = \sum_{\sigma\sigma'} \epsilon_f f_{-1\sigma}^\dagger \delta_{\sigma\sigma'} f_{-1\sigma'} + \sum_{\sigma\sigma'} \Delta\epsilon_f f_{-1\sigma}^\dagger \tau_{z,\sigma\sigma'} f_{-1\sigma'},$$

with the definitions  $\epsilon_f := (\epsilon_{f\uparrow} + \epsilon_{f\downarrow})/2$  and  $\Delta\epsilon_f := (\epsilon_{f\uparrow} - \epsilon_{f\downarrow})/2$ . The terms containing  $\epsilon_{n+1\sigma}$  and  $t_{n\sigma}$ , respectively, can be written in formally the same way. All the spin-dependent quantities that appear in  $H_N$  can be expressed in terms of the Pauli matrix  $\tau_z$ . It is therefore clear that  $H_N$  commutes with both  $\mathbf{S}_N^2$  and  $S_{Nz}$  even when the spin degeneracy has been lifted.

In the standard implementation of the NRG for the Anderson model [Kri80] only the paramagnetic case has been considered. In that case, the eigenstates of the Hamiltonian usually are designated using the good quantum numbers  $Q$ ,  $S$  and  $S_z$ , and the numerical diagonalization is carried out in each  $(Q, S, S_z)$  subspace separately. A further simplification arises due to the degeneracy of the subspaces with the same  $Q$  and  $S$  but different  $S_z$  quantum numbers. As a consequence, it is enough to consider only the quantum numbers  $Q$  and  $S$  and to use so-called reduced matrix elements of the operators  $f_{N\sigma}^\dagger$  that are independent of  $S_z$ . This results in a considerable reduction of the numerical effort. It is therefore natural to try to implement the same formalism in the magnetic case, where all the  $(Q, S, S_z)$  subspaces are indeed different and have to be treated separately. This is possible in principle, because, as discussed above, both  $S$  and  $S_z$  are still good quantum numbers. It has turned out, however, that a practical implementation of the formalism in that case is not possible. The difficulty lies in the construction of the eigenstates of  $\mathbf{S}_{N+1}^2$  for the next step of the iteration. Not only is this quite complicated, but it also requires that all the subspaces are complete. It is one of the fundamental restrictions in carrying out the iterative diagonalization as described above that this can no longer be guaranteed after only a few steps [Zit00].

The reason for this is the exponential growth of the total number of states when adding additional sites to the chain of conduction electron states. It can be seen from (4.9) that this number increases by a factor of 4 each time a site is added. For  $N \gtrsim 5$  it is no longer possible to keep all the eigenstates of  $H_N$ , and one is restricted to only a fixed number of states in each step. In practice only around 1000 states, those with the lowest-lying energy eigenvalues, are used to construct

the basis states for the next step. This is a good approximation, as it is precisely those states that determine the low-energy behavior of the system. In other words, since each successive step in the diagonalization corresponds to smaller and smaller energy scales, the states with high energies in step  $N$  will not affect the states of the chain of length  $N + 1$  by too much. It is clear that this requires the parameter  $\Lambda$  not to be too close to 1. As discussed before, this parameter relates the energy scales of two succeeding steps, and obviously the error due to the truncation of the Hilbert space is larger when  $\Lambda$  is smaller. In practice values of  $\Lambda$  between 1.5 and 2.5 have turned out to be a good choice.

As a result of what has been discussed so far, the eigenstates are now labelled using only the two quantum numbers  $Q$  and  $S_z$ . In this formalism, the eigenstates  $|Q, S_z\rangle_{-1}$  of the impurity are given by

$$\begin{aligned} |-1, 0\rangle_{-1} &= |0\rangle \\ |0, -1/2\rangle_{-1} &= f_{-1\downarrow}^\dagger |0\rangle \\ |0, 1/2\rangle_{-1} &= f_{-1\uparrow}^\dagger |0\rangle \\ |1, 0\rangle_{-1} &= f_{-1\uparrow}^\dagger f_{-1\downarrow}^\dagger |0\rangle, \end{aligned}$$

and the corresponding eigenenergies are

$$\begin{aligned} E_{-1}(-1, 0) &= 0 \\ E_{-1}(0, -1/2) &= \Lambda^{-1}\epsilon_{f\downarrow} \\ E_{-1}(0, 1/2) &= \Lambda^{-1}\epsilon_{f\uparrow} \\ E_{-1}(1, 0) &= \Lambda^{-1}(\epsilon_{f\downarrow} + \epsilon_{f\uparrow} + U). \end{aligned}$$

The matrix elements of  $f_{-1\sigma}^\dagger$  which are needed for the first step in the iterative diagonalization can also be easily calculated and are given in Appendix A.

Once the Schrödinger equation for the chain of length  $N$

$$H_N |Q, S_z, r\rangle_N = E_N(Q, S_z, r) |Q, S_z, r\rangle_N \quad (4.12)$$

has been solved, a basis for the chain of length  $N + 1$  characterized by the quantum numbers  $Q$  and  $S_z$  can be constructed,

$$\begin{aligned} |Q, S_z, r, 1\rangle_{N+1} &= |Q + 1, S_z, r\rangle_N \\ |Q, S_z, r, 2\rangle_{N+1} &= f_{N+1\uparrow}^\dagger |Q, S_z - 1/2, r\rangle_N \\ |Q, S_z, r, 3\rangle_{N+1} &= f_{N+1\downarrow}^\dagger |Q, S_z + 1/2, r\rangle_N \\ |Q, S_z, r, 4\rangle_{N+1} &= f_{N+1\uparrow}^\dagger f_{N+1\downarrow}^\dagger |Q - 1, S_z, r\rangle_N. \end{aligned} \quad (4.13)$$

In this basis the matrix of  $H_{N+1}$  is first built and then diagonalized. This can be done in each of the  $(Q, S_z)$  subspaces separately. As a result, one obtains the

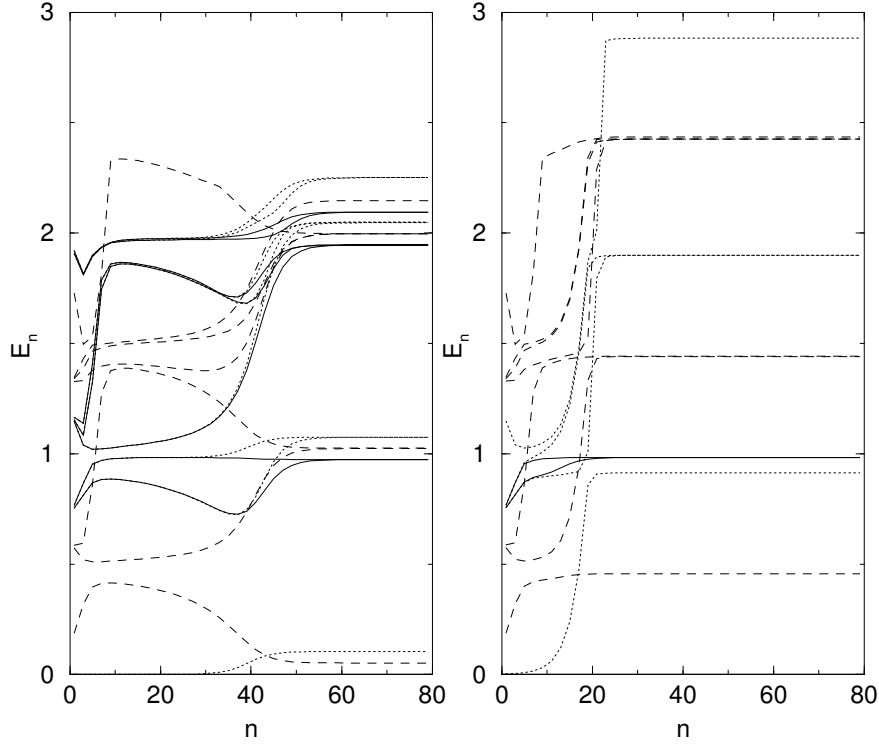


**Fig. 4.3:** Energy spectrum for the linear chain in the presence of a magnetic field  $H$  at the impurity site. The lowest-lying eigenenergies with  $Q = 0, S_z = 1/2$  (solid lines),  $Q = 0, S_z = -1/2$  (dotted lines) and  $Q = \pm 1, S_z = 0$  (dashed lines) are shown for  $H < T_K$  (left) and  $H \gg T_K$  (right). The different fixed points for large  $n$  can clearly be identified.

eigenstates  $|Q, S_z, w\rangle_{N+1}$  of  $H_{N+1}$ , together with the corresponding eigenenergies. The details of this can be found in the appendix.

In Figure 4.3 the lowest-lying eigenstates of the linear chain in the presence of a magnetic field at the impurity site are shown as a function of the iteration number  $n$ . The states are labelled by the quantum numbers  $Q$  and  $S_z$ , and all energies are measured with respect to the ground state energy. In addition, the energies have been rescaled to be of the order of 1 in each step of the iteration. Only the iterations with odd  $n$  are shown. This is an important aspect of the NRG formalism. The quantum numbers of the states of the chain change between even and odd values of  $n$ . It can easily be seen that the states shown in Fig. 4.3 can not exist for a chain with even  $n$ . For example,  $n = 0$  corresponds to the impurity plus one additional site, and a state with  $Q = 0$  implies that two electrons are present. Clearly, a value of  $S_z = \pm 1/2$  is not possible. Strictly speaking, the fixed points of the renormalization group transformation  $R_\Lambda$  are fixed points of

$R_{\Lambda}^2$ , and this implies that  $E_n = E_{n+2}$ . It will be shown later that this is also of importance when calculating the spectral function, in particular in the presence of a magnetic field.

A detailed discussion of the fixed points of the renormalization group transformation along the lines of [Kri80] is beyond the scope of this work. What is important to note is that the relevant energy scale in the presence of a magnetic field is still the Kondo temperature  $T_K$ . For a field  $H < T_K$  there is a transition from the local moment fixed points at intermediate values of  $n$  to the strong coupling fixed points at large  $n$ . This corresponds to the formation of a singlet from the impurity spin and the spin on the first site of the conduction electron chain at low temperatures. The applied magnetic field simply results in a splitting of the energies of the states with  $Q = 0$  and  $S_z = \pm 1/2$  (left panel of Fig. 4.3). Otherwise the energy spectrum shows the same qualitative behavior as in the paramagnetic case [Kri80]. This is different for  $H \gg T_K$ . The energies do not flow to the strong coupling fixed points anymore, but instead the local moment fixed points are stable even at low temperatures. This can be seen most clearly by looking at the states with  $Q = \pm 1$  and  $S_z = 0$  (right panel of Fig. 4.3). This situation corresponds to an isolated spin at the impurity site that is effectively decoupled from the rest of the conduction electron chain. The changes due to the magnetic field will be discussed further in the section describing the calculation of dynamical quantities from the spectra shown in Fig. 4.3.

There are two drawbacks to the implementation of the iterative diagonalization using only the quantum numbers  $Q$  and  $S_z$  as described above. For one thing, it is clear that the matrices that have to be diagonalized now are in general larger than those in the paramagnetic case. This results in an increase in computational time, however, with ever advancing computer power, this can easily be compensated. The second point is that in general the spectrum of the Hamiltonian is now much more dense, because there are simply more non-degenerate states that have to be treated separately. As a result, the energy of the highest state in the spectrum that is kept for the construction of the new basis is now lower than it is in the paramagnetic case with the same number of states kept. For the reasons detailed above, this results in a less accurate calculation of the new basis states. This can be overcome by keeping more states, also at the cost of increased computational effort. Comparisons with NRG calculations done in the standard way showed very good agreement for the paramagnetic case even if only moderately more states were kept. As a result, the generalization of the NRG method to include spin-dependent couplings can be considered just as reliable when it comes to the description of quantum impurity problems at low temperatures as the original method.

Once the spectrum of  $H_N$  is known, it is also possible to calculate static properties such as the magnetic susceptibility and the specific heat of the impurity [Kri80].

This is done using the statistical operator of the chain of length  $N$

$$\begin{aligned}\hat{\rho}_N &= \frac{1}{Z_N} \sum_n e^{-E_n/k_B T_N} |n\rangle_N \langle n| \\ Z_N &= \sum_n e^{-E_n/k_B T_N},\end{aligned}\tag{4.14}$$

where  $Z_N$  is the corresponding partition function. The eigenstates of the chain of length  $N$  are now denoted by  $|n\rangle_N$  and the eigenvalues by  $E_n$ . The temperature  $T_N$  is defined by  $T_N = \Lambda^{(N-1)/2} T$ , as a result of the relation (4.6). It is important to note that calculating the properties of the impurity at a given temperature  $T$  formally requires to consider the limit  $N \rightarrow \infty$ . Considering only a chain of length  $N$  and calculating the properties of this chain at the desired temperature  $T$  is an approximation. However, it has been shown by Wilson that the error is of the order of  $O(\Lambda^{-(N+1)/2}/k_B T)$  or, equivalently,  $O(\beta_N/\Lambda)$ . This implies that for an accurate calculation of the impurity properties at this temperature, it is sufficient to consider a large enough  $N$ .

Of course, one is usually interested in a whole range of temperatures when calculating thermodynamic properties. Therefore, in order to be consistent, what is done in practice is to fix the value  $\beta_N$  and carry out the calculations for chains of increasing length  $N$ . Note that in doing so each chain of length  $N$  now corresponds to a discrete temperature  $T_N$ . In other words, what lies at the heart of the calculation of the static properties for the single impurity problem is the following: Instead of considering the limit  $N \rightarrow \infty$ , i.e. a chain of infinite length, the calculations are carried out for only a fixed number of sites, which represent the full system at the temperature  $T_N$  within a given accuracy. Obviously it is desirable to choose  $\beta_N$  as small as possible (as  $\Lambda$  is usually around 2). However, a precise evaluation of the sums in (4.14) then requires knowledge of the higher excited states of  $H_N$ , but due to the truncation of the Hilbert space in each step this information is not available. In practice  $\beta_N$  is chosen only somewhat smaller than 1, and all the calculations in this work have been done using a value of  $\beta_N = 0.727$ .

The thermodynamic expectation value of an operator  $A$  for the chain of length  $N$  is given by the trace  $\text{Tr} \hat{\rho}_N A$ . All that is needed for the actual calculation is the matrix elements of the operator  $A$  in the basis of eigenstates of the chain of length  $N$ . For the quantities considered in this work, namely the occupation number  $n_{f\sigma}$  and the double occupancy  $n_{f\uparrow} n_{f\downarrow}$  of the impurity, they can easily be obtained in each step of the calculation. This is carried out along the lines of the calculation of the matrix elements of  $f_{-1\sigma}^\dagger$  that is presented in the appendix.

Figure 4.4 shows a comparison of the calculation of the impurity magnetization  $m = n_{f\uparrow} - n_{f\downarrow}$  for the symmetric Anderson model in the presence of small magnetic field. The parameters used are  $\Lambda = 2$ , a constant  $\Delta_\sigma = 0.0002$ ,  $U = 0.002$ ,

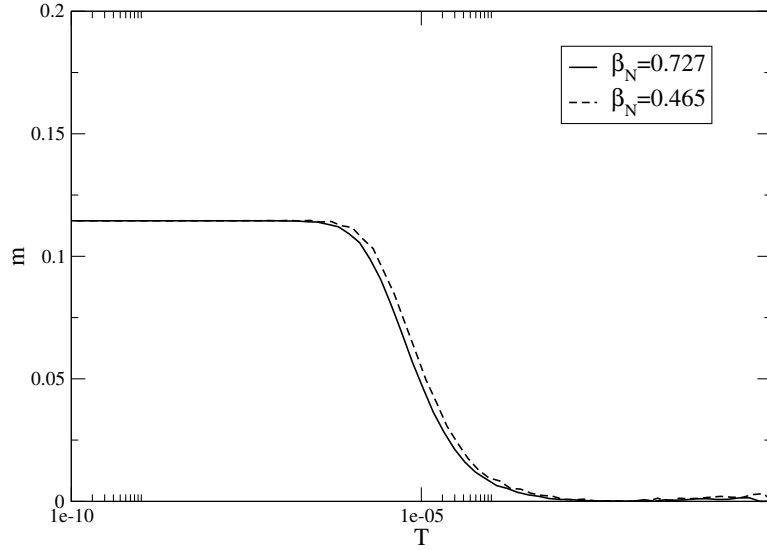


**Fig. 4.4:** Calculation of the impurity magnetization using different values of  $\beta_N$ .

$\epsilon_{f\uparrow} = 0.001001$  and  $\epsilon_{f\downarrow} = 0.000999$ . While there are some systematic differences in the value of the magnetization in the intermediate temperature regime, it is important to note that at low temperatures both curves lie on top of each other. This shows that the accuracy of the approach outlined above grows as the temperature becomes small. As most of the calculations in this work are done for the ground state, this is an important confirmation that the values obtained for the static properties from the NRG are indeed correct. For calculations at higher temperatures, one should keep in mind that at least the qualitative behavior of the system is correctly reproduced, while the precise values at a given temperature may differ by a few percent. This also implies that in the DMFT calculations the results at higher temperatures are qualitatively correct, but the exact values of e.g. transition temperatures can not be obtained. However, this is not the goal of the work presented here. The NRG itself has been designed to capture the arbitrarily small energy scales at very low temperatures and is therefore best suited to study the ground state. In the practical implementation, the case  $T = 0$  simply corresponds to choosing  $N$  large enough so that all additional couplings become negligibly small. This is usually the case for  $N$  between 60 and 100.

Additional confirmation of the results of the NRG method developed to study the magnetic properties of the single impurity model and, within the DMFT, of lattice models, can be obtained by a comparison with the exact results of Bethe ansatz calculations. The application of this method to the s-d model is discussed at length in the book by Hewson [Hew93]. Among other things, a calculation of the impurity moment as a function of an applied magnetic field  $H$  is presented for the ground state of the s-d model. As discussed in Section 2.2,

there is a parameter regime where the Anderson model can be mapped onto the s-d model by a Schrieffer-Wolff transformation. If a calculation of the impurity magnetization is performed in this regime of the Anderson model at  $T = 0$ , it can be compared to the results obtained by Hewson. This is shown in Figure 4.5. The parameters for the NRG calculation are  $\Delta_\sigma = 0.01$ ,  $U = 0.3$  and  $\epsilon_{f\sigma} = 0.15$ . In the calculation by Hewson the magnetic field has been scaled with the

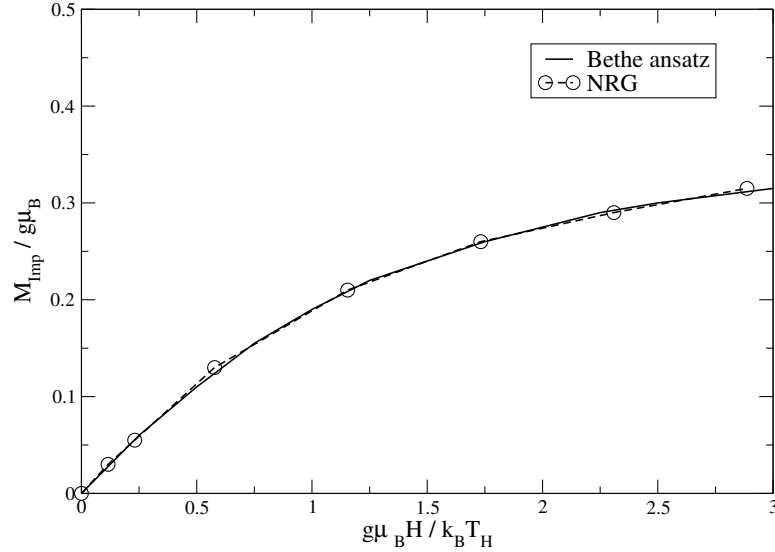


**Fig. 4.5:** Comparison of the impurity moment in a magnetic field with the Bethe ansatz result.

temperature  $T_H$ , which is proportional to the Kondo temperature  $T_K$ . While in the NRG calculations the Kondo temperature is not known a priori, it is enough to know that all thermodynamic quantities scale with this temperature. The NRG results are therefore simply scaled to fit to the Bethe ansatz calculation. The Kondo temperature  $T_K$  is of the order of  $10^{-7}$ . The fact that such a scaling is possible and both curves lie very close to each other for the whole range of magnetic fields  $H$  can be seen as confirmation of the NRG calculations. Both the almost linear behavior of the magnetization as  $H$  goes to zero and the slow approach to the saturation value of the magnetic moment can be reproduced. Only for temperatures much larger than the Kondo temperature the impurity spin is fully polarized.

It is also possible to calculate dynamical quantities such as the impurity spectral function using the formalism presented in this section. This is necessary to allow for the solution of the DMFT self-consistency equations. Again, this can also be done for finite temperatures, when only the chain corresponding to the temperature  $T_N$  has to be used for the calculation. However, only temperatures that are small compared to the bandwidth are accessible with the NRG. The details

of this approach, and the additional difficulties introduced by the broken spin symmetry, are described in the following section.

### 4.3 Calculation of dynamical quantities

The calculation of dynamical quantities using the NRG has first been realized by Frota and Olivera [Fro86] and also by Sakai et al. [Sak89]. In addition, transport properties like the resistivity, the thermal conductivity and the Hall-coefficient have been calculated [Hew93, Cos94]. In the following, the important steps necessary to obtain the spin-dependent impurity spectral function are explained in detail. It has turned out that performing this calculation as accurately as possible is essential if this approach is to be used to study the magnetic properties of lattice models in the framework of the DMFT.

#### Calculation of the spectral function

The impurity spectral function

$$A_{N\sigma}^f(\omega) = -\frac{1}{\pi} \Im m G_{N\sigma}^f(\omega) \quad (4.15)$$

at temperature  $T_N$ , or, more precisely, for a chain of length  $N$ , can be obtained from the equilibrium impurity Green's function

$$G_{N\sigma}^f(t) = -i\Theta(t) \text{Tr} \left\{ \hat{\rho}_N \left[ f_{-1\sigma}(t), f_{-1\sigma}^\dagger(0) \right] \right\} . \quad (4.16)$$

Laplace transformation of this expression and insertion into (4.15) lead to

$$A_{N\sigma}^f(\omega) = \frac{1}{2\pi} (C_{N\sigma}^>(\omega) + C_{N\sigma}^<(\omega)) , \quad (4.17)$$

where

$$C_{N\sigma}^>(\omega) = 2\pi \sum_{n_1, n_2, n} \rho_{n_1 n_2} \langle n_2 | f_{-1\sigma} | n \rangle \langle n | f_{-1\sigma}^\dagger | n_1 \rangle \delta(\omega - E_n + E_{n_2})$$

and

$$C_{N\sigma}^<(\omega) = 2\pi \sum_{n_1, n_2, n} \rho_{n_1 n_2} \langle n_2 | f_{-1\sigma}^\dagger | n \rangle \langle n | f_{-1\sigma} | n_1 \rangle \delta(\omega - E_{n_1} + E_n) .$$

The matrix elements of the  $f$  operators needed to evaluate (4.17) can be calculated during each step of the iterative procedure (see Appendix A). However, due to the truncation of the Hilbert space, each step  $N$  provides information only in a certain frequency range about  $T_N$ . Thus, in order to obtain the spectral function

at all relevant energy scales, one must collect the information from previous steps of the iterative diagonalization and combine it in a suitable way. The details of how to get a continuous function from the  $\delta$ -peaks in (4.17) are described at the end of this section.

An important shortcoming of this particular way to calculate dynamical quantities has first been pointed out by Hofstetter [Hof00]. If one evaluates (4.17) for some  $N' < N$ , one completely neglects the effects introduced by the degrees of freedom of the sites  $N' + 1 \dots N$  of the chain. In particular, in the case of a magnetic field applied to the impurity, the static magnetization calculated from the NRG (see Sec. 4.2) does not agree with the value obtained by integrating over the spectral functions for both spins up to the Fermi level and calculating the difference, at least not for small and intermediate fields. As most of the spectral weight is contained under the charge fluctuation peaks at high frequencies, they are obviously not reproduced correctly by using this method. Furthermore, the

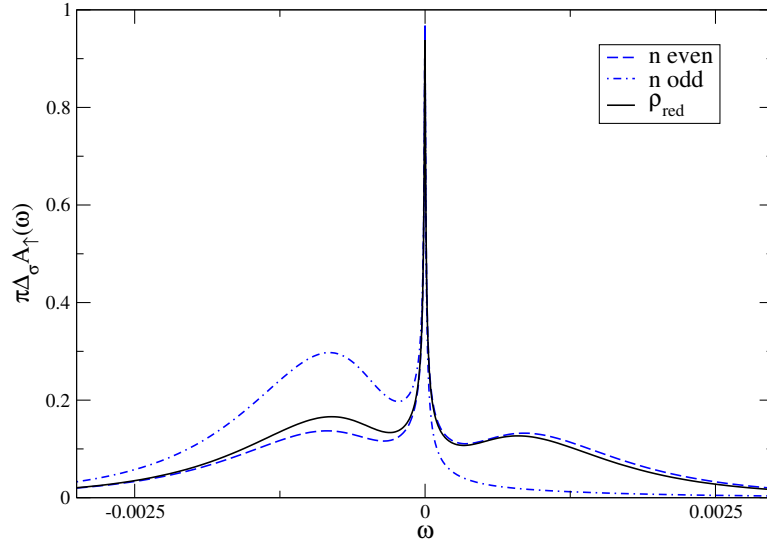


**Fig. 4.6:** Results for the impurity spectral function in a small magnetic field at  $T = 0$ . Both the curves calculated from even and odd iterations of the NRG differ significantly from the result obtained by using the reduced density matrix.

results show a strong dependence on whether the spectral function has been calculated from the even or the odd iterations of the NRG. This can be seen from Figure 4.6, where the two curves are compared to the correct result obtained with the method that will be introduced in the following. The parameters are the same as the ones used in the calculation of the static magnetization as a function of temperature in Sec. 4.2. Due to the symmetry of the spectra only those for spin up have been plotted. While not shown here, it is important to note that the value of the magnetization that can be extracted from the spectra obtained by

using the reduced density matrix (see below) is in excellent agreement with the static result at  $T = 0$ .

The key to understanding the discrepancy shown in Fig. 4.6 is the fact that the excitation spectrum for the chain changes between even and odd iterations due to the states having different quantum numbers  $Q$  and  $S_z$ . This has already been mentioned in the discussion of the energy levels of the chain in Fig. 4.3. It usually affects the results only slightly in the paramagnetic case, but it becomes crucial in the presence of an external magnetic field. The important difference is that once the spin symmetry has been broken, the states with  $S_z \neq 0$  are no longer degenerate. This may result in a situation where, for example, the ground state for even  $n$  has the quantum number  $S_z = 0$  and is therefore degenerate, whereas the ground state for odd  $n$  has the quantum number  $S_z = 1/2$  and is not degenerate. Of course this not only affects the ground state, but also the excited states. What is now used to describe the high-energy features of the full system, i.e. a chain of infinite length, are two short chains of finite length  $n$ , where  $n$  is either even or odd. For the reasons outlined above, the behavior of these two finite systems in a magnetic field may be qualitatively different, and neither one can capture the subtle effects a small field may have on the full system. This does not occur in the paramagnetic state, as the states will always be degenerate regardless of the value of  $S_z$ , and there is no additional small energy scale introduced by the magnetic field.

The situation becomes even more dramatic for the DMFT when applied to phases with broken symmetry. Here, no external field is present, but an internal molecular field is generated via the different effective media for spin up and spin down. Since within the DMFT all quantities have to be determined self-consistently, it is vital to get an accurate result for the one-particle dynamics obtained from the NRG. In fact, without using the formalism outlined in the following section, it has not been possible to obtain a stable magnetic solution for the Hubbard model at all.

From the previous discussion it is clear that the physics at low energy scales play an important role in determining dynamical properties at higher frequencies, at least in the case of symmetry-breaking. Therefore it is necessary to somehow connect the states of the chain at low temperatures to those of the finite system at higher temperatures. This is done by effectively projecting the states of the full system, i.e. the chain of length  $N$  corresponding to the temperature that one is interested in, onto the states of the shorter chain. In order to achieve this goal, one has to relate the density matrix at some step  $N' < N$  to the density matrix at step  $N$ , which actually describes the state of the system under investigation. Hofstetter suggested to calculate the reduced density matrix  $\hat{\rho}_{N'}^{red}$  that is obtained by tracing out the degrees of freedom of the remaining sites of the chain, and to use this matrix to evaluate (4.17) in step  $N'$ .

To make this procedure more transparent, let us divide the chain of length  $N$  as shown in Fig. 4.7 into a shorter chain of length  $N'$  and the remaining sites. One

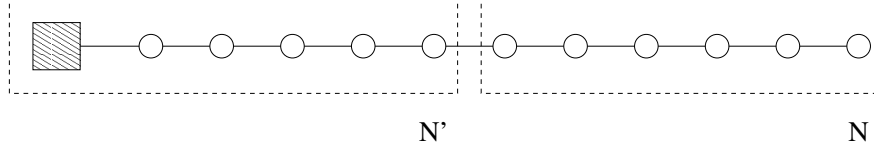


**Fig. 4.7:** *Division of the chain of length  $N$  into two subsystems.*

can then define a basis for the whole system by using the product basis of the two subsystems. Let the states  $|n'\rangle$  denote a basis for the shorter chain and the states  $|m\rangle$  a basis for the remaining part of the chain. In this product basis, the statistical operator  $\hat{\rho}_N$  may be written as

$$\hat{\rho}_N = \sum_{n'_1, n'_2, m_1, m_2} \rho_{m_1 n'_1 m_2 n'_2} |m_1\rangle |n'_1\rangle \langle n'_2| \langle m_2|. \quad (4.18)$$

Then, the reduced density matrix  $\hat{\rho}_{N'}^{red}$  can be obtained by successively tracing out the degrees of freedom of the remaining sites,

$$\hat{\rho}_{N'}^{red} = \text{Tr}_m(\hat{\rho}_N) = \sum_{n'_1, n'_2} \rho_{n'_1 n'_2}^{red} |n'_1\rangle \langle n'_2|, \quad (4.19)$$

with the matrix elements of  $\hat{\rho}_{N'}^{red}$  with respect to the basis of the shorter chain given by

$$\rho_{n'_1 n'_2}^{red} = \sum_m \rho_{m n'_1 m n'_2}. \quad (4.20)$$

This is the matrix that should be used to evaluate (4.17) in step  $N'$  of the diagonalization. Although it is no longer diagonal, it is still block diagonal with respect to the quantum numbers  $Q$  and  $S_z$ . This is important, because it allows for the projection of the reduced density matrix  $\hat{\rho}_{N'}^{red}$  onto  $\hat{\rho}_{N'-1}^{red}$  to be carried out separately for each subspace  $(Q, S_z)$ .

The procedure then works as follows. First, one has to complete the NRG up to a desired step  $N$ . Second, starting from this step  $N$ , one has to transform the density matrix back onto the chain with  $N' < N$  sites. How the latter is done in practice will be illustrated for the first step of this projection.

The starting point is the statistical operator (4.14) for the chain with  $N$  sites. In the basis in which  $H_N$  is diagonal, the matrix associated with this operator is also diagonal. Now, a unitary transformation is carried out onto the product basis of  $H_N$ , which has the form (4.13) with  $N$  replaced by  $N - 1$ . The transformation matrix is built from the eigenvectors obtained by the previous diagonalization of

$H_N$  in each subspace. In this representation, the matrix of the operator  $\hat{\rho}_N$  is of course no longer diagonal. In order to obtain the reduced density matrix for the chain of length  $N - 1$ , one needs to trace out the degrees of freedom of the  $N$ th site. From (4.13) it is clear that these can be represented by the four states  $|0\rangle$ ,  $|1\rangle = f_{N\uparrow}^\dagger|0\rangle$ ,  $|2\rangle = f_{N\downarrow}^\dagger|0\rangle$  and  $|3\rangle = f_{N\uparrow}^\dagger f_{N\downarrow}^\dagger|0\rangle$ . Therefore, the matrix elements of the reduced density matrix are

$$\rho_{n'_1 n'_2}^{red} = \sum_{i=0}^3 \langle i | \hat{\rho}_N | i \rangle, \quad (4.21)$$

where now  $N' = N - 1$ .

Again, this can be done for each  $(Q, S_z)$  subspace of  $H_{N-1}$  separately. In practice, one has to identify those subspaces of  $H_N$  which are linked to the subspace  $(Q, S_z)$  of  $H_{N-1}$  through the definitions (4.13). The matrix of  $\hat{\rho}_N$  for each of these four subspaces in the product basis of  $H_N$  is made up of four blocks corresponding to four different subspaces of  $H_{N-1}$ . All that is left to do is to identify the block corresponding to the desired  $(Q, S_z)$  subspace of  $H_{N-1}$  for each of these four matrices and perform the partial trace. One thus obtains four contributions to  $\hat{\rho}_{N-1}^{red}$ , which, when added up, produce the final reduced density matrix  $\rho_{N-1}^{red}$  for a given subspace  $(Q, S_z)$  of  $H_{N-1}$ . These matrices then serve as the starting point for the next step of the projection. In doing this projection all the way back, it is possible to obtain the correct spectral density for all the different energy scales represented by the chains of different length  $N'$ .

In the actual calculation one therefore does not compute the spectral function in each step of the iterative diagonalization, but one first carries out the diagonalization until the end, keeping all the unitary matrices from each step. Then, using these matrices, the reduced density matrix is calculated for each chain of different length  $N'$ . Finally, once all these matrices are known, the spectral function is calculated using eq. (4.17).

It is clear from (4.17) that the resulting spectral function is made up of a set of discrete peaks. To get a continuous function  $A_\sigma(\omega)$ , these peaks have to be broadened, using a Gaussian broadening on a logarithmic scale with a width  $b$ ,

$$\delta(\omega - \omega_n) \rightarrow \frac{e^{-b^2/4}}{b\omega_n\sqrt{\pi}} \exp\left(-\frac{(\ln \omega - \ln \omega_n)^2}{b^2}\right). \quad (4.22)$$

This is done with respect to the exponentially decreasing energy scales of the series of Hamiltonians  $H_N$ . In practice the parameter  $b$  is chosen between 0.3 and 0.6. For the calculations presented in this work the value  $b = 0.6$  has been used.

Once the spectral function is known, it is possible to calculate the single-particle Green's function  $G_\sigma^f(z)$  [Sak89, Cos94]. There are, however, difficulties in the calculation of the self-energy  $\Sigma_\sigma(z)$  from this Green's function. The reason for this is

the inaccuracy in the calculation of the spectral function, namely the combination of the spectral information from all the different steps of the NRG calculation and the additional broadening. Especially for the DMFT calculations, it is crucial that the self-energy is calculated as accurately as possible. Therefore, an alternative way of calculating the self-energy of the impurity has been developed [Bul98], which will be introduced in the following section.

### Calculation of the self-energy

The starting point for the calculation of the self-energy is the Hamiltonian of the single-impurity model (4.3). From the equation of motion

$$z \langle\langle A, B \rangle\rangle_z + \langle\langle [H, A], B \rangle\rangle_z = \langle[A, B]_+\rangle, \quad (4.23)$$

where  $A$  and  $B$  are fermionic operators, the following result is obtained for the impurity Green's function  $G_\sigma^f(z) = \langle\langle f_{-1\sigma}, f_{-1\sigma}^\dagger \rangle\rangle_z$ ,

$$(z - \epsilon_{f\sigma}) G_\sigma^f(z) - U F_\sigma(z) - \sum_{k\sigma} V_{k\sigma} \langle\langle c_{k\sigma}, f_{-1\sigma}^\dagger \rangle\rangle_z = 1. \quad (4.24)$$

The correlation function  $F_\sigma(z)$  is defined by  $F_\sigma(z) = \langle\langle f_{-1\sigma} f_{-1\bar{\sigma}}^\dagger f_{-1\bar{\sigma}}, f_{-1\sigma}^\dagger \rangle\rangle_z$ .

Using the relation (4.23) it can also be shown that

$$(z - \epsilon_{k\sigma}) \langle\langle c_{k\sigma}, f_{-1\sigma}^\dagger \rangle\rangle_z - V_{k\sigma} G_\sigma^f(z) = 0. \quad (4.25)$$

Combining equations (4.25) and (4.24), the impurity Green's function can be written as

$$G_\sigma^f(z) = \frac{1}{z - \epsilon_{f\sigma} - \Sigma_\sigma(z) - \Delta_\sigma(z)} \quad (4.26)$$

with

$$\Sigma_\sigma(z) = U \frac{F_\sigma(z)}{G_\sigma^f(z)} \quad \text{and} \quad \Delta_\sigma(z) = \sum_{k\sigma} V_{k\sigma}^2 \frac{1}{z - \epsilon_{k\sigma}}. \quad (4.27)$$

In this formalism, the self-energy  $\Sigma_\sigma(z)$  is calculated by dividing one correlation function by another. The function  $F_\sigma(z)$  can be calculated from the NRG in a similar way as the Green's function. The additional matrix elements in the spectral representation of  $F_\sigma(z)$  needed for this calculation are given in the appendix.

The important improvement is that both quantities used to obtain the self-energy are now affected by the same systematic errors due to the combination of spectral information from the various steps and the broadening of the  $\delta$ -peaks. It has been shown that the calculation of the self-energy in such a way is much more accurate than a direct extraction of this quantity using the relation

$$\Sigma_\sigma(z) = G_{0\sigma}^f(z)^{-1} - G_\sigma^f(z)^{-1}, \quad G_{0\sigma}^f(z) = \frac{1}{z - \epsilon_{f\sigma} - \Delta_\sigma(z)}, \quad (4.28)$$

from the impurity Green's function alone [Bul98]. Therefore, it is the method outlined above that is used for all the DMFT calculations presented in this work.

It should be mentioned that this method also allows for a more accurate calculation of the spectral function for the impurity problem. Using the self-energy obtained from (4.27), it is possible to calculate the Green's function (4.26), as the hybridization function  $\Delta_\sigma(z)$  is usually known. At least for a constant  $\Delta_\sigma$  this can easily be implemented. Fig. 4.8 shows some results for the symmetric

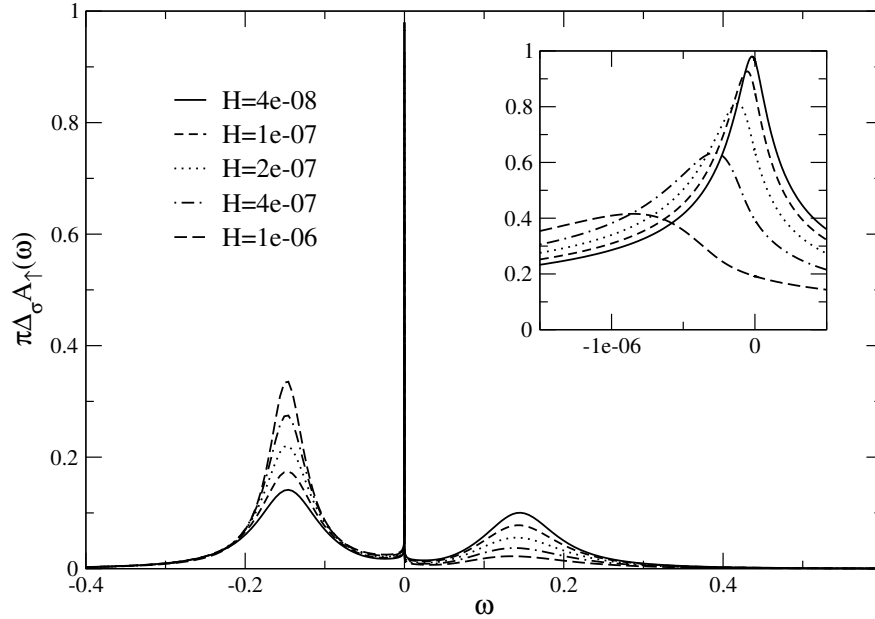


**Fig. 4.8:** Spectral function for the symmetric Anderson model at  $T = 0$  in the presence of a magnetic field, with parameters  $\Delta_\sigma = 0.01$ ,  $U = 0.3$  and  $\epsilon_{f\sigma} = 0.15$ .

Anderson model in a magnetic field at  $T = 0$  for the parameters  $\Delta_\sigma = 0.01$ ,  $U = 0.3$  and  $\epsilon_{f\sigma} = 0.15$ . The parameters for the NRG are  $\Lambda = 2$  and  $b = 0.6$ , and 1600 states have been kept in each step of the calculation. Again, due to particle-hole symmetry only the spectral function for spin up is shown.

There are two main effects due to the applied magnetic field. One is obviously the redistribution of spectral weight from the charge fluctuation peak above the Fermi energy to the one below it. This corresponds to a difference in the occupation number of the impurity site and a magnetization  $m = n_\uparrow - n_\downarrow$ . The behavior of the magnetization as a function of magnetic field  $H$  has already been discussed in Sec. 4.2. The value of the magnetization that can be extracted from the spectra shown above is in excellent agreement with the static results regardless of the size of  $H$ .

The second effect is the shift of the resonance at the Fermi level. For the majority

spin shown here it is shifted below the Fermi energy. In addition, the height of the resonance decreases as  $H$  increases. It turns out that the relevant energy scale for the suppression of the resonance is the Kondo temperature  $T_K$ . As long as  $H < T_K$ , the height of the peak does not deviate significantly from its zero-field value of 1. As soon as  $H$  is of the order of the Kondo temperature, the height of the resonance decreases and it is shifted further away from the Fermi level. For the parameters used in this calculation  $T_K$  is of the order of  $10^{-7}$ , and this behavior can be seen very nicely from Fig. 4.8. In the presence of a strong magnetic field the Kondo effect is suppressed, a screening of the impurity spin at very low temperature is no longer possible. This is also reflected in the flow of the energy levels shown in Fig. 4.3, where the different fixed points for both small and large fields have been discussed. The fact that the local Fermi liquid behavior is destroyed can also be seen from the self-energy, as it starts to deviate from the typical quadratic dependence on  $\omega$  at low frequencies when a magnetic field is applied.

The accurate calculation of the self-energy described above, combined with the extension of the NRG to include the spin degree of freedom, now allows for the NRG to be used as a reliable impurity solver in the DMFT investigations of the symmetry-broken phases of the Hubbard model. The results obtained from the combination of these two methods will be presented in the following chapter.



## 5. RESULTS

In this chapter results for the one-band Hubbard model both at half filling and with finite doping are presented. They have been obtained within the framework of the dynamical mean-field theory that has been introduced in Chapter 3. The effective single impurity Anderson model has been solved using Wilson's numerical renormalization group theory, suitably extended to allow for the treatment of spin-dependent problems and the calculation of dynamical quantities. Using this method, which has been discussed in Chapter 4, it is possible to obtain reliable results for the Hubbard model at low temperatures and at  $T = 0$ . The focus of the work presented here is the investigation of the magnetic properties of this model. To that end, the single-particle spectral function in the symmetry-broken phases is calculated, and from that additional quantities like the optical conductivity are accessible. In addition, the magnetization and the double occupancy can be calculated from the NRG directly. Thus, a comprehensive description of the magnetic phases of this important model can be obtained within the DMFT.

### 5.1 The Hubbard model at half filling

The half-filled one-band Hubbard model is frequently used to explain the properties of real materials such as various transition metal oxides, in particular the paramagnetic metal-insulator transition and the antiferromagnetic phase at low temperatures. In studying the paramagnetic MIT the antiferromagnetic phase is usually suppressed, and a brief review of the results obtained for this scenario is presented in Sec. 5.1.1. The antiferromagnetic ground state, in particular the question whether a similar transition can be found in this phase, is discussed in detail in Sec. 5.1.2. To that end, the optical conductivity in the Néel state is calculated within the DMFT. In order to describe the phase diagram of real materials like  $V_2O_3$ , the Hubbard model in the presence of frustration is investigated in Sec. 5.1.3.

#### 5.1.1 The paramagnetic metal-insulator transition

The paramagnetic metal-insulator transition in the half-filled Hubbard model has been studied extensively within the dynamical mean-field theory. Note that

in order to observe this transition, it is necessary to artificially suppress the antiferromagnetic state that otherwise dominates the physics at half filling. This can easily be done in the numerical calculations by simply not allowing for a symmetry-broken solution. It is motivated by the presence of a paramagnetic metal-insulator transition in real materials such as  $V_2O_3$  (see Fig. 2.1). In doing so, a transition from a paramagnetic metal to a paramagnetic insulator can be found at half filling. At  $T = 0$  it occurs at a value of the Coulomb parameter  $U_c \approx 1.5W$  [Jar93, Geo96, Bul99]. Interestingly, the transition is of first order [Geo96, Bul01] for  $T > 0$  with a second order end point at a  $T_c \approx 0.017W$  and  $U_c \approx 1.2W$ . At higher temperatures a crossover from the metallic to the insulating region is found. This has been summarized in the phase diagram shown

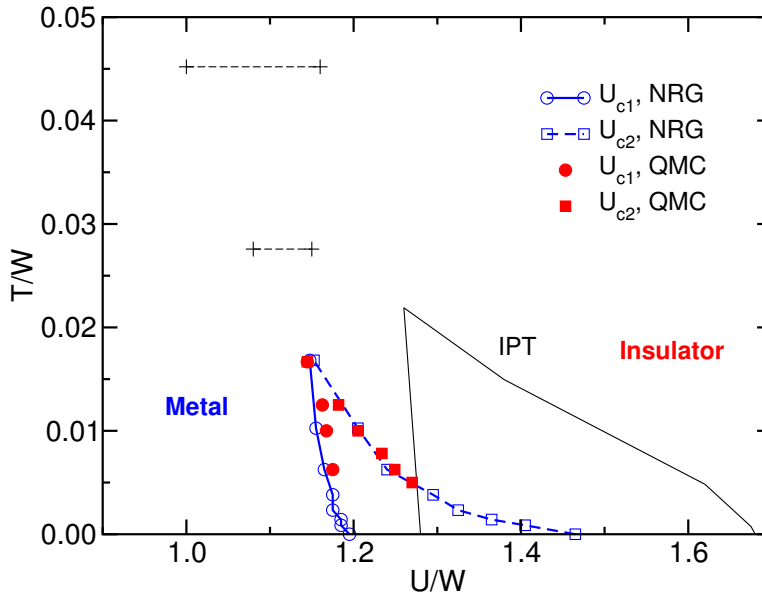


**Fig. 5.1:** DMFT phase diagram for the paramagnetic metal-insulator transition in the one-band Hubbard model.

in Figure 5.1. A closer look at the phase diagram of  $V_2O_3$  (see Fig. 2.1) reveals a strikingly similar scenario, and indeed the DMFT results for the Hubbard model have frequently been used as a qualitative explanation [Roz95, Geo96].

The NRG has played a very important role in establishing this picture of the Mott transition in the Hubbard model. Previously there had been some disagreement with regard to the first order transition and the possibility of the coexistence of an insulating and a metallic region. This scenario had first been proposed by Georges et al. [Geo96] using the iterated perturbation theory (IPT) and exact diagonalization. The NRG has been able to confirm this both at  $T = 0$  [Bul99] and at finite temperatures [Bul01]. In the meantime, quantum Monte Carlo calculations have further validated these results [Roz99, Blu02]. Furthermore,

the features described above are independent of the underlying lattice structure. While the data shown in Figure 5.1 have been obtained for the Bethe lattice (which will be introduced later in this chapter), the results for the hypercubic lattice are qualitatively the same, with the critical interaction  $U$  also of the order of the bandwidth  $W$ . Figure 5.2 shows the spectral function

$$A(\omega) = -\frac{1}{\pi} \Im m G_{ii}(\omega) \quad (5.1)$$

for the hypercubic lattice for different values of the interaction strength  $U$ . The calculations have been done using the NRG at  $T = 0$ . As in most of the calculations presented in this chapter, the parameter  $\Lambda = 2$  has been used, and 800 states have been kept in each step of the calculation. The unit of energy is

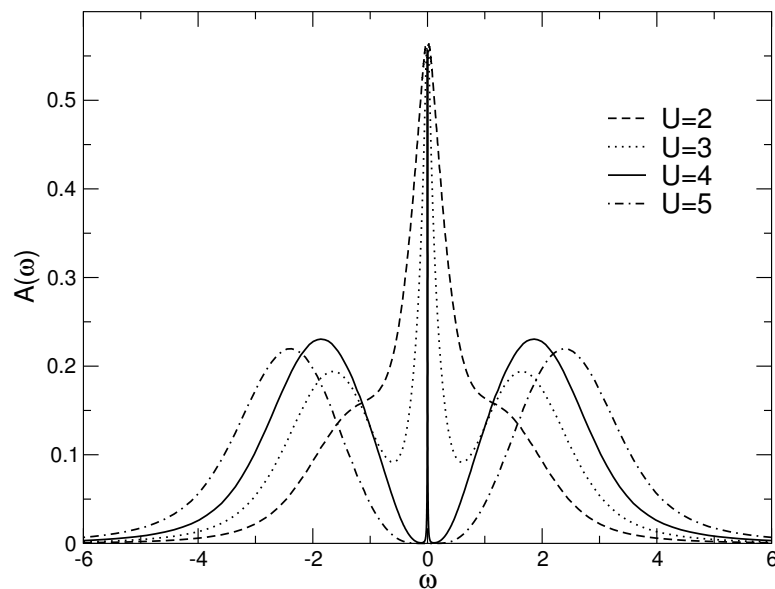


**Fig. 5.2:** Spectral functions for the Hubbard model on a hypercubic lattice for different values of the Coulomb interaction  $U$ . With increasing  $U$  the quasiparticle peak narrows until it vanishes at a critical  $U_{c2} \approx 4$ .

again the rescaled hopping matrix element  $t^*$  defined by equation (3.5). As the Gaussian density of states in the limit of  $d \rightarrow \infty$  has no real band edges, a value of  $W = 4t^*$  is taken to be a reasonable approximation for the hypercubic lattice. Not only is the spectral weight of the Gaussian exhausted by 99% between  $\omega = -W/2$  and  $\omega = W/2$ , but the metal-insulator transition then occurs at a value  $U_{c2} \approx W$  [Jar93].

As the transition is approached from the metallic side, a typical three-peak structure appears in the spectral function, namely the two Hubbard bands at  $\omega \approx \pm U/2$  and a quasiparticle peak at  $\omega = 0$ . The width of this peak decreases

as  $U$  increases, until it vanishes as  $U \rightarrow U_{c2}$ . As a result, only the two Hubbard bands remain, with the Fermi energy lying between them. Although, due to the broadening involved in the calculation of the self-energy, the spectral weight at the Fermi energy is never exactly zero, the results indicate that the gap opens discontinuously. Approaching the transition from the insulating side and decreasing  $U$ , the transition to a metallic state occurs at a lower critical value  $U_{c1}$ . In the practical implementation this is done by initializing the DMFT calculation with an insulating solution and slowly decreasing  $U$ . This results in the hysteresis region depicted in the phase diagram in Fig. 5.1. The actual first order transition lies between the two phase boundaries, and it can only be determined by calculating the free energy. This is currently not possible using the NRG, but it has been done for the QMC calculations at higher temperatures [Blu02].

From what has been discussed in the previous section it is clear that the NRG is a very powerful method to investigate the paramagnetic metal-insulator transition in the Hubbard model using the DMFT. Not only is it non-perturbative, but the fact that it is designed to capture arbitrarily small energy scales make it the ideal method to describe the vanishing of the quasiparticle peak. It should be noted that the high-energy features of the spectral function, i.e. the precise shape of the Hubbard peaks, can not be obtained from the NRG due to the intrinsic broadening on a logarithmic scale. However, more importantly, the spectral weight under these peaks is always obtained very accurately. Furthermore, the NRG allows for an accurate calculation of dynamical quantities at very low temperatures, and, by design, works best at  $T = 0$ . While until recently the NRG could only be applied to the studies of the paramagnetic state, the extension of the method to describe symmetry-broken phases now allows for the investigation of the antiferromagnetic ground state of the Hubbard model within the framework of the DMFT. This will be discussed in the following section.

### 5.1.2 The antiferromagnetic state

The tendency to order antiferromagnetically has already been discussed in Section 2.1, when the Hubbard model was first introduced. Now, numerical calculations are performed to take a closer look at the antiferromagnetic ground state at half filling. This is interesting for several reasons. First, as has been mentioned already, the insulating phase in real materials like  $V_2O_3$  is in many cases accompanied by antiferromagnetic ordering, which is typically of the Néel type. One interesting and controversial question concerns the description of the optical properties of these materials [Tho94]. It is not clear whether the underlying physics are governed by the broken translational symmetry in the antiferromagnetic state or rather by the electronic correlations, i.e. the opening of a gap due to the formation of an upper and a lower Hubbard band. To what extent the

model (2.1) can describe the optical properties of ordered insulating phases has up to now not been studied in detail. To that end, a formalism to calculate the optical conductivity within the DMFT has been developed in Sec. 3.3, and the results will be discussed below. Second, as has been shown in the previous section, the restriction of the Hubbard model to the paramagnetic state shows a metal-insulator transition at a finite critical  $U_c > 0$ , which has been shown to be of first order. It might be argued that for the Néel state a similar situation can occur. At small  $U$ , a weak coupling theory is expected to give accurate results, leading to a band or Slater insulator [Sla51] due to the doubled unit cell in the Néel state. At large  $U$ , on the other hand, the Hubbard model is known to reduce to an effective Heisenberg model (see Sec. 2.1), with localized moments from the onset. It is an open question whether these two limits are linked continuously or via a phase transition at some finite value of the Coulomb interaction  $U$ .

The results which are presented in the following have been obtained for a hypercubic lattice with nearest neighbor hopping at half filling and  $T = 0$ . The hopping matrix element is again chosen as  $t = t^*/\sqrt{4d}$ , which ensures the correct scaling of the kinetic energy in the limit  $d \rightarrow \infty$ . The unit of energy is the bandwidth  $W$  of the non-interacting system. As discussed in the previous section,  $W = 4t^*$  seems a reasonable definition. The effective quantum impurity model of the DMFT is solved using the NRG method (see chapter 4), extended to allow for an accurate calculation of dynamical quantities in the magnetic state. The calculations have been performed using a discretization parameter  $\Lambda = 2$  and keeping 800 states in each step of the NRG calculation. Dynamical quantities have been calculated with the parameter  $b = 0.6$  for the logarithmic broadening of the  $\delta$ -peaks. Occasional checks using 1600 states or a smaller  $\Lambda$  have been performed and showed a sufficient robustness of the results.

### Single-particle properties

Before discussing the optical conductivity calculated from (3.18), it is helpful to review the single particle properties. The spin resolved one-particle density of states (DOS) calculated at  $T = 0$  for different values of  $U$  shows the expected insulating behavior with a clear gap at the Fermi energy for all values of  $U > 0$  (see Fig. 5.3). In particular for small values  $U \ll W$ , the DOS shows nicely developed nesting singularities at the gap edges, which qualitatively follow the predictions of a weak coupling theory. This will be discussed in more detail in Section 5.2.1. With increasing  $U$ , the features get more and more smeared out, and for  $U \gtrsim W$  the spectra resemble those of the Mott insulator [Pru95]. Note that the appearance of a gap in the DOS is of course accompanied by a vanishing imaginary part of the one-particle self-energy in this region. Neither the development of the DOS nor the magnetization as a function of  $U$  shown in the inset to Fig. 5.3 provide any evidence as to whether the limits  $U \ll W$

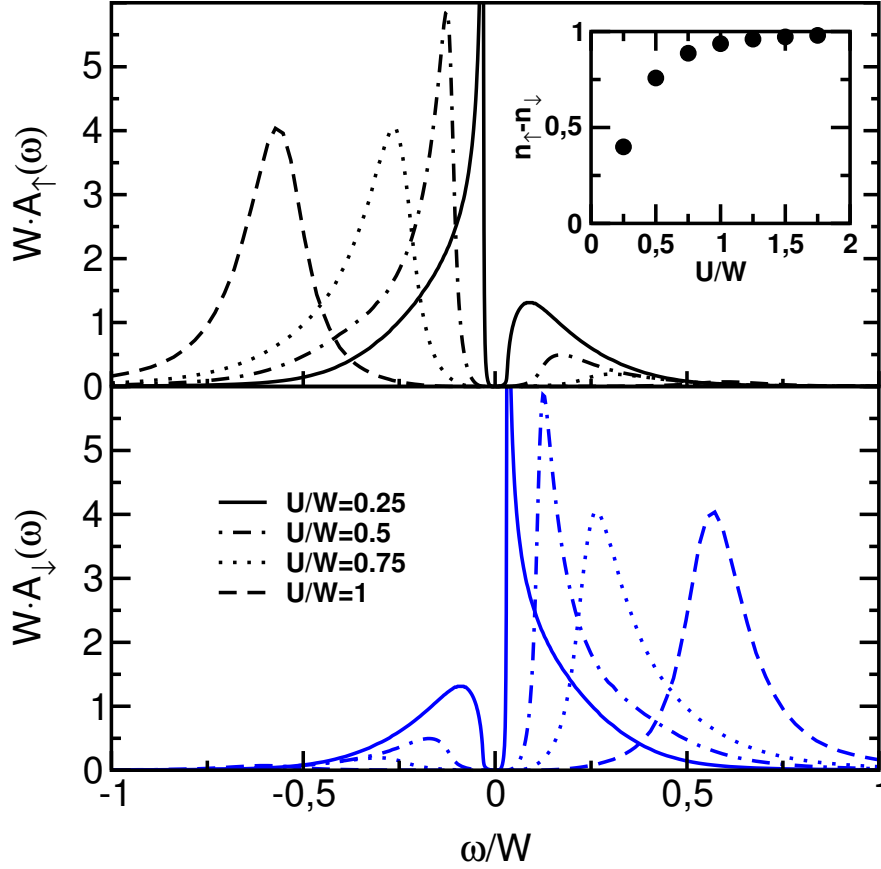


**Fig. 5.3:** *Spin-resolved density of states for the antiferromagnetically ordered phase of the half-filled Hubbard model for different values of  $U/W$ . The inset shows the magnetization as a function of  $U/W$ .*

and  $U \gtrsim W$  are linked smoothly or by some kind of transition. To gain further insight into this open question, it is necessary to obtain additional information about the nature of the antiferromagnetic state.

### Spin dynamics

A quantity of interest is the dynamical magnetic susceptibility, whose low-energy behavior may give insight into possible differences in the spin and charge dynamics of the system. In principle, it is also possible to calculate this quantity as a function of the wave vector  $\mathbf{q}$  within the DMFT [Jar93, Geo96]. However, this requires the calculation of the local irreducible particle-hole self-energy [Bra91], which is presently not possible within the NRG. Nevertheless, for the current investigation, a reasonable approximation can be obtained from the local magnetic

susceptibility

$$\chi_{\perp}(z) = \frac{1}{N} \sum_{\mathbf{q}} \chi_{\perp}(\mathbf{q}, z) .$$

Since the ground state of the system is the Néel state, spin excitations require a minimum excitation energy, the spin gap  $\Delta_s$ , which conventionally is obtained by evaluating  $\Im m \chi_{\perp}(\mathbf{Q}, \omega + i\delta)$  at the antiferromagnetic wave vector  $\mathbf{Q} = (\pi, \pi, \dots)$ . However, the gaps at other  $\mathbf{q}$  vectors will be equal to or larger than  $\Delta_s$ . Thus, even after summing over all  $\mathbf{q}$ -values, the size of the gap in  $\Im m \chi_{\perp}(\omega + i\delta)$  will be determined by  $\Delta_s$ . The quantity  $\Im m \chi_{\perp}(\omega + i\delta)$  on the other hand can easily be calculated from the NRG once the DMFT has converged. This calculation has been performed by Thomas Pruschke. The results for three typical values of  $U/W$  are shown in Fig. 5.4, displaying a nice spin gap  $\Delta_s$  as  $\omega \rightarrow 0$ . Evidently,

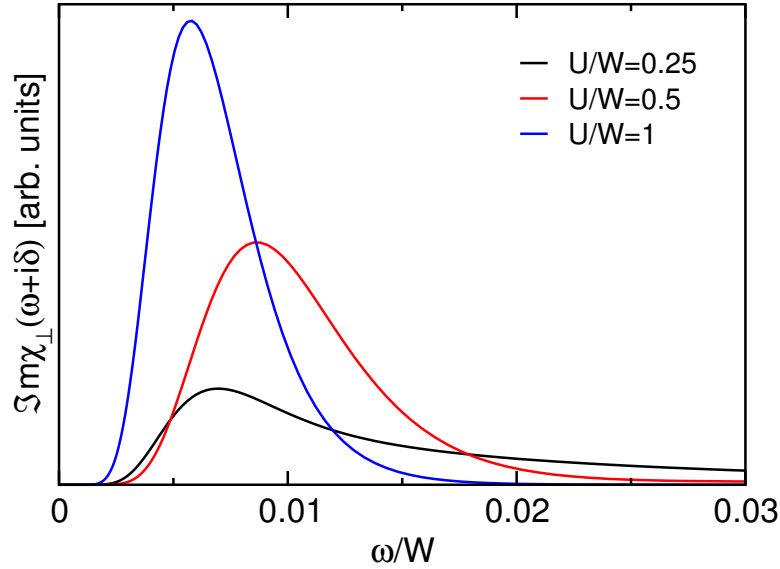


**Fig. 5.4:** *Imaginary part of the local transverse magnetic susceptibility as a function of  $\omega/W$  for  $U/W = 0.25, 0.5$  and  $1$ , which shows a well-defined gap  $\Delta_s$  as  $\omega \rightarrow 0$ . Only the part for  $\omega > 0$  is shown. Note that  $\Delta_s$  first increases with increasing  $U$ , but eventually decreases again.*

the value of  $\Delta_s$  first increases with increasing  $U$  before it decreases again, as is to be expected from the mapping of the Hubbard model onto an antiferromagnetic Heisenberg model at large  $U$ . From the calculated  $\Im m \chi_{\perp}(\omega + i\delta)$  one can extract the values for  $\Delta_s(U)$  by fitting the data to  $\Im m \chi_{\perp}(\omega + i\delta) \propto e^{-\Delta_s/\omega}$  as  $\omega \rightarrow 0$ . The results will be discussed below together with the results for the charge gap obtained from the optical conductivity (see Fig. 5.7).

### Optical conductivity and optical gap

The optical conductivity, calculated from the spectra in Fig. 5.3, is shown in Figure 5.5. Apparently, the overall behavior seen in the DOS is reflected in

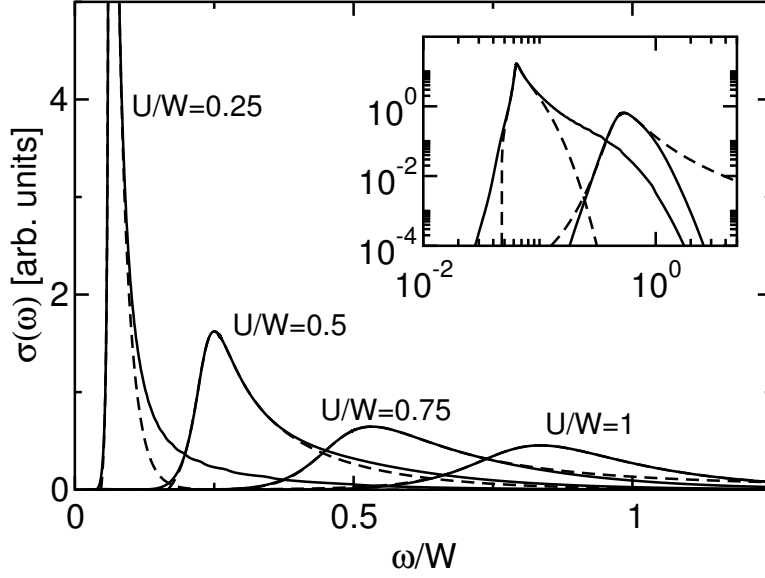


**Fig. 5.5:** *Optical conductivity of the half-filled Hubbard model in the Néel state at  $T = 0$  as a function of  $U$ . The full lines represent the calculated data, the dashed lines a fit with the function  $\omega \cdot \sigma(\omega) = \Im m \{ e^{i\phi} (\omega - \omega_0 + i\gamma)^{-\alpha} \}$ . The inset shows the curves for  $U/W = 0.25$  and  $U/W = 0.75$  using a logarithmic scaling.*

the results for  $\sigma(\omega)$ . For small values of  $U$  one finds a threshold behavior with a singularity, whereas for large  $U$  the optical conductivity closely resembles the one found in the paramagnetic insulator [Jar93]. There are two interesting features that can be identified in the result for  $\sigma(\omega)$ , namely the behavior of  $\sigma(\omega)$  in the vicinity of the maximum and the actual value of the optical gap, i.e. the energy at which  $\sigma(\omega) = 0$ .

In order to address the first point, one can proceed as follows. In the Hartree limit, i.e. without an imaginary part of the self-energy, an approximate evaluation of (3.18) yields

$$\omega \cdot \sigma(\omega) \propto \frac{\Theta(\omega - 2\Delta_0)}{\sqrt{\omega - 2\Delta_0}}$$

with  $\Delta_0 = Um_s/2$  and  $m_s = \langle n_\uparrow - n_\downarrow \rangle$ . Since this behavior is governed by the square-root singularities in the integrand in (3.18) (see e.g. the explicit formula derived in the appendix), it is reasonable to assume that for a finite imaginary

part of the self-energy the above singularity will become an algebraic function,

$$\omega \cdot \sigma(\omega) \propto \Im m \left\{ \frac{e^{i\phi}}{(\omega - \omega_0 + i\gamma)^\alpha} \right\}, \quad (5.2)$$

with a general exponent  $\alpha$ . The quantity  $\gamma$  approximately takes into account the finite imaginary part introduced by the one-particle self-energy, and  $\phi$  allows for a more complex mixing of real and imaginary parts in the integral (3.18). The function (5.2) describes the behavior of  $\sigma(\omega)$  in the vicinity of the maximum very well for all values of  $U/W$  (see dashed lines in Fig. 5.5); note that from the inset it is evident that for small  $U$  this algebraic form has the tendency to overestimate the optical gap, while at large  $U$  it is clearly underestimated.

The behavior of the fit parameters  $\omega_0$ ,  $\alpha$  and  $\phi$  as a function of  $U/W$  is shown in Fig. 5.6. As  $U \rightarrow 0$ , it is expected that  $\omega_0 = 2\Delta_0 = Um_s$ ,  $\alpha = 1/2$  and  $\phi = \pi/2$ , i.e.  $\omega \cdot \sigma(\omega) \propto \Re e (\omega - \omega_0 + i\delta)^{-1/2} = \Theta(\omega - \omega_0)/\sqrt{\omega - \omega_0}$ . This square-root singularity is indeed reproduced; however, even for small values of  $U/W$ , the

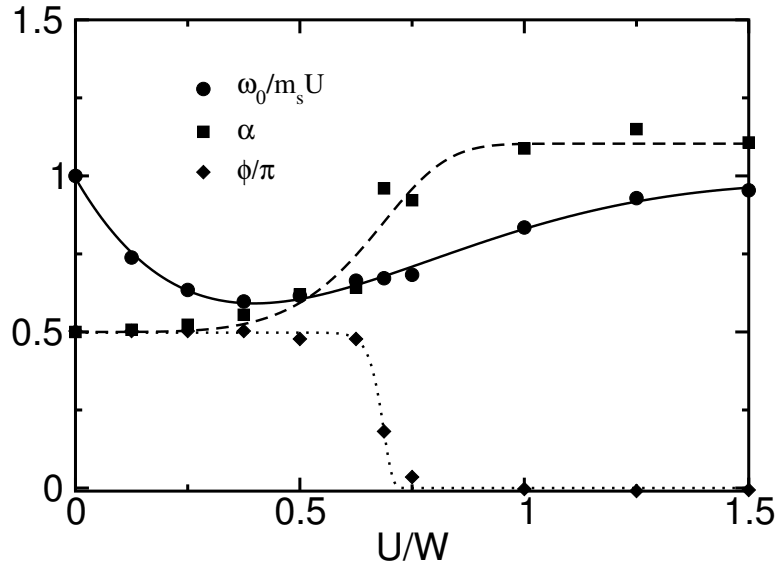


**Fig. 5.6:** Dependence of the fit parameters  $\omega_0$ ,  $\alpha$  and  $\phi$  in (5.2) on  $U$ . The lines are meant as guides to the eye. Note the rather well defined change in  $(\alpha, \phi)$  from  $(\alpha, \phi) = (1/2, \pi/2)$  to  $(\alpha, \phi) = (1, 0)$  around  $U/W = 0.75$ .

value of  $\omega_0$  significantly deviates from the Hartree value, being systematically smaller but obviously approaching it as  $U \rightarrow 0$ . This indicates that correlation effects have to be taken into account even for small values of  $U$ .

For values  $U > W$ , the behavior of  $\omega \cdot \sigma(\omega)$  is best described by a Lorentian, which becomes apparent from the values of  $\alpha$  and  $\phi$  obtained in this region, i.e.

$\alpha \approx 1$  and  $\phi = 0$ . This leads to the expression  $\omega \cdot \sigma(\omega) \propto \Im m(\omega - \omega_0 + i\gamma)^{-1} \propto 1/((\omega - \omega_0)^2 + \gamma^2)$ . In addition, the results for  $\omega_0$  together with  $m_s \approx 1$  indicate that  $\omega_0 \approx U$ , in agreement with the predictions of the Mott-Hubbard picture [Geo96].

The optical gap  $\Delta_c$  is displayed in Figure 5.7, together with the spin gap  $\Delta_s$  and the double occupancy  $\langle n_\uparrow n_\downarrow \rangle$ . While the definition of the optical gap is straight-

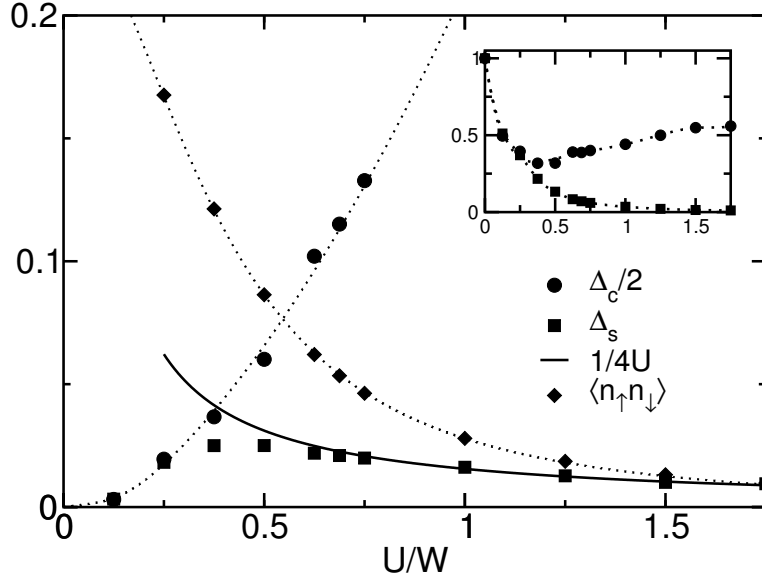


**Fig. 5.7:** Optical gap  $\Delta_c/2$  (circles), spin gap  $\Delta_s$  (squares) and double occupancy (diamonds) as a function of  $U$ . The inset shows the gaps scaled with  $Um_s/2$ . Dotted lines are meant as guides to the eye. For small  $U$  both charge and spin gap are identical, while for large  $U$  they behave like  $\Delta_c \propto U$  (see inset) and  $\Delta_s \propto 1/U$  (full line in main panel).

forward, the extraction of numbers from the numerical data is rather difficult. This is due to the following reasons. First, it is well known that the spectra calculated from the NRG contain an intrinsic broadening, which becomes especially severe for the Hubbard bands at larger values of  $U/W$  due to the logarithmic discretization of the conduction band. Second, as  $\omega \ll \omega_0$ , the imaginary part of the one-particle self-energy becomes negligible, and the singular structure of the integrands (B.1) – (B.4) that enter into the calculation of the optical conductivity from equation (3.18) require an additional broadening to allow for a stable numerical integration. Both of these effects taken together very efficiently mask the true  $\omega$ -dependence close to the optical gap, in particular for larger values of  $U/W$ . In order to nevertheless have an unambiguous working procedure that allows to extract a reasonable approximation to the true optical gap from the numerical data, it is *postulated* that  $\omega \cdot \sigma(\omega) \propto \Theta(\omega - 2\Delta_0) \cdot (\omega - 2\Delta_0)^\alpha$  in the region where

the fit with the function (5.2) starts to deviate substantially from the data, and a minimal  $\alpha$  is *chosen* such that a reasonable fit can be obtained *for all values of*  $U/W$  (see Fig. 5.8 for selected results). Doing so results in a value  $\alpha = 5/2$  (the

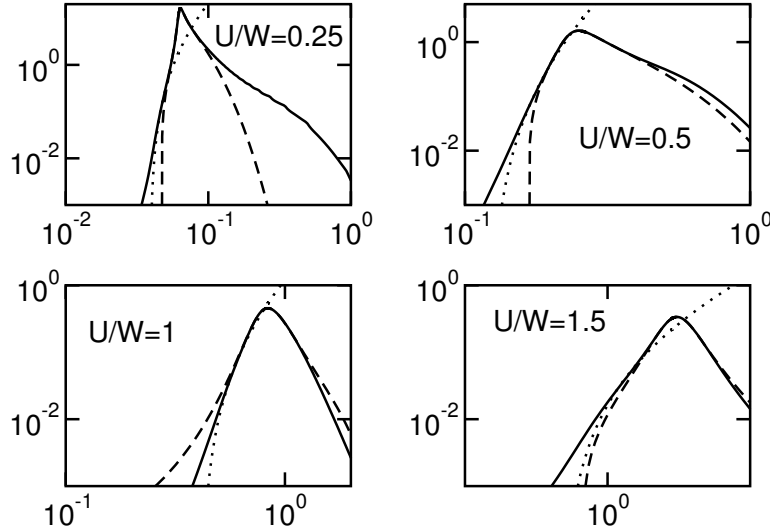


**Fig. 5.8:** Results for the fits to  $\sigma(\omega)$  (full lines) with function (5.2) for  $\omega \approx \omega_0$  (dashed lines) and  $\Theta(\omega - 2\Delta_0) \cdot (\omega - 2\Delta_0)^{5/2}$  in the low- $\omega$  region (dotted lines) for several values of  $U/W$ .

value  $\alpha = 3/2$  used in [Tho94] does not lead to a satisfying description), and the optical gap  $\Delta_c$  is found to be consistent with the spin gap  $\Delta_s$  as  $U \rightarrow 0$ . The good agreement of these two differently calculated quantities (see the inset to Fig. 5.7) also serves as an a posteriori check for the procedure used to determine  $\Delta_c$ . In view of a possible comparison to experimental results [Tho94] this situation is, of course, not satisfying. For this purpose, a more thorough and possibly analytical evaluation of  $\sigma(\omega)$  close to  $\Delta_c$  is required. Unfortunately, the complicated form of the integrals in (3.18) so far have allowed for an analytical evaluation only in the Hartree limit (see Appendix B).

For small  $U/W$ , the optical gap is exactly twice as large as the spin gap and, as becomes apparent from the inset to Fig. 5.7, approaches the Hartree value  $Um_s$  as  $U \rightarrow 0$ . Again, both quantities deviate systematically and by the same amount from the expected Hartree values even for the smallest  $U$ . Thus, even for  $U/W \ll 1$ , correlation effects are important and significantly modify the predictions from Hartree theory [Don91, Don94, Mou01]. For large  $U$ , on the other hand,  $\Delta_c \propto U/W$ , consistent with Mott-Hubbard localized states; furthermore,  $\Delta_s \propto 1/U$  as is expected from the mean-field theory of the Heisenberg model. Further confirmation that the value of the spin gap extracted from the local magnetic susceptibility is correct even quantitatively can be obtained from the fact

that the prefactor of the decay of  $\Delta_s$  for large  $U$  is reproduced correctly. There is, however, no evidence that the Slater limit at  $U/W \rightarrow 0$  and the Mott-Heisenberg limit at  $U/W \rightarrow \infty$  are separated by some kind of phase transition. All results, including the variation of  $\langle n_\uparrow n_\downarrow \rangle$  shown in Fig. 5.7, rather indicate that a smooth crossover takes place for  $U/W \approx 3/4$ .

While in the paramagnetic phase of the Hubbard model at half filling, when artificially extended to  $T = 0$ , a true phase transition from a correlated metal to a Mott-Hubbard insulator at  $U_c \approx W$  has been established, the situation in the physically more relevant Néel state has not been investigated in similar detail up to now. As a first step into this direction, the properties in the ground state of the Hubbard model at half filling with particle-hole symmetry have been discussed in this section. The physical properties at small and large values of the Coulomb interaction  $U$  can be described well within the Slater and Mott-Heisenberg picture respectively. In contrast to the paramagnetic MIT, no evidence of a similar transition in the Néel state has been found; the data rather suggest a smooth crossover, which occurs at a value  $U \lesssim W$ . Even the double occupancy, which in the case of the paramagnetic MIT is an indicator of a phase transition, does not show any sign of a discontinuity.

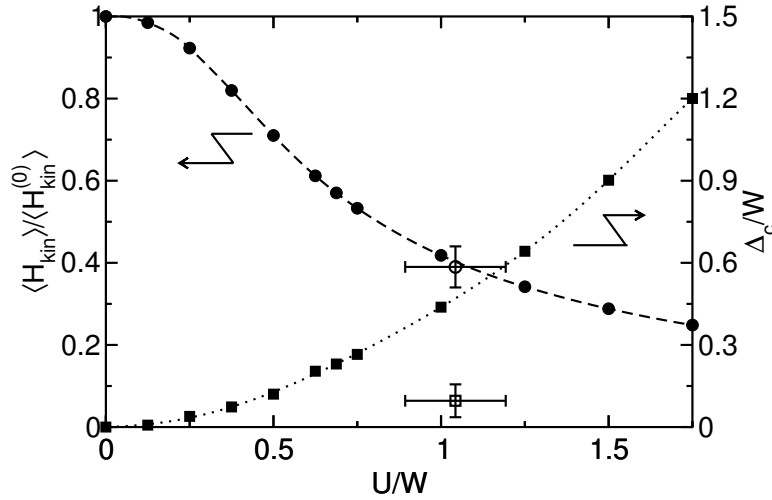


**Fig. 5.9:** Kinetic energy scaled to its value at  $U = 0$  (circles and left scale) and full optical gap  $\Delta_c/W$  (squares and right scale) vs.  $U/W$ . The open circle and square with errorbars represent values for the scaled kinetic energy and  $\Delta_c/W$  respectively, extracted from ref. [Tho94] for the sample of  $V_2O_3$  with  $T_N \approx 50K$ . Note that in ref. [Tho94]  $D = W/2$  and  $\Delta = \Delta_c/2$ .

There are, however, still several unanswered questions. First, the analytic form of the optical conductivity close to the optical gap and the precise value of this gap could not be obtained at present due to the difficulty in evaluating the integral

in (3.18). Especially for a more quantitative comparison with experiment this has to be improved in future work. Second, comparison with the data for  $V_2O_3$  from ref. [Tho94] shows a nice agreement for the kinetic energy (obtained using the optical sum rule), but fails completely concerning the size of the optical gap. This is shown in Figure 5.9, where the kinetic energy scaled to its value for  $U = 0$  (circles and left scale) and  $\Delta_c/W$  (squares and right scale) vs.  $U/W$  is plotted. The open circle and square represent data for the kinetic energy and charge gap, respectively, extracted from ref. [Tho94] for a  $V_2O_3$  sample with  $T_N \approx 50K$ . Obviously, with the present model, the optical gap at intermediate values of  $U$  is overestimated.

Of course, the present investigation did concentrate on the simplest situation, namely a system with perfect particle-hole symmetry. In reality, electron hopping beyond nearest neighbors will destroy antiferromagnetism at small values of  $U$  and consequently lead to different gaps at intermediate values of  $U$ . On the other hand, the gaps at large  $U$  are controlled by Mott-Hubbard physics and will most likely change only little. A similar line of argument has in fact been invoked in [Tho94]. Calculations for the magnetically frustrated Hubbard model indicate that this scenario is indeed very likely. These calculations will be presented in the next section.

### 5.1.3 The Hubbard model with frustration

The Mott-Hubbard metal-insulator transition in the paramagnetic phase of the one-band Hubbard model has long been used to describe similar features in real materials like  $V_2O_3$ . For a proper description of this material, however, the antiferromagnetic phase below  $T_N \approx 160K$  [McW70] has to be taken into account. It was argued and generally accepted [Geo96] that the introduction of partial magnetic frustration in the Hubbard model leads to the anticipated situation, where the MIT extends beyond the antiferromagnetic phase that persists at low temperatures. The merging of these two transitions presents an interesting problem, because it is commonly believed that the magnetic transition should be of second order, while the paramagnetic MIT is a first order transition. Furthermore, previous results for this model with magnetic frustration show an extended antiferromagnetic metallic phase at  $T = 0$ , preceding the transition to the antiferromagnetic insulator [Geo96, Chi99]. This suggests the possibility to link the MIT in the paramagnetic phase with a transition from a metal to an insulator in the antiferromagnetic phase. As with the extension of the NRG formalism presented in Chapter 4 a very reliable method is now available to investigate the antiferromagnetic phase of the Hubbard model at low temperatures, in the following it will be applied to the model including frustration, first on a hypercubic lattice and then, for reasons that will become clear soon, on a Bethe lattice.

## Results for the hypercubic lattice

The natural choice for studying the effect of magnetic frustration is the simple hypercubic lattice with nearest and next-nearest neighbor hopping. In the case of the Néel state as the natural first choice, the system is divided into A and B sublattices, which results in a matrix structure of the DMFT equations (see Sec. 3.3). An antiferromagnetic Néel order then corresponds to a finite staggered magnetization  $m_S > 0$  with  $m_A = m_S$  and  $m_B = -m_S$ . Frustration is introduced by the inclusion of the next-nearest neighbor hopping matrix element  $t'$  in the Hubbard model,

$$H = -t \sum_{nn,\sigma} c_{i\sigma}^\dagger c_{j\sigma} - t' \sum_{nnn,\sigma} c_{i\sigma}^\dagger c_{j\sigma} + U \sum_i n_{i\uparrow} n_{i\downarrow}. \quad (5.3)$$

Here  $nn$  and  $nnn$  denote nearest and next-nearest neighbors respectively. For the hypercubic lattice as shown in Fig. 3.3, the hopping due to  $t'$  takes place along the diagonals, i.e. within one of the two sublattices. Note that in the limit  $d \rightarrow \infty$  the matrix element  $t'$  has to be rescaled according to  $t' = t^*/\sqrt{4d(d-1)}$  [Met89, Mue89]. In the following  $t^*$  is again chosen as the unit of energy.

The Green's function is now given by the matrix

$$G_{\mathbf{k}\sigma}(z) = \begin{pmatrix} \zeta_\sigma(z) - \epsilon'_\mathbf{k} & -\epsilon_\mathbf{k} \\ -\epsilon_\mathbf{k} & \zeta_{\bar{\sigma}}(z) - \epsilon'_\mathbf{k} \end{pmatrix}^{-1}, \quad (5.4)$$

where again  $\zeta_\sigma(z) = z + \mu - \Sigma_\sigma(z)$ . Here, in addition to the dispersion  $\epsilon_\mathbf{k}$  due to the nearest neighbor hopping, the dispersion  $\epsilon'_\mathbf{k}$  due to the hopping along the diagonals enters into the expression for the Green's function. This matrix structure in the Néel state can lead to the challenging problem of a numerical  $\mathbf{k}$  summation in order to calculate the local Green's function  $G_{ii,\sigma}(z)$ . It turns out, however, that in the limit  $d \rightarrow \infty$  it is still possible to convert the  $\mathbf{k}$ -sum into an integration over the energy. This is due to the fact that in this limit the two dispersions are related by [Mue89]

$$\epsilon'_\mathbf{k} = t^*(1 - \epsilon_\mathbf{k}^2), \quad (5.5)$$

where the  $\epsilon_\mathbf{k}$  still have a Gaussian distribution. As a result, the local Green's function can be obtained by evaluating the integral

$$G_{ii,\sigma}(z) = \int_{-\infty}^{\infty} d\epsilon \frac{\rho(\epsilon)(\tilde{\zeta}_{\bar{\sigma}}(z) + t'^*\epsilon^2)}{(\tilde{\zeta}_\sigma(z) + t'^*\epsilon^2)(\tilde{\zeta}_{\bar{\sigma}}(z) + t'^*\epsilon^2) - \epsilon^2}, \quad (5.6)$$

where  $\tilde{\zeta}_\sigma = \zeta_\sigma - t'^*$  and  $\rho(\epsilon)$  is the Gaussian density of states (3.6). This is easily verified by inverting the matrix (5.4). Using some basic algebra it is again possible

to reduce (5.6) to terms that can be evaluated by making use of the function  $w(z)$  that has been introduced in Section 3.2. How this is done in principle can be seen from the calculations in Appendix B.

In the following, results for the hypercubic lattice in the limit  $d \rightarrow \infty$  are presented. The calculations have been performed at  $T = 0$ . The parameters for the NRG are once more  $\Lambda = 2$  and  $b = 0.6$ , and 800 states have been kept in each step of the calculation. The value of  $t'^*$  is  $1/2$ .

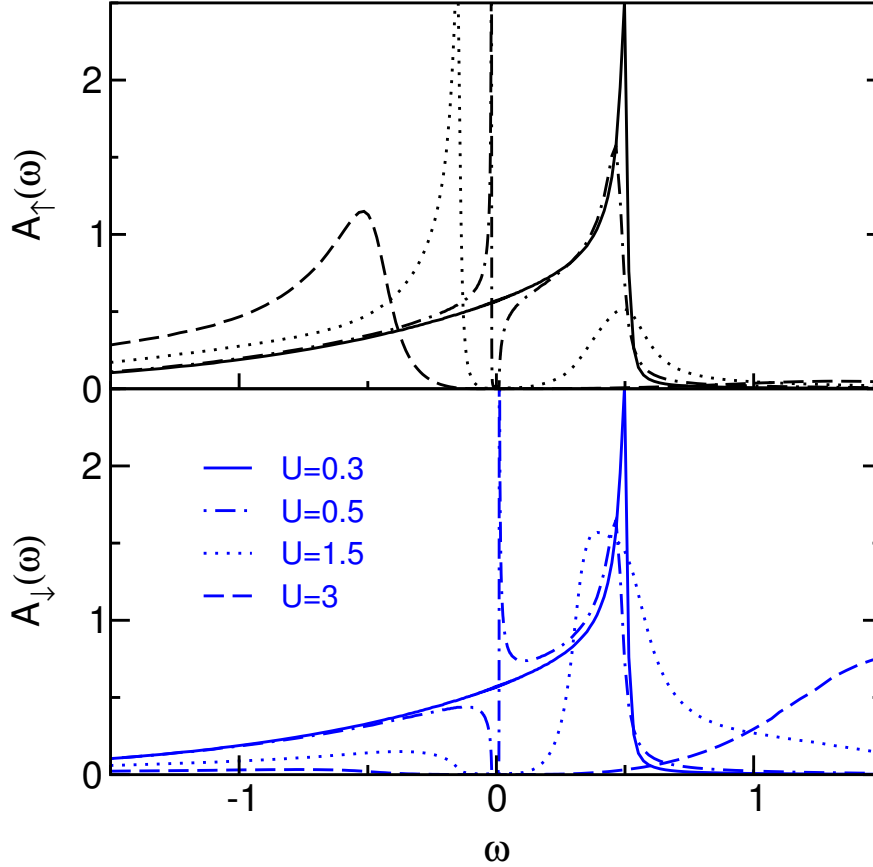


**Fig. 5.10:** *Spin-resolved density of states for the half-filled Hubbard model with frustration. The next-nearest neighbor hopping matrix element  $t'^*$  is  $1/2$ .*

Fig. 5.10 shows the spectral function for both spin up and spin down for different values of  $U$ . Due to the presence of the next-nearest neighbor hopping, the ground state at small values of the Coulomb interaction  $U$  is now paramagnetic (solid line in Fig. 5.10). In addition, a strong asymmetry has been introduced, with a divergence at the upper band edge. This is due to the fact that the sign of  $t'^*$  has been chosen to be the same as that of  $t^*$ . In case of opposite signs, the resulting spectra are simply mirror images of the ones shown here, with a divergence at

the lower band edge. This asymmetry is becoming even more pronounced when  $|t^*|$  is increased. This can also be seen from the non-interacting density of states, which the spectra for the smallest value of  $U$  still closely resemble.

For larger  $U$  the ground state is again antiferromagnetic, with a gap opening at the Fermi energy. Even though the degree of the frustration is rather high, this takes place at a small value  $U_c \approx 0.5$  of the interaction. In order to shift  $U_c$  to higher values,  $t^*$  has to be chosen even larger. The more  $U$  is increased, the larger the staggered magnetization  $m_s$  and the more smeared out the features in the spectral function become. While the transition from the paramagnet to the antiferromagnet seems to be discontinuous, with a sharp drop of the spectral weight at the Fermi energy, a closer examination reveals that it is difficult to clearly identify a metal-insulator transition in this case. This is shown in Figure. 5.11.

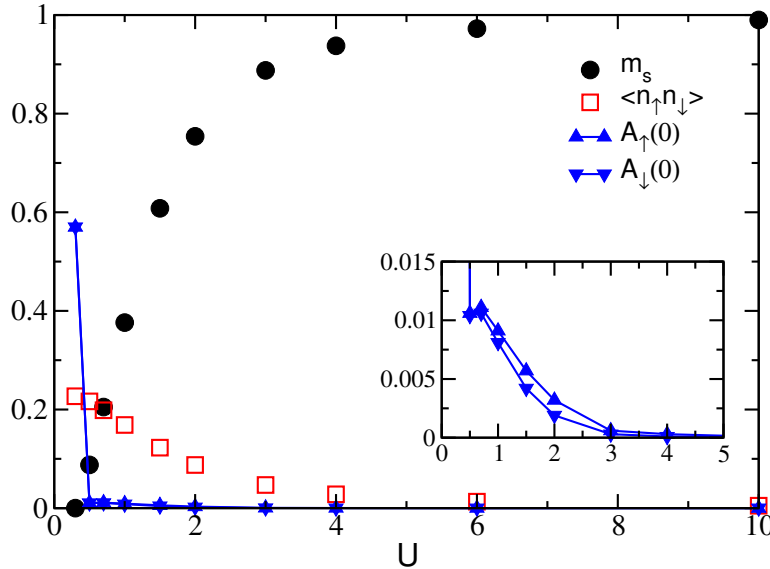


**Fig. 5.11:** Plot of the staggered magnetization, the double occupancy and the spectral weight at the Fermi level for the frustrated Hubbard model on a hypercubic lattice as a function of the Coulomb interaction  $U$ .

Clearly, there is no discontinuity in both the staggered magnetization and the double occupancy as the system enters the magnetic state. Instead, the magnetization increases smoothly with increasing  $U$ , similar to what has been found for the model without frustration. A closer look at the density of states at the Fermi level (see the inset to Fig. 5.11) shows that, while the spectral weight is small, it is by no means zero. It is therefore not possible to associate the onset of magnetic ordering with the existence of a truly insulating solution of the DMFT equations. The reason for this is the fact that the Gaussian DOS of the hypercubic lattice has no real band edges in  $d \rightarrow \infty$ , but stretches to infinity, and

the resulting exponential tails prevent a clear distinction between a metal and an insulator even at  $T = 0$ . This has also been observed in a Hartree calculation for the hypercubic lattice with next-nearest neighbor hopping [Hof98]. In this work the authors observed that, since there is never a true bandgap for the hypercubic lattice in  $d \rightarrow \infty$ , for any finite value of  $t^*$  a transition from a paramagnetic metal to an antiferromagnetic metallic state takes place at some critical value  $U_c$  of the Coulomb interaction.

From Fig. 5.11 and the previous discussion it is also clear that one cannot identify a transition from a metallic to an insulating state in the antiferromagnetic phase, which has been part of the original motivation of the work presented here. It turns out, however, that the problems introduced by the Gaussian density of states can be avoided by using a different underlying lattice structure, one which has clearly defined band edges even in the limit  $d \rightarrow \infty$ . To that end, calculations have been performed on a Bethe lattice, and the results will be presented in the following section.

### Results for the Bethe lattice

The technical problems described previously can be avoided by following a suggestion by Georges et al. [Geo96] and studying the Hubbard model with frustration on a Bethe lattice with infinite coordination number. This is illustrated in Fig. 5.12. Note that the Bethe lattice is also a bipartite lattice, and the for-

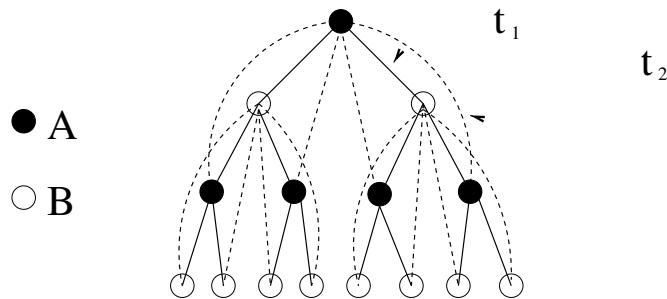


**Fig. 5.12:** Schematic representation of a Bethe lattice with frustration. The Bethe lattice is also a bipartite lattice, and the hopping takes place along the branches of the lattice, with matrix elements  $t_1$  and  $t_2$  between nearest and next-nearest neighbors respectively.

malism described in Section 3.3 can be applied. The only modification is now the calculation of the local Green's function of the lattice, which, for the type of frustration shown in Fig. 5.12, actually leads to a simplification of the DMFT calculations.

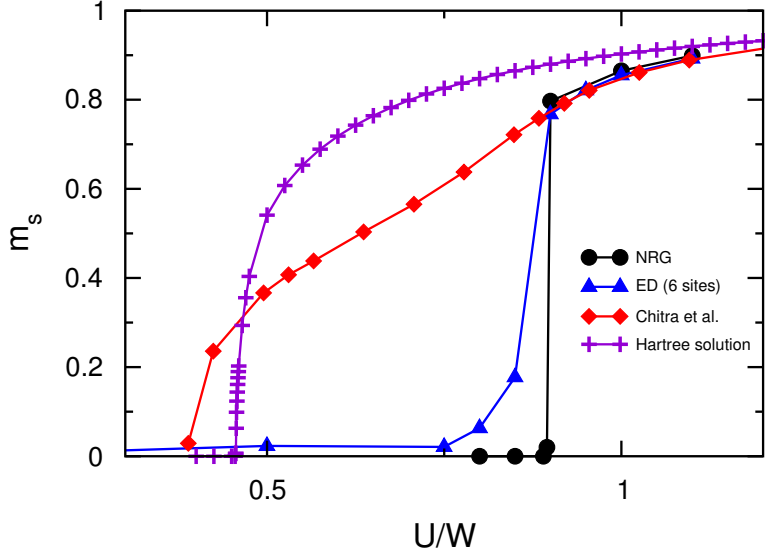


**Fig. 5.13:** Staggered magnetization  $m_s$  as a function of  $U$  at  $T = 0$ . The circles are the results from the NRG; the triangles are results from an ED calculation for 6 sites, while the diamonds are taken from ref. [Chi99]. For comparison, the results of a Hartree calculation are given by the crosses.

Motivated by an early work by Müller-Hartmann [Mue89] for the hypercubic lattice, the hopping as shown in Fig. 5.12 results in a set of real-space DMFT equations for the Bethe lattice [Geo96, Chi99]

$$\begin{aligned}
 G_{A\sigma}(z) &= \frac{1}{z + \mu - \Sigma_{A\sigma}(z) - \frac{t_1^2}{4}G_{B\sigma}(z) - \frac{t_2^2}{4}G_{A\sigma}(z)} \\
 G_{B\sigma}(z) &= \frac{1}{z + \mu - \Sigma_{B\sigma}(z) - \frac{t_1^2}{4}G_{A\sigma}(z) - \frac{t_2^2}{4}G_{B\sigma}(z)},
 \end{aligned} \tag{5.7}$$

which contain magnetic frustration and lead to a density of states with compact support. The bandwidth is  $W = 2\sqrt{t_1^2 + t_2^2}$ , and the non-interacting density of states is semi-circular. In the paramagnetic case, the equations (5.7) reduce to those of a standard Bethe lattice which, for example, has frequently been used to study Mott transition [Geo96, Bul99]. Furthermore, despite the frustration that has now been introduced, the system is still particle-hole symmetric. Especially for half filling this feature reduces the numerical effort quite drastically.

Invoking the symmetry  $G_{A\sigma}(z) = G_{B\bar{\sigma}}(z)$  of the Néel state, eqs. (5.7) reduce to two coupled nonlinear equations which are solved iteratively. Again, the quantity  $\Sigma_\sigma(z)$  is calculated from the solution of the single impurity Anderson model by using the NRG. While in the presence of frustration the Néel state is not the only possible realization of magnetic ordering, it is still reasonable to assume

that in carrying out the calculation as described above the essential changes in the physics introduced to the Hubbard model can indeed be captured, at least on the level of the DMFT. In  $d \leq 2$  the true lattice structure and non-local fluctuations will of course invalidate the DMFT results.

In the following, the results obtained for  $t_2/t_1 = 1/\sqrt{3} \approx 0.58$  are discussed. The bandwidth  $W = 2\sqrt{t_1^2 + t_2^2}$  of the non-interacting system is used as the energy scale. The NRG parameters are once more  $\Lambda = 2$  and  $b = 0.6$ , and in order to make sure that the results are reliable, the calculations have been redone by keeping 1600 states in each step of the NRG, twice as many as usual. This has not lead to any qualitative changes but only slight quantitative ones.

Figure 5.13 shows the staggered magnetization as a function of  $U$  at  $T = 0$ . Here, the results are very surprising. The NRG results in Fig. 5.13 (circles) show a completely different behavior as compared to the data (diamonds) from ref. [Chi99], where the impurity model has been solved using an exact diagonalization (ED) method. Instead of a continuous increase of the staggered magnetization  $m_S$  for  $U > U_c \approx 0.4W$  as suggested by both a Hartree calculation (crosses) and the data from ref. [Chi99], a jump in  $m_S$  at a considerably larger  $U_c \approx 0.9W$  is found.

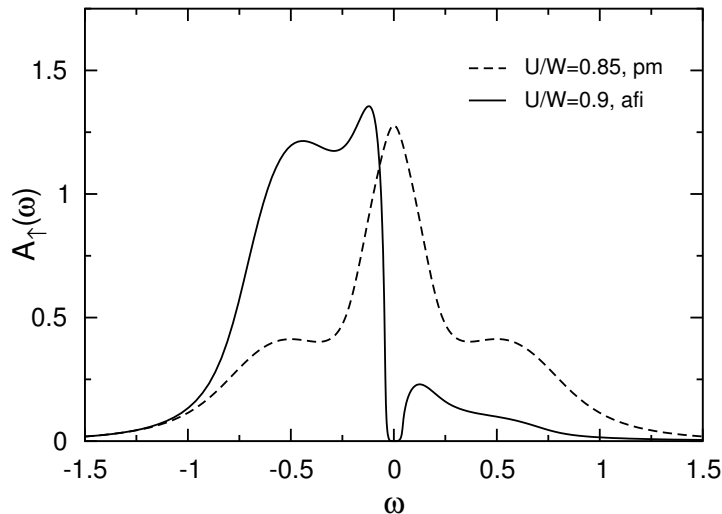


**Fig. 5.14:** *Density of states for spin up on lattice site A at  $T = 0$ .*

To clarify this discrepancy, Ning-hua Tong performed additional ED calculations resulting in the triangles shown in Fig. 5.13. There is a good agreement with the NRG results, and the transition systematically approaches the NRG curve with increasing system size in the ED. Furthermore, a rather strong dependence of the ED results on details of the numerical procedure has been observed, namely on the largest frequency  $\omega_{\max}$  in the calculation of  $G(i\omega)$  and, more importantly, the choice of initial values for the generation of the parameters of the effective

Anderson impurity model from  $G(z)$  [Geo96]. The triangles shown in Fig. 5.13 were obtained using  $\omega_{\max} = 40\pi$  and fixed initial values in each DMFT step. Initializing the ED with results from the previous DMFT iteration leads to a solution similar to the one found in ref. [Chi99]. However, this solution has been found to have a higher total energy than the one obtained by using fixed initial values. The NRG, on the other hand, is stable with respect to changes in the parameters controlling its numerical accuracy.

Another important question is the existence of an antiferromagnetic metallic solution of the DMFT equations for the frustrated Hubbard model. Figure 5.14 shows the NRG results for the density of states at  $T = 0$  and spin up on lattice site  $A$ . Due to particle-hole symmetry the DOS for spin down on  $A$  sites (or spin up on  $B$  sites) can be obtained by taking  $\omega \rightarrow -\omega$ . The full and dashed lines represent the antiferromagnetic insulating solution (AFI) for  $U \searrow U_c$  and the paramagnetic solution (PM) for  $U \nearrow U_c$  respectively. Clearly, the magnetic solution is insulating with a well-developed gap at the Fermi energy. In contrast to the results for the hypercubic lattice, the DOS at the Fermi level is now practically zero, however, as has already been mentioned, due to the broadening of the NRG it can never become exactly zero. Quite generally, no stable antiferromagnetic metallic solution has been found at  $T = 0$  in the calculations for the Bethe lattice presented here.

The discontinuity in the staggered magnetization  $m_s$  at the transition  $\text{PM} \leftrightarrow \text{AFI}$  implies a first order transition and the existence of a hysteresis region, similar to

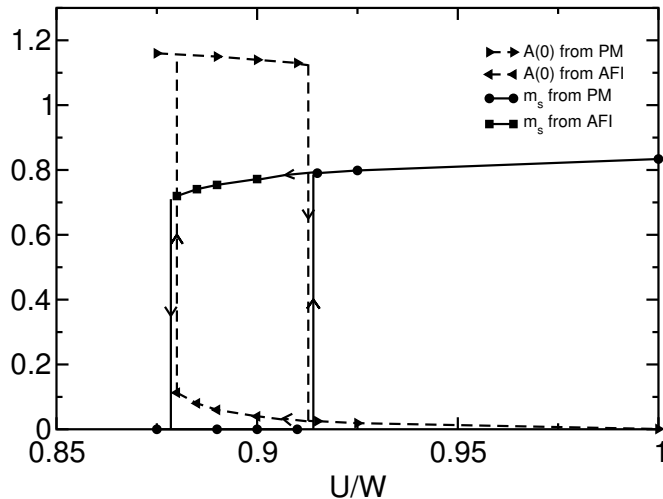


**Fig. 5.15:** Staggered magnetization (solid lines) and total DOS at the Fermi energy (dashed lines) as a function of  $U$  in the vicinity of  $U_c$  for  $T = 0.0155W$ . The arrows indicate that the DMFT solutions have been obtained by either increasing  $U$  ( $\rightarrow$ ) or decreasing  $U$  ( $\leftarrow$ ).

what has been found for the paramagnetic MIT [Geo96, Bul99]. Indeed, starting from the paramagnet at  $U \ll U_c$  and increasing  $U$  results in a magnetization curve different from the one obtained by starting at  $U \gg U_c$  and decreasing  $U$ . This is apparent from Fig. 5.15 (full lines) where a region of hysteresis can be observed in the staggered magnetization (for temperature  $T = 0.0155W$ ). At the same time, the total DOS at the Fermi energy  $A(0) = A_{\uparrow}(0) + A_{\downarrow}(0)$  shows hysteresis between metallic and insulating behavior in exactly the same  $U$  region. Note that due to the finite temperature the DOS at the Fermi level is no longer zero in the Néel state, but strongly reduced as compared to the metal [Bul01]. At  $T = 0$  the results are qualitatively the same, the size of the hysteresis region is somewhat larger and the jumps in both the magnetization and the DOS at the Fermi energy are even more pronounced.

It is of course important to verify that the hysteresis found for small  $U$  is not some kind of artefact of the method used. This can most conveniently be shown by looking at the transition at large  $U$ . Due to the mapping of the Hubbard

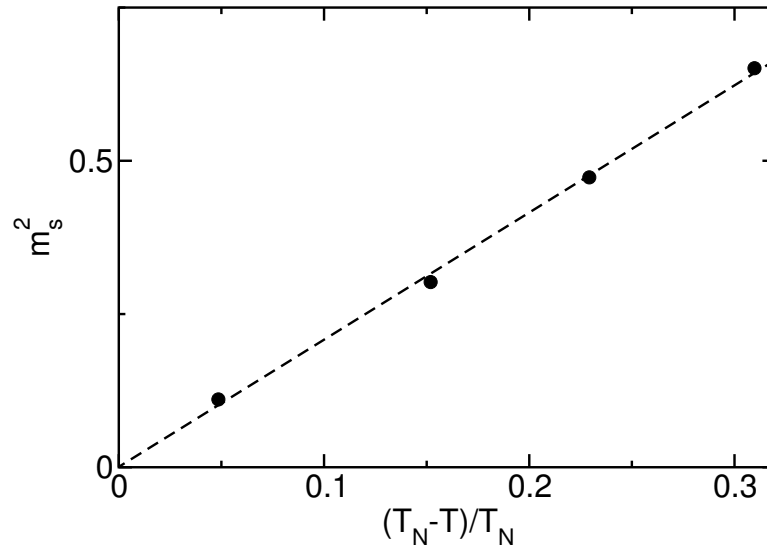


**Fig. 5.16:** Squared staggered magnetization  $m_S$  as a function of  $T$  at  $U/W = 2$ . Note that  $m_S^2$  vanishes continuously like  $T_N - T$  as  $T \searrow T_N$ .

model to a Heisenberg model in this regime, one should expect the transition to be of second order, with the staggered magnetization vanishing continuously like  $m_s \propto \sqrt{T_N - T}$  when approaching  $T_N$  from below. That this is indeed the case is apparent from Fig. 5.16, where the squared staggered magnetization is shown as a function of  $T$  for  $U/W = 2$ . The transition is thus of second order with the expected mean-field exponent in this region of the phase diagram.

Collecting the results for the transitions and the hysteresis region for different

temperatures leads to the phase diagram shown in Figure 5.17. An enlarged view of the region showing coexistence of the PM and the AFI phases is given in the inset, where the full line represents the transition  $\text{PM} \rightarrow \text{AFI}$  with increasing  $U$  and the dashed line the transition  $\text{AFI} \rightarrow \text{PM}$  with decreasing  $U$ . These two lines

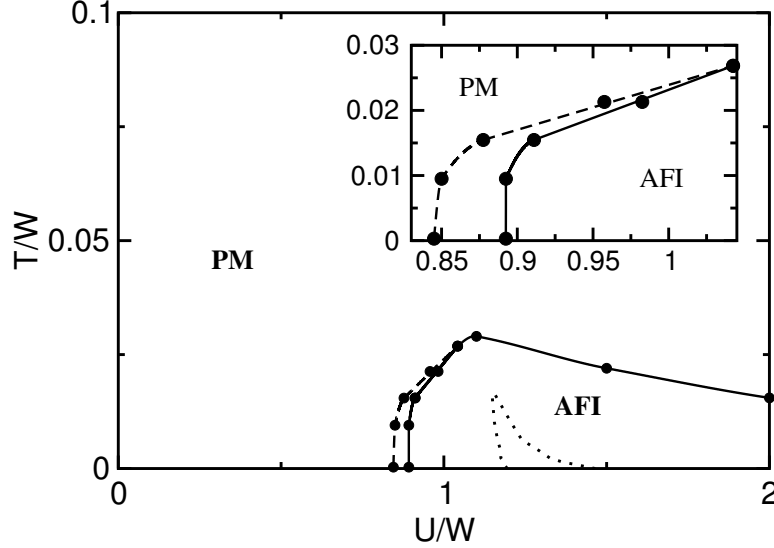


**Fig. 5.17:** *Magnetic phase diagram for the Hubbard model with frustration as defined by eqs. (5.7) and  $t_2/t_1 = 1/\sqrt{3}$ . The dotted lines inside the AFI denote the coexistence region for the paramagnetic MIT. The inset shows an enlarged view of the region with a coexistence of a paramagnetic metal and an antiferromagnetic insulator.*

seem to merge at a value of  $U \approx W$  for this particular value of  $t_2$ , with a critical temperature  $T_c \approx 0.02W$  for this endpoint. Note that even in the presence of such a sizeable  $t_2$ , the antiferromagnetic phase still completely encompasses the paramagnetic MIT (dotted lines in the main panel of Fig. 5.17 [Bul01]).

Obviously, in order to arrive at a scenario where the paramagnetic MIT extends beyond the antiferromagnetic phase, the value of  $t_2$  has to be even larger than the one used in the above calculations. Therefore it is interesting to see how the magnetic phase evolves with increasing  $t_2$  and, in particular, how its boundary crosses the paramagnetic MIT. What is found from the calculations is that increasing  $t_2$  does not change the qualitative behavior of the magnetic phase shown in Fig. 5.17, but mainly shifts the critical  $U$  to higher values and decreases the maximum  $T_N$ . The calculated estimates for these two quantities as a function of  $t_2$  lead to the schematic evolution of the phase diagram presented in Fig. 5.18a-c. Here, only the true phase boundaries are shown. A direct calculation of the free energy at finite temperatures is presently not possible with the NRG method. Therefore, the actual transition line separating the paramagnetic and the anti-

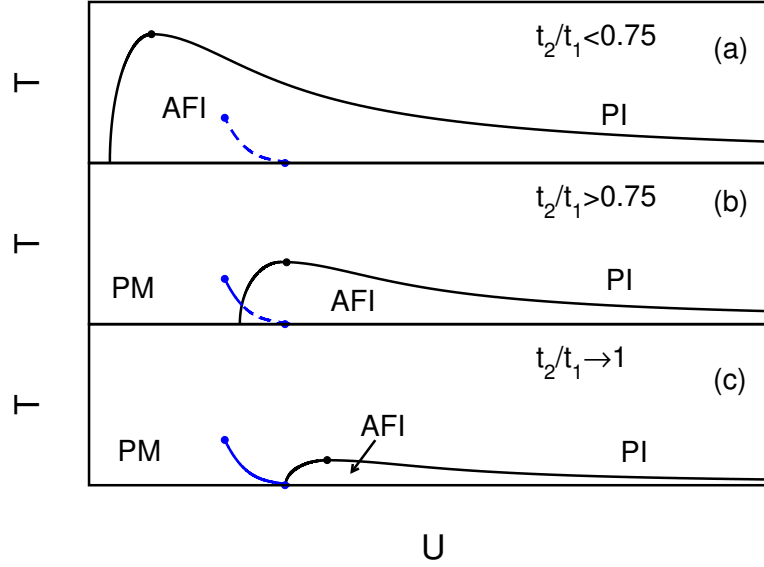


**Fig. 5.18:** Schematic evolution of the magnetic phase diagram with increasing frustration. The dots on the phase transition lines denote the critical endpoints of the first order transitions.

ferromagnetic phase can not be calculated. The transition lines in Fig. 5.18a-c are a guide to the eye only. For the Mott transition, the position of the actual transition line has been calculated [Ton01].

Figure 5.18a shows the qualitative phase diagram corresponding to Fig. 5.17, with the line of first order transitions ending in a critical point. Upon further increasing the value of  $t_2$ , the first order transition lines from both the PM $\leftrightarrow$ AFI and the Mott transition cross (Fig. 5.18b), thus exposing a finite region of the Mott insulator and a transition PI $\leftrightarrow$ AFI. Finally, for even higher values of  $t_2$ , the PM $\leftrightarrow$ AFI transition at  $T = 0$  approaches the Mott transition and  $T_N$  is reduced significantly (Fig. 5.18c). Note that in the limiting case  $t_2 = t_1$  the AFI phase completely vanishes due to the structure of the DMFT equations (5.7). However, as  $t_2 \rightarrow t_1$ , there is always a finite antiferromagnetic exchange  $J \propto (t_1^2 - t_2^2)/U$  between the localized moments for  $U > U_c$  of the Mott transition, which is sufficient to stabilize an antiferromagnetic ground state.

From the results presented in this section one may conclude that a one-band Hubbard model with frustration alone is not sufficient to even qualitatively reproduce the phase diagram of materials like  $V_2O_3$  (see Fig. 2.1). In particular, the Mott transition extends beyond the AFI region only for unphysically large values of  $t_2$ . The question remains whether it is possible at all to reproduce qualitatively the scenario observed in  $V_2O_3$  within some kind of one-band model. Based on the results reported here, it seems that one has to take into account additional

degrees of freedom, for example phonons (within a Holstein-Hubbard model) or orbital degeneracies (within a multi-band Hubbard model).

Another aspect that has to be clarified is the qualitative difference in the results obtained for the Bethe lattice and those for the hypercubic lattice presented in the previous section. It is not clear at present whether this discrepancy is caused by the the Gaussian density of states used in the calculations for the hypercubic lattice, or the strong asymmetry introduced due to the next-nearest neighbor hopping  $t'$  in that case. Additional calculations using even larger values of  $t'$  so far have not revealed any signs of a discontinuous transition both at  $T = 0$  and for finite temperatures. However, as there are numerical difficulties in fixing the filling in this strongly asymmetric case, this scenario can not be excluded.

## 5.2 Results for finite doping

The Hubbard model at half filling  $\langle n \rangle = 1$  has been investigated thoroughly using various approximate and exact techniques [Mon92, Lie95, Tas98b], and its properties are understood to a large extent. In addition, the DMFT calculations presented in Sec. 5.1 have provided new insights into the magnetic properties of this model at low temperatures and also at  $T = 0$ . Off half filling, the model is well understood for  $d = 1$ , but the situation is less clear in dimensions  $d > 1$ . The only rigorous result is due to Nagaoka [Nag66], who proved that a ferromagnetic ground state for the Hubbard model is possible under certain conditions (see Sec. 2.1). It is therefore very useful to apply the method developed in this work also to the model away from half filling. In particular, the NRG allows for the investigation of the ground state of this model within the DMFT. To that end, calculations in both the antiferromagnetic phase at small and intermediate values of the Coulomb interaction and in the ferromagnetic phase at large values of  $U$  have been performed and will be presented in this section.

### 5.2.1 Phase Separation

The relevance of phase separation in the Hubbard model away from half filling has already been discussed in Sec. 2.1. In this section, numerical results for the hypercubic lattice with nearest neighbor hopping at  $T = 0$  within the dynamical mean-field theory are presented. From the formalism of the DMFT as it has been discussed in Chapter 3 it is clear that the investigation of a phase separated, i.e. inhomogeneous state, is difficult within the framework of this theory. In principle the DMFT equations allow only for a homogeneous solution with a fixed occupation number  $\langle n \rangle$ . In addition, they do not allow for the investigation of incommensurate phases, because only magnetic order with a commensurate

wave vector can be implemented. Here, the calculations have again been done for a bipartite lattice with a standard Néel type antiferromagnetic order. The details of this formalism have been described in Sec. 3.3.

The difficulty lies now in controlling the filling when the homogeneous solution (homogeneous concerning the charge distribution) of the DMFT equations turns out to be unstable towards phase separation. Fixing the chemical potential  $\mu$  is not sufficient anymore, as the system will be driven to a filling corresponding to a stable solution, such as  $n = 1$ . To enforce a metastable state with finite doping, a procedure is implemented which has already been used in calculations for the half-filled Hubbard model in a homogeneous magnetic field [Lal94]. The schematic flow diagram of the resulting DMFT self-consistency cycle is shown in Fig. 5.19.

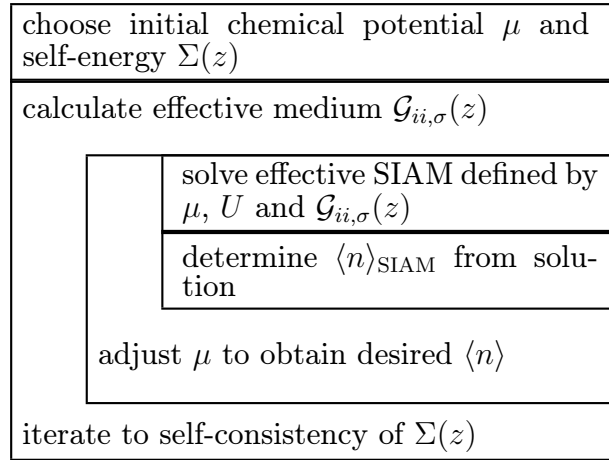


**Fig. 5.19:** Flow diagram for the DMFT self-consistency cycle with fixed filling  $\langle n \rangle$ .

Starting from a paramagnetic solution for the desired doping, a homogeneous or staggered magnetic field is introduced to break the symmetry, and the effective medium  $\mathcal{G}_{ii,\sigma}(z)$  for the DMFT cycle is determined [Pru95, Geo96]. Keeping the medium fixed, one now varies the on-site energy of the effective SIAM until the desired doping has been reached. This result for the self-energy is then used to obtain a new effective medium, and the procedure is repeated until convergence is reached. It should be noted that, for a metastable state, no true convergence can be reached for a finite number of iterations in the sense that the solution, when iterated further without adjusting the filling properly, will flow again to the phase separated one, i.e. either one with filling  $n = 1$  or one with filling  $n \ll 1$ . Typically for such a calculation, the chemical potential between successive DMFT iterations shows a weakly damped oscillatory behavior. The process is therefore repeated until the chemical potential does not change by more than 2-3% between

two successive iterations and the physically interesting quantities do not show any visible qualitative changes. At this point, in order to minimize errors, all quantities are calculated by averaging over several iterations.

To find the correct ground state, one has to calculate the ground state energy

$$\frac{E}{N} = \frac{1}{N} \langle H \rangle = \frac{1}{N} \langle H_t \rangle + \frac{U}{N} \sum_i \langle n_{i\uparrow} n_{i\downarrow} \rangle , \quad (5.8)$$

where  $H_t$  is the kinetic part of the Hamiltonian (2.1). The expectation value  $\langle n_{i\uparrow} n_{i\downarrow} \rangle$  can be determined within the NRG directly. The quantity  $\langle H_t \rangle$ , on the other hand, has to be calculated from the converged result for the spectral function for the phase that is investigated. For the para- and ferromagnetic phases it is simply given by [Pru95, Geo96]

$$\frac{1}{N} \langle H_t \rangle = \sum_{\sigma} \int_{-\infty}^{\infty} d\epsilon \epsilon \rho^{(0)}(\epsilon) \int_{-\infty}^{\infty} d\omega f(\omega) A_{\sigma}(\epsilon, \omega) , \quad (5.9)$$

with  $\rho^{(0)}(\epsilon)$  the density of states (DOS) for the non-interacting system,  $f(\omega)$  the Fermi function and

$$A_{\sigma}(\epsilon, \omega) = -\frac{1}{\pi} \Im m \frac{1}{\omega + \mu - \epsilon - \Sigma_{\sigma}(\omega + i0^+)}$$

the spectral function of the Hubbard model in the DMFT.

In the antiferromagnetic state with Néel order, one has to take into account the AB lattice structure, and it is easily verified that in this case the formula becomes

$$\frac{1}{N} \langle H_t \rangle = 2 \int_{-\infty}^{\infty} d\epsilon \epsilon \rho^{(0)}(\epsilon) \int_{-\infty}^{\infty} d\omega f(\omega) B(\epsilon, \omega) \quad (5.10)$$

instead, with

$$B(\epsilon, \omega) = -\frac{1}{\pi} \Im m \frac{1}{\sqrt{\zeta_{\sigma}(\omega) \zeta_{\bar{\sigma}}(\omega)} - \epsilon}$$

and  $\zeta_{\sigma}(\omega) = \omega + \mu - \Sigma_{\sigma}(\omega + i0^+)$ . Obviously, expression (5.10) reduces to (5.9) without magnetic order, i.e.  $\zeta_{\sigma}(\omega) = \zeta_{\bar{\sigma}}(\omega)$ .

For the hypercubic lattice, the resulting non-interacting density of states is the Gaussian (3.6), and the unit of energy is again defined by  $t^*$ .

### Weak-coupling results

It is useful to review some of the weak-coupling results [Don91, Don94, Don96], as these will be frequently referred to in the following section. Since the hypercubic lattice is a bipartite lattice, one obtains in lowest order, i.e. in a Hartree

approximation, a transition to a Néel state for any  $U > 0$  at  $T = 0$  below a critical doping  $\delta_c^H(U)$ . For small  $U \rightarrow 0$ , the magnetization  $m$  as well as the critical doping depend non-analytically on  $U$ , i.e.  $m, \delta_c^H \propto \exp(-1/(U\rho^{(0)}(0))) / U$ , independent of the dimension  $d$ .

A quantity that is of particular interest in the DMFT is the single-particle Green's function. The general structure of the Green's function in the Néel state for both Hartree theory and DMFT has been introduced in Sec. 3.3, where in the Hartree approximation  $\Sigma_\sigma(z)$  reduces to  $\Sigma_\sigma^H(z) = Un_{\bar{\sigma}} = \frac{1}{2}U(n - \sigma m)$  where  $n$  is the filling and  $m$  the magnetization. The local Green's function is obtained by summing over the wave vectors  $\mathbf{k} \in \text{MBZ}$ , which yields for example for spin up

$$G_{ii,\uparrow}(\omega) = \frac{\zeta_\downarrow(\omega)}{\sqrt{\zeta_\uparrow(\omega)\zeta_\downarrow(\omega)}} G^{(0)}\left(\sqrt{\zeta_\uparrow(\omega)\zeta_\downarrow(\omega)}\right) \quad (5.11)$$

with  $\zeta_\sigma(\omega) = \omega + i0^+ + \mu - \frac{U}{2}n + \sigma\frac{U}{2}m$  and

$$G^{(0)}(z) = \int_{-\infty}^{\infty} d\epsilon \frac{\rho^{(0)}(\epsilon)}{z - \epsilon} . \quad (5.12)$$

It is now useful to define

$$\begin{aligned} \omega_- &= \frac{U}{2}n - \mu - \frac{U}{2}m \\ \omega_+ &= \frac{U}{2}n - \mu + \frac{U}{2}m . \end{aligned}$$

Then, as long as  $\omega \leq \omega_-$  or  $\omega \geq \omega_+$ , the radicant in (5.11) is positive, and the resulting DOS can be expressed as

$$\rho_\uparrow(\omega) = \frac{\zeta_\downarrow(\omega)}{\sqrt{\zeta_\uparrow(\omega)\zeta_\downarrow(\omega)}} \rho^{(0)}\left(\sqrt{\zeta_\uparrow(\omega)\zeta_\downarrow(\omega)}\right) .$$

For  $\omega_- < \omega < \omega_+$ , on the other hand, the radicant in (5.11) is negative, i.e.  $\sqrt{\zeta_\uparrow(\omega)\zeta_\downarrow(\omega)} = i\sqrt{|\zeta_\uparrow(\omega)\zeta_\downarrow(\omega)|}$ . Since the Green's function  $G^{(0)}(z)$  defined in (5.12) for purely imaginary arguments is purely imaginary, too, one finds

$$\rho_\uparrow(\omega) = 0 ,$$

i.e. the DOS has a gap between  $\omega_-$  and  $\omega_+$ . As one approaches  $\omega_-$  from below or  $\omega_+$  from above, it is easy to confirm that

$$\rho_\uparrow(\omega) \approx \begin{cases} \sqrt{\frac{Um}{|\omega - \omega_-|}} \rho^{(0)}(0) & \omega \nearrow \omega_- \\ \sqrt{\frac{|\omega - \omega_+|}{Um}} \rho^{(0)}(0) & \omega \searrow \omega_+ \end{cases} . \quad (5.13)$$

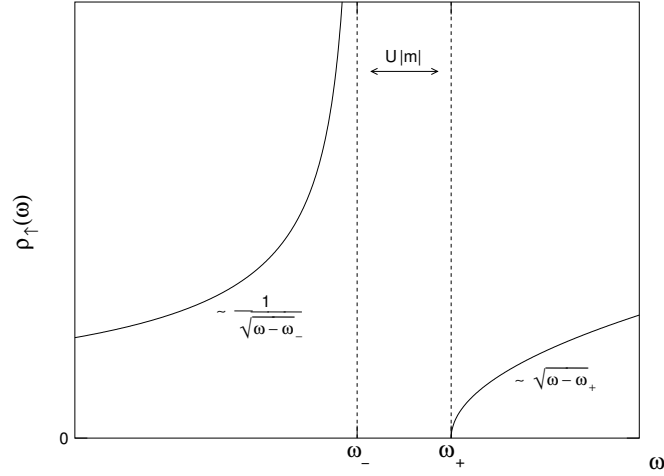


**Fig. 5.20:** Behavior of the DOS for the majority spins on a particular sublattice in Hartree approximation close to the gap edges.

The corresponding DOS for  $\sigma = \downarrow$  has a similar behavior. Here, however, the DOS diverges like  $1/\sqrt{|\omega - \omega_+|}$  at the upper gap edge, and it vanishes like  $\sqrt{|\omega - \omega_-|}$  at the lower one. This is summarized in Figure 5.20.

In order to determine the thermodynamically stable phase, one has to calculate the ground state energy as a function of the doping  $\delta = 1 - n$ . The result, up to second order in  $U$ , is [Don96]

$$E(\delta) - E(0) = -\frac{U}{2}\delta + \alpha^{\text{H}} \cdot \Phi^{\text{H}}(\delta/\delta_1) , \quad (5.14)$$

where

$$\Phi^{\text{H}}(x) = \begin{cases} \frac{1}{2}x \left(1 - \frac{1}{4}x\right) & x < 1 \\ \frac{1}{4} \left(1 + \frac{1}{2}x^2\right) & x > 1 \end{cases} \quad (5.15)$$

and  $\delta_1$  is the critical doping for antiferromagnetism in Hartree approximation. The coefficient  $\alpha^{\text{H}}$  is given by  $\alpha^{\text{H}} = 2\delta_1^2/\rho^{(0)}(0)$ . The function  $\Phi^{\text{H}}(\delta/\delta_1)$  appearing in expression (5.14) leads to the full line in Fig. 5.21. Apparently, this function is not convex for small  $\delta$ , i.e. the resulting phase is thermodynamically unstable towards phase separation for doping levels less than  $\delta_c = \sqrt{2}\delta_1$ . The resulting ground state energy is then obtained from a Maxwell construction, given by the straight dashed line in Fig. 5.21.

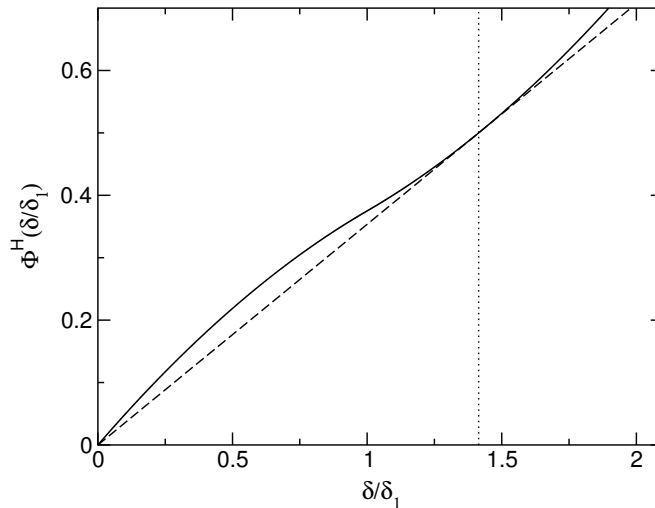


**Fig. 5.21:** The function  $\Phi^H(\delta/\delta_1)$  from Eq. (5.15). Note the concave curvature between  $\delta = 0$  and  $\delta = \delta_1$ . The dashed line shows the actual behavior of the ground state energy following from a Maxwell construction.

### Results of the DMFT calculations

The case of half filling  $n = 1$  has been discussed extensively in Sec. 5.1.2. There, the Néel phase is energetically stable. The variation of the DOS for increasing  $U$  has been shown in Fig. 5.3. As expected, the DOS for small  $U$  resembles the form (5.13) predicted for weak-coupling, i.e. remnants of the characteristic square-root divergence can be seen in the density of states for spin up at the lower gap edge and a corresponding power law is found at the upper gap edge. These characteristic features vanish rapidly with increasing  $U$ , and already for  $U = 3$  the DOS mainly consists of the Hubbard peaks at  $\omega = +U/2$  and  $\omega = -U/2$  for  $\sigma = \downarrow$  and  $\sigma = \uparrow$  respectively.

Keeping  $U$  fixed at  $U = 3$  and increasing  $\delta$  leads to the spectra shown in Fig. 5.22. Quite interestingly, the typical weak-coupling characteristics reappear in the spectra for small doping and are still recognizable for  $\delta = 13\%$ . Note also that, upon variation of doping and hence of the magnetization, the spectra are not shifted in the same way as in Hartree theory. Instead, the dominant effect is a strong redistribution of spectral weight from the Hubbard bands to the Fermi level. Eventually, in the paramagnetic phase one recovers the well-known three peak structure of the doped Hubbard model in the DMFT [Pru95, Geo96].

The evolution of the spectra both at and away from half filling can be understood within a simple picture. In Fig. 5.23 a sketch of the Hartree bandstructure of the Hubbard model in the Néel state is shown, which has two branches in the MBZ and a gap of width  $\propto U|m|$  between them. If, on the other hand, the

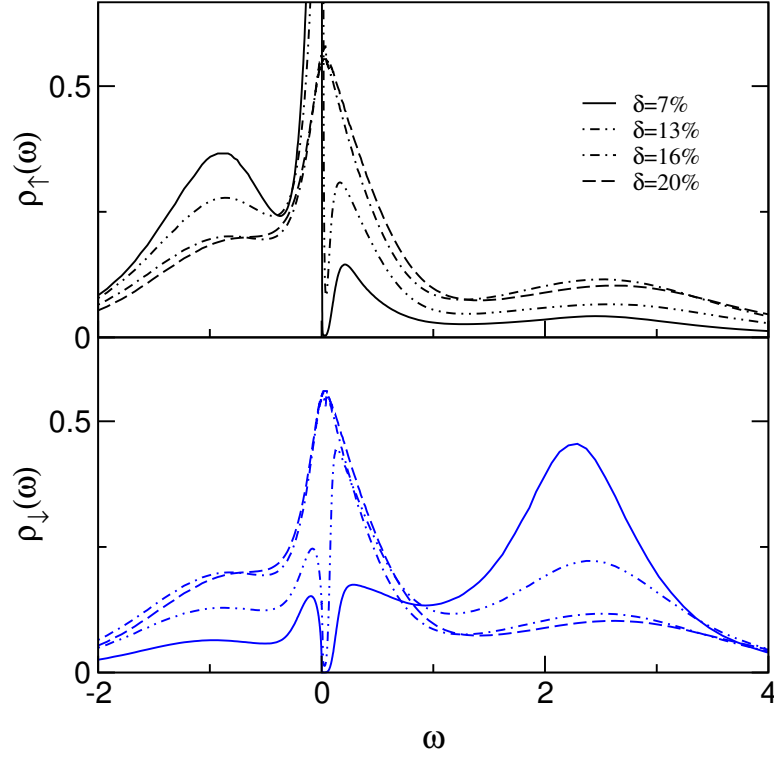


**Fig. 5.22:** DOS for spin up and down for  $U = 3$  and different dopings  $\delta$ . For  $\delta = 20\%$  the system is already in the paramagnetic phase.

paramagnetic solution is considered, one finds at half filling and for small values of  $U$  a Fermi liquid with quasiparticles defined on an energy scale larger than  $U|m|$ . This situation is indicated by the arrow labeled (a) on the left side of Fig. 5.23. Here it is expected for the antiferromagnetic solution (see full curve in Fig. 5.3) to have a DOS that shows the characteristic van Hove singularities of Fig. 5.20. Increasing  $U$  eventually leads to a situation where the energy scale for the quasiparticles in the paramagnetic state is finite but much smaller than  $U|m|$  (arrow (b) in Fig 5.23). The self-energy in the energy region of the van Hove singularities then has a large imaginary part and will completely smear out the characteristic structures. Upon further increasing  $U$ , the picture will not change qualitatively. With finite doping, the chemical potential is moved into e.g. the lower band. This means that even for a relatively small quasiparticle energy scale, one again finds the van Hove singularities at the band edges, which results in the well defined structures in the spectra for small doping in Fig. 5.22.

From the occupation numbers  $n_\sigma$  obtained after of the DMFT calculation has converged, one can calculate the magnetization  $m = (n_\uparrow - n_\downarrow)/(n_\uparrow + n_\downarrow)$  as a function of the doping  $\delta$ . The results for  $U = 1$  and  $U = 3$  are shown in Fig. 5.24,

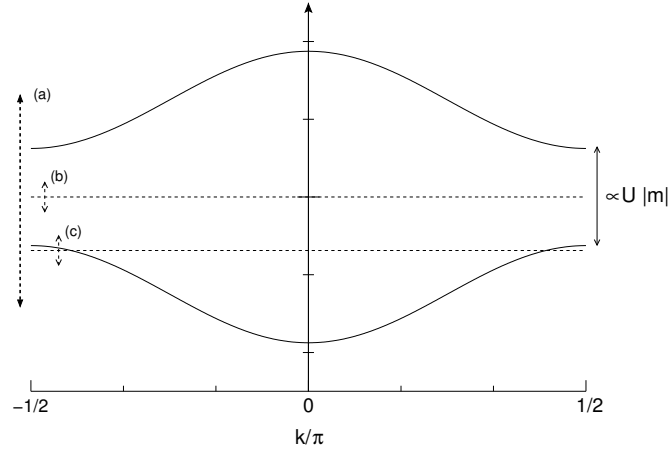


**Fig. 5.23:** Schematic picture of the Hartree bandstructure of the Hubbard model in the Néel state. A detailed explanation is given in the text.

together with a fit to a power law of the form

$$m(\delta) = m_0 \left| 1 - \frac{\delta}{\delta_c^{\text{AF}}} \right|^\nu. \quad (5.16)$$

The resulting fit parameters are summarized in Table 5.1. As expected for a mean-field theory, the value for the critical exponent is  $\nu = 1/2$ .

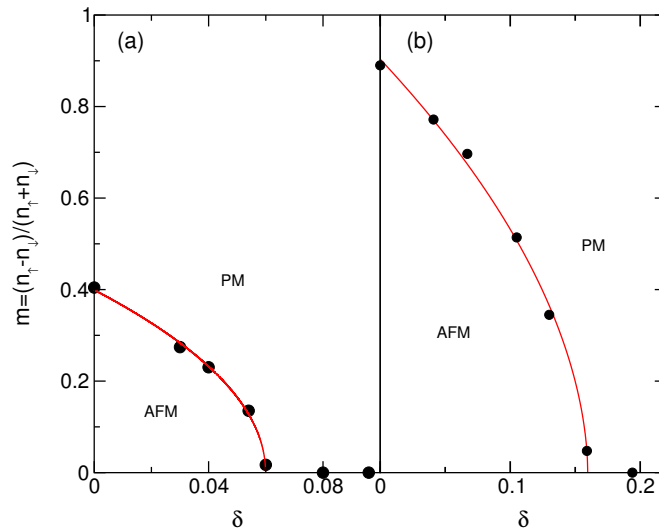


**Fig. 5.24:** Doping dependence of the magnetization per electron for  $U = 1$  (a) and  $U = 3$  (b). The full lines are fits with the function (5.16), the resulting fit parameters are summarized in Table 5.1.

Finally, with the converged DMFT self-energy  $\Sigma_\sigma(z)$  one can calculate the expectation value  $\langle H \rangle / N$  according to eqs. (5.8) and (5.9) as well as (5.10) for the paramagnetic and the antiferromagnetic phase respectively. The results for the characteristic function

$$\Phi(\delta) = E(\delta) + \frac{U}{2}\delta - E_{\text{mag}}(0)$$

are summarized in Fig. 5.25.

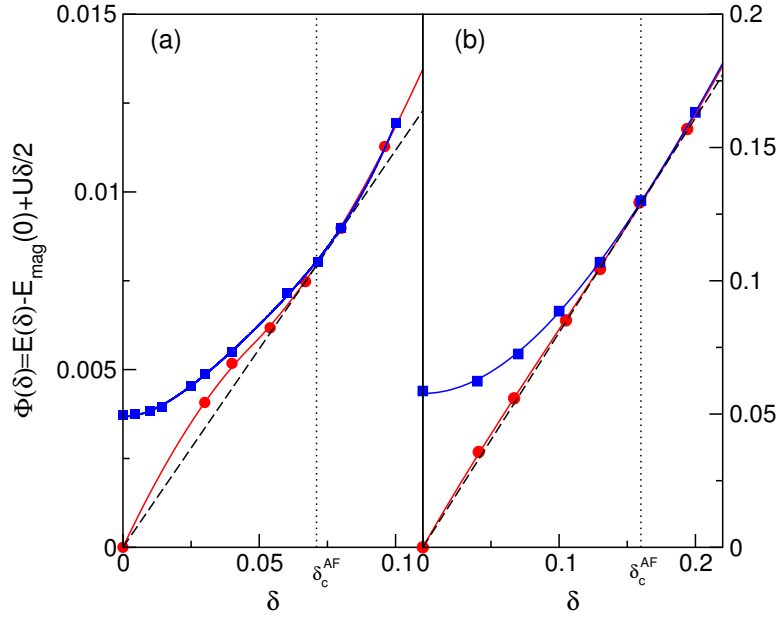


**Fig. 5.25:** Doping dependence of the energy of the paramagnetic phase (squares) and the Néel state (circles) for  $U = 1$  (a) and  $U = 3$  (b). The full lines are fits with the function (5.17), the corresponding fit parameters are summarized in Table 5.1. The dashed lines are the result of a Maxwell construction for the ground state energy.

In Fig. 5.25 the energies of the antiferromagnetic phase are represented by the circles, those of the paramagnetic phase by the squares. The full lines interpolating the antiferromagnetic data are fits to the function

$$\Phi(\delta) = \alpha \Phi^{\text{H}}(\delta/\delta_1) + \gamma \left( \frac{\delta}{\delta_1} \right)^3 \quad (5.17)$$

with  $\Phi^{\text{H}}(x)$  according to (5.15). The fit parameters are summarized in Table 5.1. The use of the function  $\Phi^{\text{H}}(x)$  in (5.17) is motivated by the results of van Dongen [Don96]. The lines interpolating the paramagnetic data are meant as guides to

$U$	Magnetization			Energy			
	$m_0$	$\delta_c^{\text{AF}}$	$\nu$	$\delta_c^{\text{PS}}$	$\delta_1$	$\alpha/\alpha^{\text{H}}$	$\gamma$
1	0.4	0.06	0.49	0.07	0.047	0.52	0
3	0.9	0.16	0.54	0.157	0.191	0.33	0.026

**Tab. 5.1:** Results for the fits of  $m(\delta)$  in Fig. 5.24 to expression (5.16) and  $E(\delta)$  in Fig. 5.25 to (5.17).

the eye only. The dotted vertical lines denote the value  $\delta_c^{\text{AF}}$  as obtained from Fig. 5.24.

The antiferromagnet obviously has the lower energy as compared to the paramagnet in the region  $0 \leq \delta \leq \delta_c^{\text{AF}}$ . However, in both cases  $U = 1$  and  $U = 3$  a non-convex behavior in  $E(\delta)$  is found in that region, i.e. the aforementioned signature of an instability towards phase separation. The true ground state energy as a function of  $\delta$  is obtained again via a Maxwell construction, leading to the dashed lines in Fig. 5.25 and the values  $\delta_c^{\text{PS}}$  given in Table 5.1. Note that in both cases  $\delta_c^{\text{AF}} \approx \delta_c^{\text{PS}}$  within the accuracy of the fitting procedure.

While for  $U = 1$  the function  $\Phi(\delta)$  nicely follows the weak-coupling prediction (5.14) with a renormalized constant  $\alpha$ , one finds a sizeable contribution  $\sim \delta^3$  for  $U = 3$ . This additional term results in a much weaker non-convex behavior of  $E(\delta)$  for  $U = 3$ .

For values  $U > 4$  a stable solution with Néel order and well-defined doping  $\delta > 0$  could not be obtained from the DMFT calculations, although for  $\delta < \delta_c(U)$  the paramagnetic phase becomes unstable. Instead, the numerical calculations produce a cycle encompassing a range of fillings instead of one solution with a well-defined filling. It might be interesting to note that at least each of the fillings in this cycle has a unique magnetization associated with it, and that all spectra in this cycle correspond to an insulator. Currently it is neither clear what type of magnetic solution this may correspond to, nor whether the breakdown of the Néel state is a true physical effect or due to numerical problems. Since at half filling the Néel state is present at these values of  $U$ , incommensurate structures or again a phase separated state seem to be possible. At even larger values of  $U$  a ferromagnetic state can be stabilized within the DMFT calculations. This is discussed in the following section.

## 5.2.2 Ferromagnetism

For values of the Coulomb interaction  $U$  beyond  $U_c \approx 25$  yet another magnetic phase appears, namely the ferromagnet. The existence of this phase has been

observed in the case of a hypercubic lattice and  $U = \infty$  [Obe97b] and for a generalized fcc lattice [Vol97, Ulm98] before. Since these calculations have been done at finite and comparatively high temperatures, questions regarding the ground state magnetization and, especially in the case of a hypercubic lattice, the actual extent of the ferromagnetic phase in the  $(\delta, U)$  parameter space have not been discussed in detail so far. With the NRG, the whole range of parameters  $U$  and  $\delta$  has now become accessible, in particular at  $T = 0$ .

As an example for the ferromagnetic phase at  $T = 0$ , Fig. 5.26 shows the local DOS for two different values of the doping  $\delta$  and a value of the Coulomb interaction  $U = 50$ . It is quite apparent from the DOS in Fig. 5.26 that the ferromag-

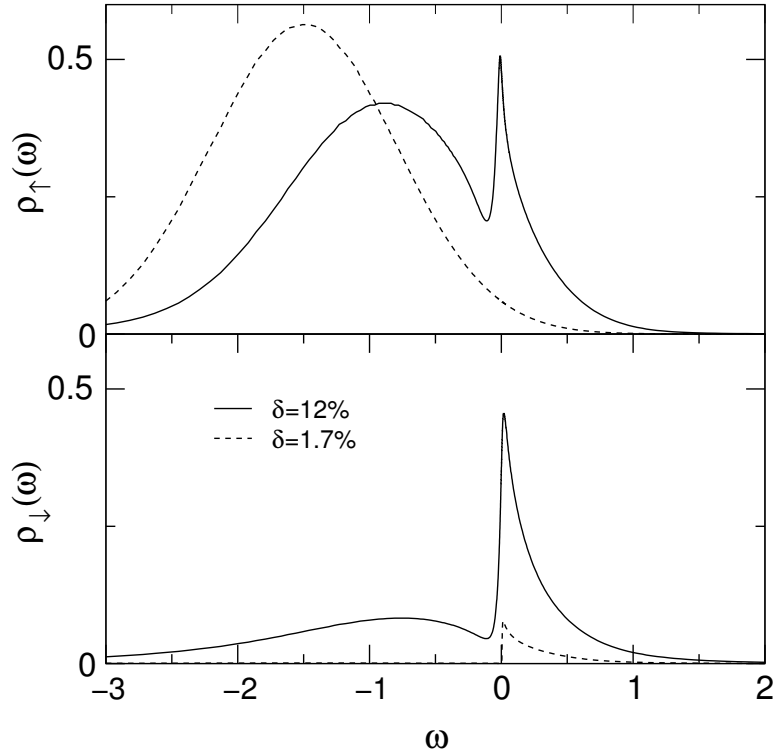


**Fig. 5.26:** Local density of states for  $U = 50$  and two characteristic dopings  $\delta = 12\%$  (full lines) and  $\delta = 1.7\%$  (dashed lines). In contrast to Stoner theory, one finds comparatively small shifts in the spectra, but rather a strong redistribution of spectral weight.

netism found here cannot be understood on the basis of the typical Stoner theory. In contrast to a shift of the spectrum expected in the latter, what is observed here is a strong redistribution of spectral weight. Still, the typical structures due to the strong correlations, namely the quasiparticle peak at the Fermi energy, are still present. Only in the case  $\delta \rightarrow 0$  the spectrum again resembles that of the

free system for the (almost completely polarized) majority spins. The minority spins become strongly depleted below the Fermi level, the spectral weight can be found almost completely in the upper Hubbard band situated around  $\omega \approx U/2$  (not shown in the figure). Nevertheless, a tiny resonance just above the Fermi energy can be seen even as  $\delta \rightarrow 0$ .

Figure 5.27 shows the magnetization per electron,  $m(\delta) = (n_\uparrow - n_\downarrow)/(n_\uparrow + n_\downarrow)$ , as a function of doping for  $U = 50$ . The data for  $m(\delta)$  in Fig. 5.27 are fitted to

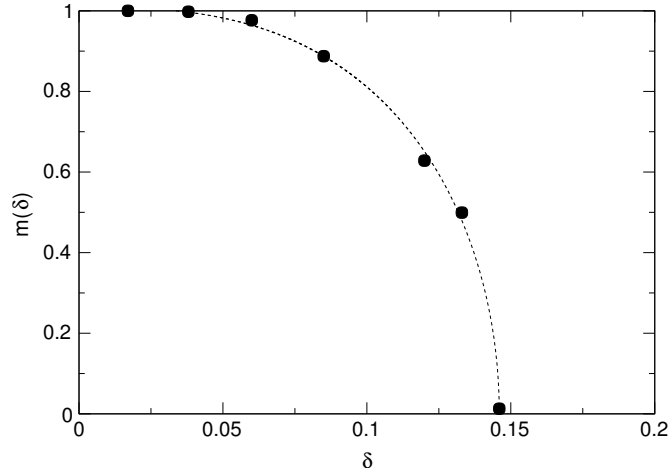


**Fig. 5.27:** Ferromagnetic magnetization per electron as a function of doping  $\delta$  for  $U = 50$ . The full line is a fit to the function (5.18). The critical doping is  $\delta_c \approx 14.6\%$ . Note that for  $\delta \rightarrow 0$  the results are consistent with a fully polarized ferromagnetic state.

the function

$$m(\delta) = m_0 \cdot \sqrt{1 - \left(\frac{\delta}{\delta_c}\right)^\nu}, \quad (5.18)$$

and the result is given by the dotted line. The parameters for the fit are  $m_0 = 1$ ,  $\delta_c = 14.6\%$  and  $\nu = 2.75$ . While for  $\delta \nearrow \delta_c$  the typical mean-field behavior, i. e.  $m(\delta) \propto \sqrt{1 - \delta/\delta_c}$ , is obtained, the result for  $\delta \rightarrow 0$  is rather unconventional,

$$m(\delta) \propto 1 - \frac{1}{2} \left(\frac{\delta}{\delta_c}\right)^{2.75}.$$

This fit assumes that a fully polarized state is only reached as  $\delta \rightarrow 0$  [Faz90, Uhr96]. Note, however, that the numerical results for the magnetization  $m(\delta)$  for small  $\delta$  are also consistent with a fully polarized ferromagnet at finite  $\delta$ . From the numerical data it is very difficult to distinguish between a fully polarized state and an *almost* fully polarized state.

### Summary of the results

With the results from the previous two sections, the ground state properties of the Hubbard model on a hypercubic lattice with nearest neighbor hopping both at and off half filling have now been investigated for the whole range of the Coulomb interaction  $U$  within the DMFT. While at half filling the ground state is antiferromagnetic for all  $U > 0$ , it seems that at least for the weak and intermediate coupling regime this type of magnetic ordering can only be realized in a phase separated state for any finite doping, thus supporting and extending earlier weak-coupling predictions.

The mapping of the Hubbard model for large  $U$  onto an antiferromagnetic tJ-model strongly suggests the dominance of antiferromagnetism in the ground state. The results obtained in this work show, however, that the type of magnetic order for intermediate values of the Coulomb interaction  $U$  away from half filling is still an open question. Furthermore, the importance of phase separation (which is observed for  $U \leq 3$ ) still has to be clarified for larger values of  $U$ .

These results are summarized in the schematic  $(\delta, U)$  ground state phase diagram of Fig. 5.28. To allow for the inclusion of all values  $0 \leq U < \infty$ , the ratio

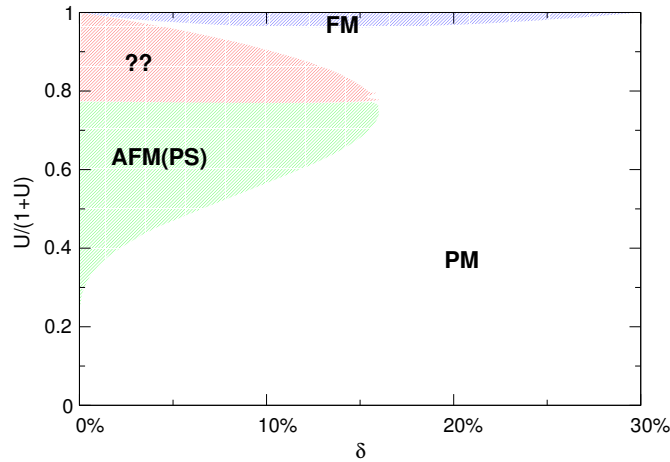


**Fig. 5.28:** Schematic ground state phase diagram for the Hubbard model. At half filling ( $\delta = 0$ ) the ground state is antiferromagnetic. Close to half filling and for small  $U$  a phase separated antiferromagnet is found. For values of  $U$  beyond  $U \approx 4$  a magnetic phase is observed, but its precise character could not be identified within the DMFT. For very large  $U > 25$  and up to  $\delta \approx 30\%$  a ferromagnetic phase is found.

$U/(1+U)$  is used on the abscissa. Close to half filling, a phase separated Néel state is found, up to a value of  $U < 4$ . The magnetization as a function of the doping follows a typical mean-field behavior in all cases studied, and the

spectra show the characteristic van Hove singularities of the band structure in the Néel state in cases where the characteristic energy scale of the paramagnet is large enough. Most important is the observation that, as is typical for correlated systems, the spectra are not strongly shifted, as e.g. predicted by Hartree theory, but rather show a large redistribution of spectral weight. For values of  $U > 4$  the system shows a tendency towards a magnetic instability, which could not be further identified due to technical problems in the solution of the DMFT self-consistency equations. However, at least ferromagnetism can be excluded in this region, and a speculative possibility is the occurrence of incommensurate phases or magnetic phases with additional charge order. While the former cannot be addressed within the present method, the latter should be investigated further.

At very large values of  $U > 25$  there is a region of ferromagnetism, extending between  $0 < \delta < 30\%$  as  $U \rightarrow \infty$ . For a fixed value of  $U$ , the magnetization per electron in the ferromagnetic state shows a tendency to saturate near half filling. However, from the numerical data it is of course impossible to reliably conclude whether the system is fully polarized at a finite  $\delta$  already or only as  $\delta \rightarrow 0$ . The data are consistent with both scenarios, but the latter is supported by analytical treatments of the case  $\delta \rightarrow 0$ . As in the case of the antiferromagnet, the spectrum shows a rather strong redistribution of spectral weight, not simply a shift of the features, as would be expected from Stoner theory.

The phase diagram shows a peculiarity, which has already been pointed out by Obermeier et al. [Obe97b]. In the region of very large  $U$  and  $\delta \rightarrow 0$  there exists the possibility of a direct transition between the magnetic phase at intermediate values of  $U$  and the ferromagnet. At the point  $(\delta, U) = (0, \infty)$  all possible spin configurations are degenerate, and one can speculate what the phase diagram looks like as  $(\delta, U) \rightarrow (0, \infty)$ . Generic possibilities are sketched in Fig. 5.29.

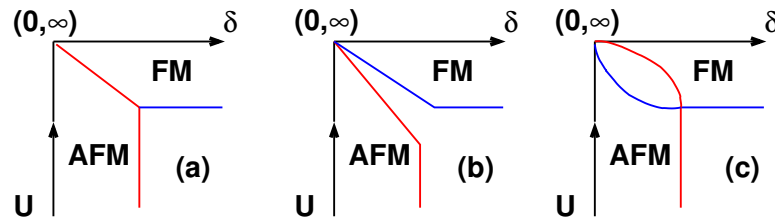


**Fig. 5.29:** Possible realizations of the phase diagram as  $(\delta, U) \rightarrow (0, \infty)$ : A direct transition between an antiferromagnet and a ferromagnet as in (a), a small paramagnetic phase between the two as in (b) or a mixed type of phase (e.g. ferrimagnet) as in (c).

There can either be a direct transition between the two phases (Fig. 5.29a), which quite likely would be of first order, a gap filled by a paramagnetic phase (Fig. 5.29b) or a new phase, e.g. a ferrimagnet interpolating between the two

extremes. The a priori exclusion or verification of any of these structures is, without a detailed knowledge of the analytic behaviour of the relevant quantities as function of  $(\delta, U)$  in the vicinity of  $(\delta, U) = (0, \infty)$ , not possible. Furthermore, an investigation of this problem within the DMFT of course requires that a stable solution can be obtained for the magnetic phase at intermediate values of  $U$ . At present, however, this does not seem to be possible.

## 6. SUMMARY AND OUTLOOK

In this thesis the magnetic properties of the one-band Hubbard model have been investigated within the dynamical mean-field theory, with a particular emphasis on the ground state of the model. To this end, an extension of the numerical renormalization group method to include the spin degree of freedom has been used to solve the effective impurity model.

The one-band Hubbard model is the simplest possible model to describe the interplay between delocalization or band formation in solids and the effects of local correlations. A thorough understanding of this model is essential both for the theoretical description of strongly correlated materials and in the view of possible extensions of the model to include additional degrees of freedom. Despite its simplicity, the phase diagram of the one-band Hubbard model reveals a surprising richness. In addition to Mott-Hubbard type metal-insulator transitions, a variety of magnetic phases can be found, and the model is frequently used to describe similar features in real materials, in particular transition metal oxides such as  $V_2O_3$ .

At the center of the investigations presented in this work is the dynamical mean-field theory. Within the framework of this theory, the lattice model is mapped onto an effective impurity problem, and quantities such as the single-particle Green's function can be calculated in a self-consistent fashion. For the solution of the impurity problem, the numerical renormalization group method has been used. While this method had successfully been used in the investigation of the paramagnetic metal-insulator transition within the DMFT before, it could not be applied to the symmetry-broken phases of the Hubbard model. Here, for the first time, it has been possible to study the magnetically ordered phases of this model, in particular in the ground state, using the NRG extended to treat spin-dependent problems.

In contrast to the standard NRG, a more refined approach has to be used for the calculation of dynamical quantities in the presence of a magnetic field. This has been discussed in detail in this work, and it should hopefully provide a better understanding of the underlying reasons and, in addition, allow for a straightforward implementation of this method by other people working in this field. It also lays the foundation for a possible extension of the NRG to include several orbitals, in order to investigate more realistic models within the DMFT along the

same lines. However, so far the increased computational effort does not allow for this, but in the future it should become possible to obtain results on a similar level of accuracy even in that case.

Within this work, fundamental results for the magnetic properties of the Hubbard model both at half filling and for finite doping have been obtained. At half filling, the ground state is an antiferromagnetic insulator for all values of the Coulomb interaction  $U$ . For small values of  $U$  clear signatures of a Slater insulator have been found, as expected from a weak-coupling theory. The strongly correlated system, on the other hand, can be well described in terms of a Mott-Heisenberg picture. This raises the question whether these two limits are linked continuously or via a phase transition at some critical value of the Coulomb interaction  $U$ , similar to what has been observed in the paramagnetic case. To address this open issue, in addition to the single-particle spectral function, the optical conductivity in the antiferromagnetic state has been calculated within the DMFT. While this quantity has frequently been used to study the paramagnetic phase, a comparable investigation of the antiferromagnetic state had not been carried out before. The behavior of both the optical gap and the spin gap, which has been extracted from the local transverse susceptibility, does not show any evidence for a transition, but rather a smooth crossover is found as a function of the Coulomb interaction.

The one-band Hubbard model has long been used to describe the paramagnetic metal-insulator transition in real materials such as  $V_2O_3$ . In order to arrive at a proper description of these materials, the antiferromagnetic phase at low temperatures also has to be taken into account. To that end, the Hubbard model with frustration of the magnetic order due to longer-range hopping processes has been studied within the DMFT. In contrast to previous results, where an extended antiferromagnetic metallic phase had been found for the same model, a first order transition from a paramagnetic metal to an antiferromagnetic insulator is observed at  $T = 0$ . In addition, even in the presence of strong frustration, the paramagnetic MIT is still hidden inside the antiferromagnetic phase. This raises the question whether the one-band Hubbard model can indeed be used to describe the phase diagram of  $V_2O_3$  or similar materials even qualitatively, or whether a more complicated model is needed.

To complete the ground state magnetic phase diagram within the DMFT, the model off half filling has been studied. To that end, the spectral properties in the ordered phases have been discussed. It has turned out that the antiferromagnetic state away from half filling is unstable towards phase separation for all dopings up to a critical value  $\delta_c$  at small and intermediate values of the Coulomb interaction. This is in good agreement with predictions from a weak-coupling theory in earlier works. At higher values of  $U$  an antiferromagnetic Néel order could not be stabilized, and other types of magnetic order, maybe an incommensurate phase,

---

seem to prevail in this parameter region. At very large  $U$  an extended ferromagnetic region has been found away from half filling, also in good agreement with previous DMFT studies at higher temperatures. As the doping  $\delta$  goes to zero, a fully polarized state is realized, however, from the numerical data, it can not be determined whether this takes place at a finite  $\delta$  or only in the limit  $\delta \rightarrow 0$ . In both the antiferromagnetic and the ferromagnetic case the resulting spectra for spin up and down are not simply shifted, but a strong redistribution of spectral weight can be found, as is common for correlated systems. Unfortunately, as the magnetic phase at intermediate values of the interaction  $U$  could not be stabilized, the interesting question about the precise nature of the transition between these two different ordered phases could not be addressed in this work.

With the extension of the NRG to treat spin-dependent problems, a reliable method is now available to study the magnetic properties of the Hubbard model at very low temperatures and in the ground state. The main extension of the calculations presented in this work would be the inclusion of additional degrees of freedom, in particular several orbitals. This would be extremely useful with respect to a more accurate description of real materials such as the transition metal oxides. If this could be done for at least three orbitals, the NRG would be the ideal method to complement the QMC, which is currently used to study these systems at higher temperatures. However, the numerical effort would be immense. Still, there are now first results for the case of two orbitals, and maybe at some point in the future the realistic description of strongly correlated materials within the DMFT, possibly in combination with the LDA, using the NRG as an impurity solver, will be possible.



# APPENDIX



## A. DETAILS OF THE NRG FORMALISM

### Iterative diagonalization

In order to diagonalize the Hamiltonian  $H_{N+1}$  in a given  $(Q, S_z)$  subspace, first the matrix of  $H_{N+1}$  in the representation (4.13) has to be built. Using the notation  $|ri\rangle_{N+1} := |Q, S_z, r, i\rangle_{N+1}$ , this matrix is obviously given by

$$\begin{aligned} {}_{N+1}\langle ri|H_{N+1}|r'j\rangle_{N+1} &= \Lambda^{1/2} {}_{N+1}\langle ri|H_N|r'j\rangle_{N+1} \\ &+ \Lambda^{N/2} \sum_{\sigma} \epsilon_{N+1\sigma} {}_{N+1}\langle ri|f_{N+1\sigma}^{\dagger} f_{N+1\sigma}|r'j\rangle_{N+1} \\ &+ \Lambda^{N/2} \sum_{\sigma} t_{N\sigma} {}_{N+1}\langle ri|f_{N\sigma}^{\dagger} f_{N+1\sigma} + f_{N+1\sigma}^{\dagger} f_{N\sigma}|r'j\rangle_{N+1}. \end{aligned}$$

The states  $|ri\rangle_{N+1}$  are eigenstates to  $H_N$ . Therefore, the only contributions due to  $H_N$  are those with  $r = r'$  and  $i = j$ :

$$\begin{aligned} {}_{N+1}\langle r1|H_N|r1\rangle_{N+1} &= E_N(Q + 1, S_z, r) \\ {}_{N+1}\langle r2|H_N|r2\rangle_{N+1} &= E_N(Q, S_z - 1/2, r) \\ {}_{N+1}\langle r3|H_N|r3\rangle_{N+1} &= E_N(Q, S_z + 1/2, r) \\ {}_{N+1}\langle r4|H_N|r4\rangle_{N+1} &= E_N(Q - 1, S_z, r). \end{aligned}$$

The  $E_N$  are the eigenenergies of  $H_N$ . Also, from the definition (4.13) it is clear that the only matrix elements of  $f_{N+1\sigma}^{\dagger} f_{N+1\sigma}$  that are non-trivial are

$$\begin{aligned} {}_{N+1}\langle r1|f_{N+1\sigma}^{\dagger} f_{N+1\sigma}|r1\rangle_{N+1} &= 0 \\ {}_{N+1}\langle r2|f_{N+1\uparrow}^{\dagger} f_{N+1\uparrow}|r2\rangle_{N+1} &= 1 \\ {}_{N+1}\langle r3|f_{N+1\downarrow}^{\dagger} f_{N+1\downarrow}|r3\rangle_{N+1} &= 1 \\ {}_{N+1}\langle r4|f_{N+1\sigma}^{\dagger} f_{N+1\sigma}|r4\rangle_{N+1} &= 1. \end{aligned}$$

Furthermore, as  ${}_{N+1}\langle ri|f_{N\sigma}^{\dagger} f_{N+1\sigma}|r'j\rangle_{N+1} = {}_{N+1}\langle r'j|f_{N+1\sigma}^{\dagger} f_{N\sigma}|ri\rangle_{N+1}$ , it is sufficient to calculate the matrix elements of  $f_{N\sigma}^{\dagger} f_{N+1\sigma}$ :

$$\begin{aligned} {}_{N+1}\langle r1|f_{N\uparrow}^{\dagger} f_{N+1\uparrow}|r'2\rangle_{N+1} &= {}_N\langle Q + 1, S_z, r|f_{N\uparrow}^{\dagger}|Q, S_z - 1/2, r'\rangle_N \\ {}_{N+1}\langle r1|f_{N\downarrow}^{\dagger} f_{N+1\downarrow}|r'3\rangle_{N+1} &= {}_N\langle Q + 1, S_z, r|f_{N\downarrow}^{\dagger}|Q, S_z + 1/2, r'\rangle_N \\ {}_{N+1}\langle r2|f_{N\downarrow}^{\dagger} f_{N+1\downarrow}|r'4\rangle_{N+1} &= {}_N\langle Q, S_z - 1/2, r|f_{N\downarrow}^{\dagger}|Q - 1, S_z, r'\rangle_N \\ {}_{N+1}\langle r3|f_{N\uparrow}^{\dagger} f_{N+1\uparrow}|r'4\rangle_{N+1} &= {}_N\langle Q, S_z + 1/2, r|f_{N\uparrow}^{\dagger}|Q - 1, S_z, r'\rangle_N. \end{aligned}$$

All the other matrix elements vanish.

Numerical diagonalization of the matrix  ${}_{N+1}\langle ri|H_{N+1}|r'j\rangle_{N+1}$  yields the eigenenergies  $E_{N+1}(Q, S_z, w)$  and the eigenstates

$$|Q, S_z, w\rangle_{N+1} = \sum_{ri} U_{QS_z}(w, ri) |Q, S_z, r, i\rangle_{N+1} \quad (\text{A.1})$$

of  $H_{N+1}$ . Here  $U_{QS_z}$  is the orthogonal matrix from the diagonalization of  $H_{N+1}$  in the subspace with quantum numbers  $(Q, S_z)$ , i.e. the columns of  $U_{QS_z}$  are just the eigenvectors to  $H_{N+1}$  in the representation (4.13).

Employing the matrices  $U_{QS_z}$  it is possible to construct the matrix of the operator  $f_{N+1\sigma}^\dagger$  in the new basis, which is needed for the next step in the iterative diagonalization,

$$\begin{aligned} & {}_{N+1}\langle Q, S_z, w|f_{N+1\sigma}^\dagger|Q', S'_z, w'\rangle_{N+1} \\ &= U_{QS_z} {}_{N+1}\langle Q, S_z, r, i|f_{N+1\sigma}^\dagger|Q', S'_z, r', j\rangle_{N+1} U_{Q'S'_z}^t. \end{aligned} \quad (\text{A.2})$$

There are only two cases that need to be considered. In the first case,  $Q' = Q - 1$  and  $S'_z = S_z - 1/2$ . The only non-vanishing matrix elements in the matrix

$${}_{N+1}\langle Q, S_z, r, i|f_{N+1\sigma}^\dagger|Q - 1, S_z - 1/2, r', j\rangle_{N+1} \quad (\text{A.3})$$

are given by

$$\begin{aligned} & {}_{N+1}\langle Q, S_z, r, 2|f_{N+1\uparrow}^\dagger|Q - 1, S_z - 1/2, r, 1\rangle_{N+1} = 1 \\ & {}_{N+1}\langle Q, S_z, r, 4|f_{N+1\uparrow}^\dagger|Q - 1, S_z - 1/2, r, 3\rangle_{N+1} = 1. \end{aligned}$$

The second case corresponds to  $Q' = Q - 1$  and  $S'_z = S_z + 1/2$ , and the matrix elements are

$$\begin{aligned} & {}_{N+1}\langle Q, S_z, r, 3|f_{N+1\downarrow}^\dagger|Q - 1, S_z + 1/2, r, 1\rangle_{N+1} = 1 \\ & {}_{N+1}\langle Q, S_z, r, 4|f_{N+1\downarrow}^\dagger|Q - 1, S_z + 1/2, r, 2\rangle_{N+1} = -1. \end{aligned}$$

Thus, the matrix elements of  $f_{N\sigma}^\dagger$  can be calculated in each step of the iterative procedure. For the first step, the impurity site alone, they can immediately be given:

$$\begin{aligned} & {}_{-1}\langle 0, -1/2|f_{-1\downarrow}^\dagger|-1, 0\rangle_{-1} = 1 \\ & {}_{-1}\langle 0, 1/2|f_{-1\uparrow}^\dagger|-1, 0\rangle_{-1} = 1 \\ & {}_{-1}\langle 1, 0|f_{-1\uparrow}^\dagger|0, -1/2\rangle_{-1} = 1 \\ & {}_{-1}\langle 1, 0|f_{-1\downarrow}^\dagger|0, 1/2\rangle_{-1} = -1. \end{aligned}$$

## Calculation of the spectral function

In order to calculate the impurity spectral function, it is necessary to know the matrix elements of  $f_{-1\sigma}^\dagger$  in each step. Again, using the unitary matrices  $U_{QS_z}$ , the matrix of  $f_{-1\sigma}^\dagger$  in the new basis can be calculated using the relation

$$\begin{aligned} & {}_{N+1}\langle Q, S_z, w | f_{-1\sigma}^\dagger | Q', S'_z, w' \rangle_{N+1} \\ &= U_{QS_z} {}_{N+1}\langle Q, S_z, r, i | f_{-1\sigma}^\dagger | Q', S'_z, r', j \rangle_{N+1} U_{Q'S'_z}^t. \end{aligned} \quad (\text{A.4})$$

It is clear that there are also only two cases that need to be considered.

If  $Q' = Q - 1$  and  $S'_z = S_z - 1/2$ , the matrix that has to be transformed is

$${}_{N+1}\langle Q, S_z, r, i | f_{-1\uparrow}^\dagger | Q - 1, S_z - 1/2, r', j \rangle_{N+1}. \quad (\text{A.5})$$

The only entries that are not vanishing are

$$\begin{aligned} i = j = 1 & : {}_N\langle Q + 1, S_z, r | f_{-1\uparrow}^\dagger | Q, S_z - 1/2, r' \rangle_N \\ i = j = 2 & : -{}_N\langle Q, S_z - 1/2, r | f_{-1\uparrow}^\dagger | Q - 1, S_z - 1, r' \rangle_N \\ i = j = 3 & : -{}_N\langle Q, S_z + 1/2, r | f_{-1\uparrow}^\dagger | Q - 1, S_z, r' \rangle_N \\ i = j = 4 & : {}_N\langle Q - 1, S_z, r | f_{-1\uparrow}^\dagger | Q - 2, S_z - 1/2, r' \rangle_N. \end{aligned}$$

Obviously this matrix is block diagonal and comprised of the matrix elements of  $f_{-1\uparrow}^\dagger$  from the previous step.

In the case  $Q' = Q - 1$  and  $S'_z = S_z + 1/2$ , the matrix

$${}_{N+1}\langle Q, S_z, r, i | f_{-1\downarrow}^\dagger | Q - 1, S_z + 1/2, r', j \rangle_{N+1} \quad (\text{A.6})$$

has to be considered. Its only entries are

$$\begin{aligned} i = j = 1 & : {}_N\langle Q + 1, S_z, r | f_{-1\downarrow}^\dagger | Q, S_z + 1/2, r' \rangle_N \\ i = j = 2 & : -{}_N\langle Q, S_z - 1/2, r | f_{-1\downarrow}^\dagger | Q - 1, S_z, r' \rangle_N \\ i = j = 3 & : -{}_N\langle Q, S_z + 1/2, r | f_{-1\downarrow}^\dagger | Q - 1, S_z + 1, r' \rangle_N \\ i = j = 4 & : {}_N\langle Q - 1, S_z, r | f_{-1\downarrow}^\dagger | Q - 2, S_z + 1/2, r' \rangle_N. \end{aligned}$$

The initial matrix elements  ${}_{-1}\langle Q, S_z | f_{-1\sigma}^\dagger | Q', S'_z \rangle_{-1}$  have already been given at the end of the previous section.

## Calculation of the self-energy

The calculation of the self-energy as described in Section 4.3 requires the knowledge of the matrix

$$\begin{aligned} & {}_{N+1}\langle Q, S_z, w | W_\sigma | Q', S'_z, w' \rangle_{N+1} \\ &= U_{QS_z} {}_{N+1}\langle Q, S_z, r, i | W_\sigma | Q', S'_z, r', j \rangle_{N+1} U_{Q'S'_z}^t. \end{aligned} \quad (\text{A.7})$$

Here, the notation  $W_\sigma := f_{-1\sigma} f_{-1\bar{\sigma}}^\dagger f_{-1\bar{\sigma}}$  has been introduced. This follows from the definition of the correlation function  $F_\sigma(z)$  by eq. (4.24).

Again, only two cases are relevant:

For  $Q' = Q + 1$  and  $S'_z = S_z - 1/2$ , the non-vanishing entries in the matrix

$${}_{N+1}\langle Q, S_z, r, i | W_\downarrow | Q + 1, S_z - 1/2, r', j \rangle_{N+1} \quad (\text{A.8})$$

are given by

$$\begin{aligned} i = j = 1 & : {}_N\langle Q + 1, S_z, r | W_\downarrow | Q + 2, S_z - 1/2, r' \rangle_N \\ i = j = 2 & : -{}_N\langle Q, S_z - 1/2, r | W_\downarrow | Q + 1, S_z - 1, r' \rangle_N \\ i = j = 3 & : -{}_N\langle Q, S_z + 1/2, r | W_\downarrow | Q + 1, S_z, r' \rangle_N \\ i = j = 4 & : {}_N\langle Q - 1, S_z, r | W_\downarrow | Q, S_z - 1/2, r' \rangle_N. \end{aligned}$$

In the case of  $Q' = Q + 1$  and  $S'_z = S_z + 1/2$ , the matrix elements of

$${}_{N+1}\langle Q, S_z, r, i | W_\uparrow | Q + 1, S_z + 1/2, r', j \rangle_{N+1} \quad (\text{A.9})$$

are

$$\begin{aligned} i = j = 1 & : {}_N\langle Q + 1, S_z, r | W_\uparrow | Q + 2, S_z + 1/2, r' \rangle_N \\ i = j = 2 & : -{}_N\langle Q, S_z - 1/2, r | W_\uparrow | Q + 1, S_z, r' \rangle_N \\ i = j = 3 & : -{}_N\langle Q, S_z + 1/2, r | W_\uparrow | Q + 1, S_z + 1, r' \rangle_N \\ i = j = 4 & : {}_N\langle Q - 1, S_z, r | W_\uparrow | Q, S_z + 1/2, r' \rangle_N. \end{aligned}$$

The initial matrix elements  ${}_{-1}\langle Q, S_z | W_\sigma | Q', S'_z \rangle_{-1}$  are easily evaluated:

$$\begin{aligned} {}_{-1}\langle 0, -1/2 | W_\uparrow | 1, 0 \rangle_{-1} & = 1 \\ {}_{-1}\langle 0, 1/2 | W_\downarrow | 1, 0 \rangle_{-1} & = -1. \end{aligned}$$

## B. EVALUATION OF THE INTEGRALS IN SEC. 3.3

In this appendix details of the evaluation of the energy integrals in equation (3.18) for the hypercubic lattice in the limit  $d \rightarrow \infty$  are presented.

In that case, the density of states becomes a Gaussian, and the integrals

$$\int_{-\infty}^{\infty} d\epsilon e^{-\epsilon^2} A_{\sigma}(\epsilon, \omega') A_{\bar{\sigma}}(\epsilon, \omega' + \omega)$$

and

$$\int_{-\infty}^{\infty} d\epsilon e^{-\epsilon^2} B_{\sigma}(\epsilon, \omega') B_{\sigma}(\epsilon, \omega' + \omega)$$

have to be calculated.

It is now convenient to split up the spectral functions into two parts,

$$A_{\sigma}(\epsilon, \omega) = A_{\sigma}^{-}(\epsilon, \omega) + A_{\sigma}^{+}(\epsilon, \omega)$$

with

$$A_{\sigma}^{\pm}(\epsilon, \omega) = -\frac{1}{2\pi} \Im m \frac{\zeta_{\bar{\sigma}}}{\sqrt{\zeta_{\sigma} \zeta_{\bar{\sigma}}}} \left( \frac{1}{\sqrt{\zeta_{\sigma} \zeta_{\bar{\sigma}} \pm \epsilon}} \right)$$

and  $\zeta_{\sigma}$  as defined in eq. (3.15). In the same way one can write

$$B_{\sigma}(\epsilon, \omega) = B_{\sigma}^{-}(\epsilon, \omega) - B_{\sigma}^{+}(\epsilon, \omega)$$

where now

$$B_{\sigma}^{\pm}(\epsilon, \omega) = -\frac{1}{2\pi} \Im m \frac{1}{\sqrt{\zeta_{\sigma} \zeta_{\bar{\sigma}} \pm \epsilon}} .$$

Using this notation and collecting equivalent terms, it can easily be verified that the following four integrals need to be calculated:

$$I_1 = 2 \int_{-\infty}^{\infty} d\epsilon e^{-\epsilon^2} B_{\sigma}^{-}(\epsilon, \omega') B_{\sigma}^{-}(\epsilon, \omega' + \omega)$$

$$I_2 = -2 \int_{-\infty}^{\infty} d\epsilon e^{-\epsilon^2} B_{\sigma}^{-}(\epsilon, \omega') B_{\sigma}^{+}(\epsilon, \omega' + \omega)$$

$$I_3 = 2 \int_{-\infty}^{\infty} d\epsilon e^{-\epsilon^2} A_{\sigma}^{-}(\epsilon, \omega') A_{\bar{\sigma}}^{-}(\epsilon, \omega' + \omega)$$

$$I_4 = 2 \int_{-\infty}^{\infty} d\epsilon e^{-\epsilon^2} A_{\sigma}^{-}(\epsilon, \omega') A_{\sigma}^{+}(\epsilon, \omega' + \omega) .$$

The further evaluation will be demonstrated for the first term.

Using the notation

$$\alpha = \sqrt{\zeta_{\sigma} \zeta_{\bar{\sigma}}} \Big|_{\omega' + i\delta} \quad \text{and} \quad \beta = \sqrt{\zeta_{\sigma} \zeta_{\bar{\sigma}}} \Big|_{\omega' + \omega + i\delta}$$

one can write

$$B_{\sigma}^{-}(\epsilon, \omega') B_{\sigma}^{-}(\epsilon, \omega' + \omega) = -\frac{1}{4\pi^2} \left[ \left( \frac{1}{\bar{\alpha} - \epsilon} - \frac{1}{\alpha - \epsilon} \right) \left( \frac{1}{\bar{\beta} - \epsilon} - \frac{1}{\beta - \epsilon} \right) \right] ,$$

where the bar above a term denotes complex conjugation. The terms inside the brackets can be expanded further to yield

$$\left[ -\frac{1}{\bar{\alpha} - \bar{\beta}} \left( \frac{1}{\bar{\alpha} - \epsilon} - \frac{1}{\bar{\beta} - \epsilon} \right) + \frac{1}{\bar{\alpha} - \beta} \left( \frac{1}{\bar{\alpha} - \epsilon} - \frac{1}{\beta - \epsilon} \right) + \frac{1}{\alpha - \bar{\beta}} \left( \frac{1}{\alpha - \epsilon} - \frac{1}{\bar{\beta} - \epsilon} \right) - \frac{1}{\alpha - \beta} \left( \frac{1}{\alpha - \epsilon} - \frac{1}{\beta - \epsilon} \right) \right] .$$

Using the Faddeeva function

$$w(z) = \frac{i}{\pi} \int_{-\infty}^{\infty} dt \frac{e^{-t^2}}{z - t} = e^{-z^2} \operatorname{erfc}(-iz)$$

for complex arguments  $z$  with  $\Im m z > 0$ , the result is

$$I_1 = \frac{1}{2\pi i} \left[ \frac{w(\alpha) - w(\beta)}{\alpha - \beta} - \frac{\overline{w(\alpha)} - \overline{w(\beta)}}{\bar{\alpha} - \bar{\beta}} - \frac{w(\alpha) + \overline{w(\beta)}}{\alpha - \bar{\beta}} + \frac{w(\alpha) + \overline{w(\beta)}}{\bar{\alpha} - \beta} \right] .$$

Here the relation  $w(-\bar{z}) = \overline{w(z)}$  has been used. The remaining three contributions can be obtained in a similar fashion.

Finally, combining complex conjugate expressions, the results are

$$I_1 = \frac{1}{\pi} \Im m \left( \frac{w(\alpha) - w(\beta)}{\alpha - \beta} - \frac{w(\alpha) + \overline{w(\beta)}}{\alpha - \bar{\beta}} \right) \quad (\text{B.1})$$

$$I_2 = -\frac{1}{\pi} \Im m \left( \frac{w(\alpha) - \overline{w(\beta)}}{\alpha + \bar{\beta}} - \frac{w(\alpha) + w(\beta)}{\alpha + \beta} \right) \quad (\text{B.2})$$

$$I_3 = \frac{1}{\pi} \Im m \left( \gamma \delta \frac{w(\alpha) - w(\beta)}{\alpha - \beta} - \gamma \bar{\delta} \frac{w(\alpha) + \overline{w(\beta)}}{\alpha - \bar{\beta}} \right) \quad (\text{B.3})$$

$$I_4 = \frac{1}{\pi} \Im m \left( \gamma \bar{\delta} \frac{w(\alpha) - \overline{w(\beta)}}{\alpha + \bar{\beta}} - \gamma \delta \frac{w(\alpha) + w(\beta)}{\alpha + \beta} \right) \quad (\text{B.4})$$

with the notation

$$\gamma = \frac{\zeta_{\bar{\sigma}}}{\sqrt{\zeta_{\sigma} \zeta_{\bar{\sigma}}}} \Big|_{\omega' + i\delta} \quad \text{and} \quad \delta = \frac{\zeta_{\sigma}}{\sqrt{\zeta_{\sigma} \zeta_{\bar{\sigma}}}} \Big|_{\omega' + \omega + i\delta} .$$

A further analytical evaluation of the remaining integration over  $\omega'$  in eq. (3.18) using eqs. (B.1) – (B.4) is possible only for  $\zeta_{\sigma} \rightarrow \omega - \sigma\Delta_0 + i\delta$ . In this case, the square-roots appearing in the functions  $\alpha$  and  $\beta$  lead to a typical threshold behavior of the form [Mah90]

$$\omega \cdot \sigma(\omega) \propto \frac{\Theta(\omega - 2\Delta_0)}{\sqrt{\omega - 2\Delta_0}} .$$

The appearance of this threshold singularity also shows that a further numerical evaluation of the remaining integral over  $\omega'$  in equation (3.18) will become problematic in regions where the imaginary part of the one-particle self-energy becomes small, because the integrand will develop a strongly singular behavior. In particular, this makes a precise numerical evaluation of the optical conductivity near the threshold impossible.



## BIBLIOGRAPHY

- [And61] P. W. Anderson, Phys. Rev. **124**, 41 (1961).
- [And63] P. W. Anderson, Solid State Phys. **14**, 99 (1963).
- [And83] N. Andrei, K. Furuya, and J. M. Lowenstein, Rev. Mod. Phys. **55**, 331 (1983).
- [And87] P. W. Anderson, Science **235**, 1196 (1987).
- [Bec00] F. Becca, M. Capone, and S. Sorella, Phys. Rev. B **62**, 12700 (2000).
- [Blu02] N. Blümer, Dissertation, Augsburg (2002).
- [Bra90] U. Brandt and C. Mielsch, Z. Phys. B – Condensed Matter **79**, 295 (1990).
- [Bra91] U. Brandt and C. Mielsch, Z. Phys. B – Condensed Matter **82**, 37 (1991).
- [Bri70] W. F. Brinkman and T. M. Rice, Phys. Rev. B **2**, 4302 (1970).
- [Bul94] R. Bulla, Dissertation, Regensburg (1994).
- [Bul97] R. Bulla, Th. Pruschke, and A. C. Hewson, J. Phys.: Condens. Matter **9**, 10463 (1997).
- [Bul98] R. Bulla, A. C. Hewson, and Th. Pruschke, J. Phys.: Condens. Matter **10**, 8365 (1998).
- [Bul99] R. Bulla, Phys. Rev. Lett. **83**, 136 (1999).
- [Bul00] R. Bulla, Habilitationsschrift, Augsburg (2000).
- [Bul01] R. Bulla, T. A. Costi, and D. Vollhardt Phys. Rev. B **64**, 045103 (2001).
- [Cas79] C. Castellani, C. Di Castro, D. Feinberg, and J. Ranninger, Phys. Rev. Lett. **43**, 1957 (1979).
- [Cas95] C. Castellani, C. Di Castro, and M. Grilli, Phys. Rev. Lett. **75**, 4650 (1995).

- [Chi99] R. Chitra and G. Kotliar, Phys. Rev. Lett. **83**, 2386 (1999).
- [Cos94] T. A. Costi, A. C. Hewson, and V. Zlatic, J. Phys.: Condens. Matter **6**, 2519 (1994).
- [Cos00] T. A. Costi, Phys. Rev. Lett. **85**, 1504 (2000).
- [Cyr77] M. Cyrot, Physica B **91**, 141 (1977).
- [Dag94] E. Dagotto, Rev. Mod. Phys. **66**, 763 (1994).
- [Don91] P. G. J. van Dongen, Phys. Rev. Lett. **67**, 757 (1991).
- [Don94] P. G. J. van Dongen, Phys. Rev. B **50**, 14016 (1994).
- [Don96] P. G. J. van Dongen, Phys. Rev. B **54**, 1584 (1996).
- [Eme90] V. J. Emery, S. A. Kivelson, and H. Q. Lin, Phys. Rev. Lett. **64**, 475 (1990).
- [Eme93] V. J. Emery and S. A. Kivelson, Physica C **209**, 597 (1993).
- [Faz90] P. Fazekas and E. Müller-Hartmann, Z. Phys. B **78**, 69 (1990).
- [Fre95] J. K. Freericks and M. Jarrell, Phys. Rev. Lett. **74**, 186 (1995).
- [Fre01] J. K. Freericks, T. P. Deveraux, and R. Bulla, Phys. Rev. B **64**, 233114 (2001).
- [Fre03] J. K. Freericks, T. P. Deveraux, R. Bulla, and Th. Pruschke, Phys. Rev. B **67**, 155102 (2003).
- [Fro86] H. O. Frota and L. N. Oliveira, Phys. Rev. B **33**, 7871 (1986).
- [Ful95] P. Fulde, *Electron correlations in molecules and solids*, Springer, Berlin (1995).
- [Gel54] M. Gell-Mann and F. E. Low, Phys. Rev. **95**, 1300 (1954).
- [Geo92a] A. Georges and G. Kotliar, Phys. Rev. B **45**, 6479 (1992).
- [Geo92b] A. Georges, G. Kotliar, and Q. Si, Int. Journ. Mod. Phys. B **6**, 705 (1992).
- [Geo96] A. Georges, G. Kotliar, W. Krauth, and M. J. Rozenberg, Rev. Mod. Phys. **68**, 13 (1996).
- [Hel97] C. S. Hellberg and E. Manousakis, Phys. Rev. Lett. **78**, 4609 (1997).

- [Hew93] A. C. Hewson, *The Kondo Problem to Heavy Fermions*, Cambridge University Press, Cambridge (1993).
- [Hof98] W. Hofstetter and D. Vollhardt, *Ann. Physik* **7**, 48 (1998).
- [Hof00] W. Hofstetter, *Phys. Rev. Lett.* **85**, 1508 (2000).
- [Hub63] J. Hubbard, *Proc. R. Soc. A* **276**, 238 (1963); M. C. Gutzwiller, *Phys. Rev. Lett.* **10**, 159 (1963); J. Kanamori, *Prog. Theor. Phys.* **30**, 257 (1963).
- [Ima98] M. Imada, A. Fujimori, and Y. Tokura, *Rev. Mod. Phys.* **70**, 1039 (1998).
- [Itz89] C. Itzykson and J. M. Drouffe, *Statistical Field Theory*, Vol. I & II, Cambridge University Press, Cambridge (1989).
- [Jan91] V. Janis, *Z. Phys. B – Condensed Matter* **83**, 227 (1991).
- [Jar92] M. Jarrell, *Phys. Rev. Lett.* **69**, 168 (1992).
- [Jar93] M. Jarrell and Th. Pruschke, *Z. Phys. B – Condensed Matter* **90**, 187 (1993).
- [Kel04] G. Keller, K. Held, V. Eyert, D. Vollhardt, and V. Anisimov, *cond-mat/0402133*.
- [Khu90] A. Khurana, *Phys. Rev. Lett.* **64**, 1990 (1990).
- [Kon64] J. Kondo, *Prog. Theor. Phys.* **32**, 37 (1964).
- [Kri80] H. R. Krishna-murthy, J. W. Wilkins, and K. G. Wilson, *Phys. Rev. B* **21**, 1003 and 1044 (1980).
- [Lal94] L. Laloux, A. Georges, and W. Krauth, *Phys. Rev. B* **50**, 3092 (1994).
- [Lee92] P. A. Lee and N. Nagaosa, *Phys. Rev. B* **46**, 5621 (1992).
- [Lie95] E. H. Lieb, *The Hubbard model – Some Rigorous Results and Open Problems*, Proceedings of the XIth International Congress of Mathematical Physics, Paris 1994, ed. D. Iagolnitzer, International Press (1995)
- [Mah90] G. Mahan, *Many-Particle Physics*, Plenum Press, New York (1990).
- [Mai97] Th. Maier, *Diplomarbeit*, Regensburg (1997), unpublished.
- [McW70] D. B. McWhan and J. P. Remeika, *Phys. Rev. B* **2**, 3734 (1970); D. B. McWhan *et al.*, *Phys. Rev. B* **7**, 1920 (1973).

- [Met89] W. Metzner and D. Vollhardt, Phys. Rev. Lett. **62**, 324 (1989).
- [Mon92] A. Montorsi ed., *The Hubbard Modell – A Reprint Volume*, World Scientific Publ., Singapore (1992).
- [Mot61] N. F. Mott, Philos. Mag. **6**, 287 (1961).
- [Mot68] N. F. Mott, Rev. Mod. Phys. **40**, 677 (1968).
- [Mou01] S. Moukouri and M. Jarrell, Phys. Rev. Lett. **87**, 167010 (2001).
- [Mue89] E. Müller-Hartmann, Z. Phys. B - Condensed Matter **74**, 507 (1989).
- [Nag66] Y. Nagaoka, Phys. Rev. **147**, 392 (1966).
- [Obe97a] Th. Obermeier, Dissertation, Regensburg (1997).
- [Obe97b] Th. Obermeier, Th. Pruschke, and J. Keller, Phys. Rev. B **56**, R8479 (1997).
- [Pru89] Th. Pruschke, Dissertation, Darmstadt (1989).
- [Pru93] Th. Pruschke, D. L. Cox, and M. Jarrell, Phys. Rev. B **47**, 3553 (1993).
- [Pru95] Th. Pruschke, M. Jarrell, and J. K. Freericks, Adv. Phys. **42**, 187 (1995).
- [Pru03] Th. Pruschke and R. Zitzler, J. Phys.: Condens. Matter **15**, 7867 (2003).
- [Pry98] L. P. Pryadko, S. Kivelson, and D. W. Hone, Phys. Rev. Lett. **80**, 5651 (1998).
- [Roz95] M. J. Rozenberg *et al.*, Phys. Rev. Lett. **75**, 105 (1995).
- [Roz99] M. J. Rozenberg, R. Chitra, and G. Kotliar, Phys. Rev. Lett. **83**, 3498 (1999).
- [Sak89] O. Sakai, Y. Shimizu, and T. Kasuya, J. Phys. Soc. Japan **58**, 3666 (1989).
- [Sch90] H. J. Schulz, Phys. Rev. Lett. **64**, 1445 (1990).
- [Sla51] J. C. Slater, Phys. Rev. **82**, 538 (1951).
- [Su96] G. Su, Phys. Rev. B **54**, R8281 (1996).
- [Tan99] A. Tandon, Z. Wang, and G. Kotliar, Phys. Rev. Lett. **83**, 2046 (1999).
- [Tas98a] H. Tasaki, Prog. Theor. Phys. **99**, 489 (1998).
- [Tas98b] H. Tasaki, J. Phys.: Condens. Matter **10**, 4353 (1998).

- 
- [Tho94] G. A. Thomas, D. H. Rapkine, S. A. Carter, A. J. Millis, T. F. Rosenbaum, P. Metcalf, and J. M. Honig, *Phys. Rev. Lett.* **73**, 1529 (1994).
- [Ton01] N. H. Tong, S. Q. Shen, and F. C. Pu, *Phys. Rev. B* **64**, 235109 (2001).
- [Tsv83] A. M. Tsvelick and P. B. Wiegmann, *Advances in Physics* **32**, 453 (1983).
- [Uhr96] G. S. Uhrig, *Phys. Rev. Lett.* **77**, 3629 (1996).
- [Ulm98] M. Ulmke, *Eur. Phys. J. B* **1**, 301 (1998).
- [Vol97] D. Vollhardt, N. Blümer, K. Held, M. Kollar, J. Schlipf, and M. Ulmke, *Z. Phys. B* **103**, 283 (1997).
- [Wil74] K. G. Wilson and J. Kogut, *Phys. Rep. C* **12**, 75 (1974).
- [Wil75] K. G. Wilson, *Rev. Mod. Phys.* **47**, 773 (1975).
- [Zit00] R. Zitzler, Diplomarbeit, Regensburg (2000), unpublished.
- [Zit02] R. Zitzler, Th. Pruschke, and R. Bulla, *Eur. Phys. J. B* **27**, 473 (2002).
- [Zit03] R. Zitzler, N. Tong, Th. Pruschke, and R. Bulla, cond-mat/0308202.



## ACKNOWLEDGEMENTS

First of all, I would like to thank my advisor Prof. Dr. Thomas Pruschke for his continued support and invaluable assistance during all this time. I am particularly grateful for his dedication and positive thinking whenever the results of the calculations turned out to be something unexpected. He always believed in me, and the discussions with him helped me greatly in getting a better understanding of physics.

I also want to thank Prof. Dr. Joachim Keller for his support, especially during the time when Thomas Pruschke had already left for Augsburg. He was the one who brought the field of electronic correlations to my attention when I was a student, and later on I started my research in his group in Regensburg. I would like to thank all the past and present members of this group, in particular Bernhard Rieder, Dmitri Ryndyk, Werner Heindl, Thomas Maier, Markus Zöfl and Christian Preis. I have many fond memories of my time in Regensburg.

I am very grateful to Prof. Dr. Dieter Vollhardt for accepting me into his group, and his generous support allowed me to finish my thesis in Augsburg even after Thomas Pruschke had become a professor at Göttingen. It has been a privilege to do my research under the excellent conditions found at the Center for Electronic Correlations and Magnetism. This is also due to all the talented physicists that have been or still are members of this group. They are far too many to mention, and I would like to thank all of them for providing many helpful discussions and creating a very friendly atmosphere. In particular I thank Prof. Dr. Arno P. Kampf, Michael Sekania, Georg Keller, Matthias Vojta and Ning-Hua Tong.

I would like to especially mention Ralf Bulla. Writing this thesis I have come to realize once more how much of my work is owed to the things he has done before me. My interest in the NRG was awakened by reading the thesis that he wrote in Regensburg ten years ago, and I would be more than happy if the work presented here someday succeeds in doing the same thing for someone else.

I also want to thank my friend Thomas Pfadenhauer for his meticulous proof-reading of this thesis. I think I can say with confidence that I could not have found someone better suited to this task than him.

Finally, I thank my family for their support over the years. Right now, they are the most important thing in my life.